# Laser-Driven Ion Beam Characteristics and Dose Measurements for Medical Applications

Inaugural-Dissertation

zur Erlangung des Doktorgrades
der Mathematisch-Naturwissenschaftlichen Fakultät
der Heinrich-Heine-Universität Düsseldorf

vorgelegt von

**Sven Spickermann**
aus Herdecke

Düsseldorf, Juni 2019

aus dem Institut für Laser- und Plasmaphysik
der Heinrich-Heine-Universität Düsseldorf

Gedruckt mit der Genehmigung der
Mathematisch-Naturwissenschaftlichen Fakultät der
Heinrich-Heine-Universität Düsseldorf

Berichterstatter:

1. Prof. Dr. Oswald Willi

2. Prof. Dr. Alexander Pukhov

Tag der mündlichen Prüfung: 08.11.2019

## Abstract

Ultraintense laser-plasma interactions offer a wide variety of interesting topics for research, among them particle acceleration from overdense targets. The optimization of the accelerated particles for a given application is a complex task, as laser and plasma influence one another during the interaction and numerous processes compete.

One such task is the medical application of ions accelerated from laser-plasma interaction. A dose delivery and measurement system for such an application is presented in this thesis, including a novel method to determine the average dose. It is shown that while the shot to shot fluctuation of this system is quite high ($\approx 70\,\%$), the average dose could be determined with an accuracy of $13\,\%$.

In addition, laser-plasma interaction experiments with two beams were performed, with a time-delay between both beams of up to several nanoseconds. The ion numbers as well as their cutoff energies were measured and their dependence on laser conditions and time-delay were investigated with the help of a dedicated plasma mirror, built as part of this work.

It is shown that in the two beam case the number of particles is reduced compared to the single beam case. Simulations have been performed, which helped explain this surprising phenomenon due to the effect of the combined laser-prepulses of both beams. It is also found that the optimal cutoff energy of ions depends on the temporal delay between two beams and does not occur in the synchronized case. It is found that this dependence can be explained by an increased efficiency of resonance absorption as the scale lengths increase along with a longer plasma expansion. While Target Normal Sheath Acceleration appears to play an important role in the observed spectra under $0\,^\circ$, there are indications of a deviation from a mere TNSA interaction in the two beam case.

One very clear indication is the appearance of quasi-monoenergetic peaks (FWHM of about $10\,\%$) in the ion spectra under $10\,^\circ$ to the target rear side normal. Another indication for this is the dependence of the increase in cutoff energy in the two beam case relative to the single beam case on the ion charge state, which also points to a deviation from a pure TNSA interaction.

## Zusammenfassung

Ultraintensive Laser-Plasma-Interaktionen bieten eine große Breite an interessanten Forschungsthemen, einschließlich Teilchenbeschleunigung aus überkritischen Targets. Die Optimierung der beschleunigten Teilchen für eine gegebene Anwendung ist eine komplexe Aufgabe, da Laser und Plasma einander während der Interaktion beeinflussen und diverse Prozesse miteinander konkurrieren.

Eine solche Aufgabe ist die medizinische Anwendung von durch Laser-Plasma-Interaktionen beschleunigter Ionen. In dieser Arbeit wird ein Dosis-Depositions- und Messsystem für eine solche Anwendung eingeführt, einschließlich einer neuartigen Methode zur Bestimmung der Dosis. Es wird gezeigt, dass trotz recht hoher Schuss-zu-Schuss-Fluktuationen ($\approx 70\,\%$), die durchschnittliche Dosis mit einer Genauigkeit von $13\,\%$ bestimmt werden konnte.

Außerdem wurden Laser-Plasma-Experimente mit zwei zueinander zeitlich verzögerten Strahlen durchgeführt, wobei die Zeitverzögerung bis zu einigen Nanosekunden betrug. Die Ionenanzahl als auch ihre Cutoff-Energien wurden gemessen und auf ihre Abhängigkeit von den Laser-Bedingungen und der zeitlichen Verzögerung hin untersucht, mithilfe eines im Rahmen dieser Arbeit gebauten Plasmaspiegels.

Es konnte gezeigt werden, dass im Zweistrahlfall die Teilchenzahl gegenüber dem Einstrahlfall reduziert ist. Es wurden Simulationen durchgeführt, die dabei halfen, dieses überraschende Phänomen mit den kombinierten Laser-Vorpulsen beider Strahlen zu erklären. Weiterhin wurde festgestellt, dass die optimale Cutoff-Energie von der zeitlichen Verzögerung beider Strahlen abhängt und nicht im zeitlich synchronisierten Fall auftritt, sowie mit den Laserbedingungen variiert. Es wird gezeigt, dass diese Abhängigkeit sich mit einer erhöhten Effizienz von Resonanzabsorption erklären lässt, da die Skalenlänge mit zunehmender Expansion zunehmen. Target Normal Sheath Acceleration scheint eine wichtige Rolle bei den in Richtung der Targetnormalen beobachteten Spektren zu spielen, jedoch gibt es Anzeichen einer Abweichung von einer reinen TNSA-Interaktion im Zweistrahlfall.

Ein sehr deutliches derartiges Anzeichen ist das Auftauchen quasi-monoenergetischer Peaks (mit einer Halbwertsbreite von etwa $10\,\%$) in den Ionenspektren, die unter $10^\circ$ zur rückwärtigen Targetnormalen gemessen wurden. Ein weiteres Anzeichen liegt in der Abhängigkeit der Zunahme der Cutoff-Energie im Zweistrahlfall relativ zum Einstrahlfall vom Ladungszustand der Ionen, was ebenfalls auf eine Abweichung von einer reinen TNSA-Interaktion hindeutet.

# Contents

# Chapter 1

# Introduction

In recent years protons accelerated by laser-induced processes and their application in the field of radiation therapy have come into increased focus [1, 2, 3, 4, 5, 6]. One expectation is that it might be cheaper than continuous irradiation by protons, in addition to the natural advantages protons have over X-rays due to the Bragg peak phenomenon which allows for a more localized energy deposition. This thesis presents, as a practical contribution to this debate, a cell irradiation system comprising a tape driver, a magnetic energy selection and a cell port, into which cells can be put for irradiation. In addition, a dosimetric method for assessing the dose deposited on cells is presented. We used the system to irradiate A549 lung cancer cells and were able to demonstrate DNA damage comparable to that caused by protons from standard accelerators. We also showed a significant difference in terms of nitroxidative stress between the two modes of irradiation, inferred from differences in nitrotyrosine creation. The biological results and analysis of these experiments were described in detail by Raschke et al [7]. The first part of this thesis focuses on the physical requirements for this unique irradiation modality as well as the dosimetry for the dose deposition by laser driven protons for the case of our setup, followed by a discussion of the biological results achieved with its help.

The second part of this work describes an experimental setup for ion acceleration with two beams and the dependence of ion numbers as well as cutoff energies on the delay between both beams as well as different acceleration processes which may be responsible for these results. In this area we also found interesting results concerning the carbon ion energies, particle numbers as well as spectral peaks under $10\,^{\circ}$. In the concluding part, there is a discussion on what can be learned from the results of this thesis and

what future perspectives offer themselves for irradiation of cells by laser-driven ion acceleration in the context of two beam experimental setups.

## Thesis Structure

The structure of this thesis in terms of chapters is as follows. Following this introduction, **Chapter 2** discusses the theoretical background in laser-plasma physics. It starts by describing different ionization and absorption mechanisms, which transfer energy from the laser to the plasma. Afterwards different mechanisms for ion acceleration are discussed, including Target Normal Sheath Acceleration, Collisionless Shock Acceleration and Radiation Pressure Acceleration.

**Chapter 3** introduces the ARCTURUS laser system on which the experiments described in this work were performed. The principle concept of CPA [8] is discussed as are the components of the laser system and the plasma mirror (3.4), which was built for this thesis.

**Chapter 4** contains a discussion of the diagnostics which were used during the experimental campaigns discussed in this work. It begins with a discussion about the challenges and different approaches and diagnostics concerning dosimetry. It then explains the dose delivery and measurement system employed in this work in detail, with a description of the design decisions (4.3), the physical components of the system (4.4), a discussion of the energy transfer from protons to cells and subsequent cell damage (4.5) and finally a description of the method used to arrive at a dose (4.6) .

**Chapter 5** discusses the experimental results achieved with the help of the concepts and methods described in the previous chapter. It discusses dosimetry with the help of PADC plastics as well as with Imaging Plates. Section 5.5.3 describes the main results of the biological experiments performed with the help of the dosimetric methods described earlier, which were also published in [7].

**Chapter 6** contains all the specific setups and experimental results for ion acceleration in the two beam setup and their interpretation. Section (6.1) gives an introduction and a background in earlier experiments with two beams. (6.2) discusses the spectral shape of ion spectra under $0^\circ$ to the target normal. (6.3) discusses the maximum detected ion energies and their dependence on the delay between the two beams, whereas (6.5) investigates the particle numbers and how the different settings affect them. There is also a discussion of results of ion spectra under $10^\circ$ to the target rear side normal

(6.6), where unusual spectral features were found, as well as transparency measurements with thin foils on the order of hundreds of nanometers (6.7). In the final subsection, (6.8), the results of the two beam ion experiments and the main conclusions from their interpretation are summarized.

**Chapter 7** summarizes the outcome of this work in its entirety and an outlook is presented.

## Role of the Author

The author developed the dosimetric measurement method described in this thesis. He built the tape driver used in it [9], planned the experimental geometry and relied on infrastructure put in place by Philip Weiß. He modified and enhanced a particle tracer originally written by Philip Weiß [10]. The author built a plasma mirror and participated in experiments for the plasma mirror's characterization, which he also evaluated. The author participated in cell biological experiments at ILPP and at the PTB in Braunschweig and in their data analysis and evaluation [7]. He evaluated the dosimetric media from the experiments at ILPP including etching CR39 plastic as well as investigating them under a microscope and counting tracks. The author ran simulations with the software SRIM in order to determine the energy deposition per proton for protons of different energies and for different setups at ILPP and PTB. For dose evaluation of imaging plates, which the author performed, he significantly modified and expanded a program originally written by Alexander Mick. The programs written by the author, mentioned in the above paragraph, are attached as appendices in sections 8.1 and 8.2.

The author participated in the setup and the performance of two beam experiments described in this thesis as well as in their evaluation. The participation included target preparation and data recording, while the evaluative role included the etching of CR39 plastics for the calbration as well as an analysis of carbon ion Thomson parabola traces under $0\,^\circ$ and $10\,^\circ$ to the target rear side normal. Some steps of this process for some conditions were also performed by Mara Wiltshire and used for later steps by this author. Similarly, for the calibration which the author used, he heavily relied on work by Mara Wiltshire and Marco Swantusch. The author also performed additional data analysis of carbon ion data resulting from experiments described in Jürgen Böker's thesis [11]. The author also ran simulations with MULTI-fs.

# Chapter 2

# Absorption Mechanisms and Laser-Driven Particle Acceleration

## 2.1 Introduction

In this chapter, modes of particle acceleration under the influence of a laser are described. It begins by expounding the mechanisms of ionization and absorption by laser light, such as Brunel heating, inverse bremsstrahlung, $j \times B$ heating, and the effects of the ponderomotive force. Later we turn our attention to the methods of ion acceleration, including TNSA, RPA and collisionless shock acceleration. In the final section we discuss the implications for the future of medical applications using ions accelerated by laser-driven processes and assess their respective usefulness.

## 2.2 Laser Generated Plasmas and Ionizing Processes

### 2.2.1 Types of Plasmas

There are many different kinds of plasmas and almost as many applications and areas of interest for and within plasma physics [12]. In this chapter we will focus mainly on laser generated plasmas and within this area on overdense plasmas created by femtosecond ultra-intense laser systems specifically, as this is the kind of plasma that is relevant in

the context of the experiments described in this thesis. A plasma is a gas containing charged particles and it is quasi-neutral, which means outside of the range of the *Debye length* there are no deviations from neutrality. The Debye length is defined by:

$$\lambda_d = \sqrt{\frac{\epsilon_0 k_B T_e}{n_e e^2}} \tag{2.1}$$

where $k_b$ is Boltzmann's constant, $T_e$ is the temperature of the electrons, $n_e$ their density and $e$ is the elementary charge.

A plasma also functions as an oscillating system with a characteristic frequency and it can be driven by the oscillations of external electric and magnetic fields as is the case in an intense laser beam. This characteristic frequency is called the *electron plasma frequency*, given as:

$$\omega_p = \sqrt{\frac{e^2 n_e}{\epsilon_0 m_e}} \tag{2.2}$$

with $m_e$ as the electron mass. An overdense plasma is a plasma with a density high enough to prohibit the light from simply transmitting as the EM oscillation frequency is smaller than the plasma frequency and so the plasma can react to the disturbance sufficiently fast to cancel it out. The boundary between the underdense and overdense state of a plasma is the so called *critical density* where the laser frequency is identical to the plasma electron frequency and resonance can take place [12, 13].

$$n_{cr} = \frac{m\epsilon_0\omega^2}{e^2} = 1.1 \cdot 10^{21}\,\mathrm{cm}^{-3} \left(\frac{\lambda}{\mu\mathrm{m}}\right)^{-2} \tag{2.3}$$

An important parameter which characterizes the vacuum-plasma interface is the scale length, which is a measure for the electron density gradient and is defined by

$$L^{-1} = \left| \frac{d}{dx} \log N_e \right|_{x=x_c} \tag{2.4}$$

with $N_e$ as the normalized electron density. [14]

Depending on the laser and plasma parameters involved, different absorption and acceleration processes occur, which will be treated in the following sections. Experimental results concerning absorption were reviewed by Davies [15] and fit functions were derived for the overall absorption of laser energy as well as for a specific population

of electrons, the so called fast or *hot electrons*, which will be discussed in upcoming sections in more detail. These results can be seen in figure 2.1.

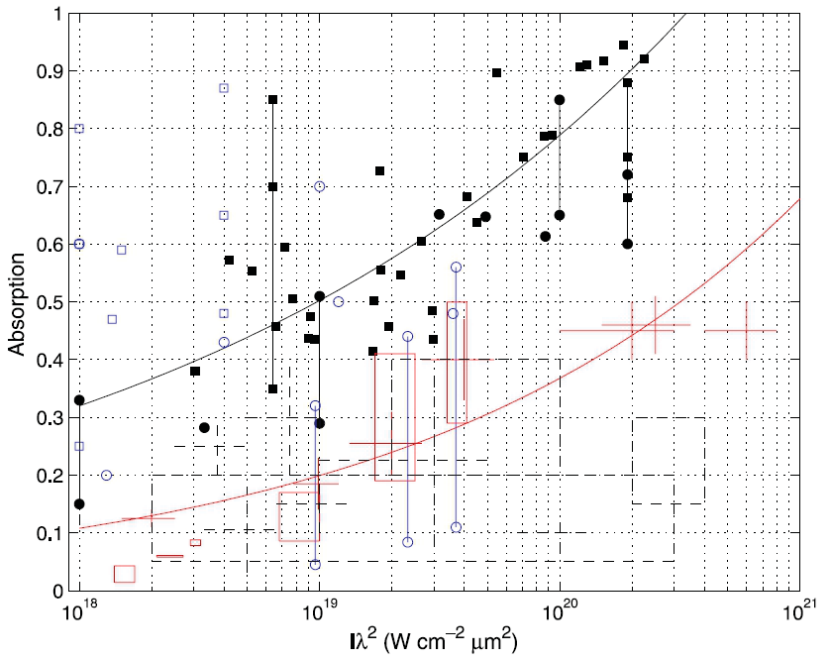


**Figure 2.1** – Absorption dependence on irradiance. The filled circles and squares denote results of absorption measurements under normal or near-normal and oblique incidence respectively. The black line indicates a fit to these results by Davies. The hollow blue symbols indicate numerical results. The red boxes and crosses indicate fast electron absorption measurements at the Nova laser. The red line is a fit to these results by Davies. Dashed crosses and boxes indicate other experimental measurement results for fast electron absorption. **Davies, Plasma Physics and Controlled Fusion, 51, 2009** [15]

We shall begin by considering interactions with individual atoms (first two sections) and after this by describing collective ionization and heating processes occurring in overdense plasmas.

### 2.2.2 Multi Photon Ionization and Above Threshold Ionization

The well known photoelectric effect [16] denotes the phenomenon that whether electromagnetic radiation can ionize a material at all does not depend on the radiation's intensity, but on its wavelength. The photon model [17] explained this by stating that electromagnetic energy comes in quantized packages called photons and only photons

with an energy $h\nu$ greater than the work function of the material can ionize it. This does not change with increased intensity, i.e. an increase in the number of photons.

However, at intensities above $10^{10}\,\mathrm{W/cm^2}$, i.e. at a high photon density in space and time, this simple picture no longer applies and several photons can indeed combine their energy to ionize the material in question even when single photons of this kind would not have been able to do this. This phenomenon is known as *multi photon ionization* and was first experimentally demonstrated by Voronov and Delone in 1965 [18]. *Above threshold ionization* is a more extreme case of the same principle, when multiple photons arrive in such a short amount of time as to combine their energy to an even higher degree, so that the electron in question is freed from the positive nuclear potential and then accelerated to velocities larger than the usual maximum value of $\sqrt{\frac{2h\nu}{m_e}}$. [14]

### 2.2.3 Tunneling Ionization and Barrier Suppression Ionization

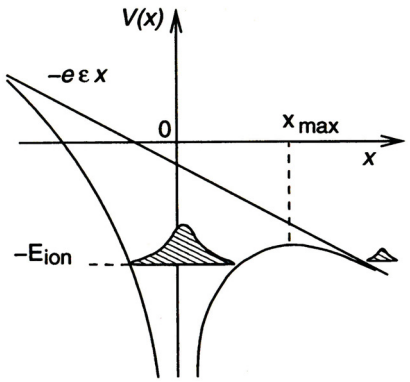


**Figure 2.2** – Tunneling ionization: An external field lowers the Coulomb barrier, so that the electron may tunnel out of the potential, leaving the atom ionized. If the field is even stronger than shown here, it can compensate the barrier entirely, thereby completely removing the electron from the influence of the core potential (barrier suppression ionization). **Gibbon, Imperial College Press, 2005** [14]

At even higher intensities a different effect takes place. If the electric field of the laser

is sufficiently strong to lower the Coulomb potential that the electron is trapped in, tunneling can take place or at even higher intensities the Coulomb barrier may be completely compensated and thereby the electron becomes unbound. This takes place at the appearance intensity of

$$I_{app} \approx 4 \cdot 10^9 \left( \frac{E_{ion}}{eV} \right)^4 Z^{-2} \tag{2.5}$$

where $Z$ is the ion core charge and $E_{ion}$ denotes the ionization potential of an atom with a charge of $Z - 1$.

These effects are known as *tunneling ionization* and *barrier suppression ionization (BSI)* respectively (see figure 2.2). To know whether the mechanisms in this section or those in the preceding one take precedence, the *Keldysh parameter* is quite useful:

$$\gamma = \omega_L \sqrt{\frac{2E_{ion}}{I_L}} \tag{2.6}$$

In general, where $\gamma > 1$ multi photon ionization occurs and at values smaller than one, tunneling ionization or BSI. [14]

### 2.2.4 Resonance Absorption

When a p-polarized electromagnetic wave impinges at an oblique angle of incidence onto a plasma surface, there is a component of the E field along the density gradient, which is not the case with s-polarized light, where the E-field is parallel to the surface. At the critical density (via tunneling as the wave does not reach there before it is reflected) a resonant Langmuir wave is excited (see figure 2.3). Later on, the energy of this electrostatic wave is absorbed by the plasma volume via damping and serves to heat the plasma. [19] Electrons heated by this process have a temperature

$$T_{hot} \approx 10(T_{keV} I_{15} \lambda^2)^{\frac{1}{3}} \,\text{keV} \tag{2.7}$$

where $T_{keV}$ is the bulk electron temperature in keV, and $I_{15}\lambda^2$ denotes the irradiance in units of $10^{15} \frac{\text{W}\mu\text{m}^2}{\text{cm}^2}$ [20].

The fractional energy absorption due to resonance absorption is governed by the following law:

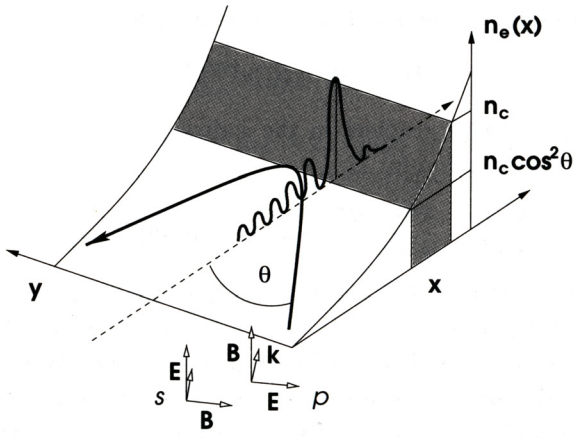


**Figure 2.3** – Resonance absorption: An incoming electromagnetic wave by a laser impinges on a plasma with a density ramp. In the case of p-polarization, there is an E-field component directed normal to the plasma surface, which excites a resonant plasma wave near the critical density. The wave moves into the plasma where it is eventually absorbed as heat. **Gibbon, Imperial College Press, 2005** [14]

$$\eta_{ra} = \frac{1}{2}\Phi^2(\xi) \tag{2.8}$$

where

$$\Phi(\xi) \approx 2.3\xi \exp\left(\frac{-2\xi^3}{3}\right) \tag{2.9}$$

is the Denisov function (see figure 2.4) and dimensionless parameter

$$\xi = (kL)^{\frac{1}{3}} \sin(\theta) \tag{2.10}$$

where $\theta$ is the angle of incidence, k is the wave number $k = \frac{2\pi}{\lambda}$ and $L$ is the scale length. [14] It is apparent that the absorption maximum is also the maximum of the Denisov function, which approximately corresponds to the condition $\xi = 1$.

If the density scale length becomes small compared to the quiver amplitude, resonance

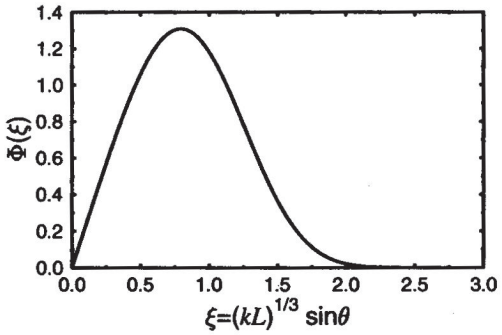


**Figure 2.4** – Denisov function, which determines the efficiency of resonance absorption. It depends on the wave vector $k$ and on the plasma's scale length $L$ which combine into the self-similar parameter $\xi$, with a maximum located close to the condition $\xi = 1$. Graph by Gibbon **Gibbon, Imperial College Press, 2005** [14].

absorption becomes impossible, for reasons discussed in the upcoming section. It is usually considered less important for high contrast, ultrashort laser-solid interaction experiments compared to other absorption mechanisms.

### 2.2.5 Vacuum Heating

At large density gradients with scale lengths

$$L < \frac{v_{os}}{\omega} \tag{2.11}$$

with

$$v_{os} = \frac{eE_0}{m_e \omega_L} \tag{2.12}$$

as the *quiver velocity* of an electron in a laser field with electrical amplitude $E_0$ [14], the critical density lies so close to the joint face of plasma and vacuum that the laser field inhibits the proper creation of an electrostatic plasma wave. Therefore energy transfer to the plasma by the resonance absorption mechanism becomes less efficient with smaller scale lengths [14]. While the laser field is strong enough to disturb a collective electron motion, its sharp decline inside the plasma due to the steep gradient allows individual electrons to be effectively accelerated by a different mechanism: A subgroup of electrons outside of the main plasma (see figure 2.5) will be accelerated into

the plasma on the first half of an oscillation by the laser E-field and then experience a weaker field pulling it outwards again on the second half of this oscillation. For this reason there is an energy transfer from the laser field to the electron and then from the electron to the plasma via collisions [21, 14]. This process, named *Brunel heating* or *vacuum heating* creates a population of "hot" electrons within the plasma. Its temperature scales with irradiance as follows:

$$T_{hot}^{GB} \approx 7(I_{16}\lambda^2)^{\frac{1}{3}} \tag{2.13}$$

where $I_{16}$ is the intensity in units of $10^{16}\,\frac{\mathrm{W}}{\mathrm{cm}^2}$ [14]. Vacuum heating contributes significantly to absorption once irradiance becomes greater than $10^{15}\,\mathrm{W}\mu\mathrm{m}^2/\mathrm{cm}^2$ [20]. While the temperature of the hot electrons depends on the intensity, the occurrence of the process itself depends on the scale length as does the kind of functional dependence of absorption on irradiance. Vacuum heating can only occur at angles of incidence other than $0\,^\circ$ because at normal incidence there is no electrical field component pointing across the critical surface.

Considering typical intensities of up to $10^{20}\,\mathrm{W/cm}^2$ with a central laser wavelength of 800 nm in the case of our laser system (see chapter 3 for a description) and applying inequality 2.11 leads to $L_{VH} = 860\,\mathrm{nm}$ as an estimate for the scale length below which resonance absorption will become inefficient and vacuum heating needs to be taken into account as an important laser energy absorption process.

### 2.2.6 $j \times B$ Heating and the Ponderomotive Potential

At highly relativistic intensities, the oscillating B field of the laser gives rise to yet another type of acceleration. Due to the Lorentz force, a force term arises:

$$f_x = -\frac{m}{4}\frac{\partial v_{os}^2(x)}{\partial x}(\cos 2\omega t) \tag{2.14}$$

This force oscillates at double the laser frequency. The reason for this is a shift in the sign of electron movement due to the acceleration caused by the E field as well as a similar, but out of phase shift in B field direction. This results in three switches of sign in the direction of the magnetic component of the Lorentz force

$$F_m = e\vec{v} \times \vec{B} \tag{2.15}$$

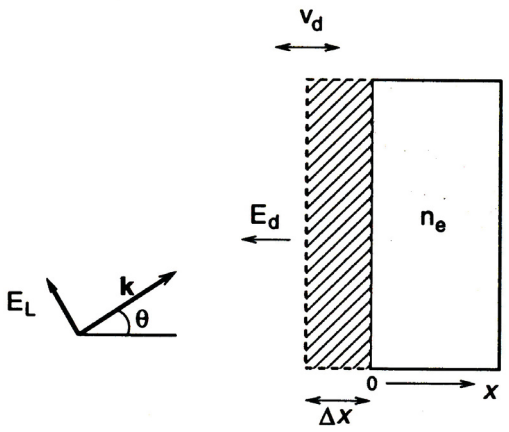


**Figure 2.5** – An illustration of vacuum heating. The driving field $E_d$, a standing wave caused by interference between the incoming and the reflected laser field, will pull out electrons from the plasma. A sheath with a thickness $\Delta x$ is created, before being sent back into the plasma, where its energy will be absorbed as the laser field attempting to pull it back is weakened by the overdense plasma. **Gibbon, Imperial College Press, 2005** [14]

during a single laser field oscillation, ie an oscillation at twice the frequency. This force can transfer energy to the plasma in a similar fashion as described in the case of vacuum heating in the previous paragraph. This absorption mechanism is called $j \times B$ *heating* and is also known as the *oscillating ponderomotive force* [22, 14]. An important difference between these two modes of absorption is that during vacuum heating electrons are being accelerated along the density gradient while in the case of $j \times B$ heating electrons are being accelerated along the propagation direction of the laser. [14, 23] Another difference is that in contrast to vacuum heating, this process is most efficient at normal incidence as the $\vec{j} \times \vec{B}$ vector is normal to the critical surface in this geometry.

Strictly speaking, the ponderomotive force is no heating mechanism, just an electron acceleration mechanism by means of intense laser light. However, it can affect and cause heating processes. An electron in an intense laser field oscillates with a quiver velocity $v_{os}$ (see 2.12).

$$v_{os} = \frac{eE_0}{m_e\omega} \tag{2.16}$$

The electron oscillates with less energy in a less intense field. By arguing in terms of energy minimization an assorted potential can thus be introduced, namely the *ponderomotive potential* along with an assorted force, the *ponderomotive force*:

$$f_p = -\frac{e^2}{4m_e\omega^2}\nabla E_0^2 \tag{2.17}$$

where $\omega_0$ is the laser frequency [14]. In practice this ponderomotive force has the effect of driving electrons out of regions of intensely focused laser light, as can be seen from the formula above, where $f_p$ is proportional to the gradient of the intensity. The ponderomotive potential scales as follows with *irradiance* ($I\lambda^2$):

$$U_p = \frac{e^2E_L^2}{4m_e\omega_L^2} \approx 1MeV\sqrt{\frac{I\lambda^2}{10^{19}\frac{W}{cm^2}\mu m}} \tag{2.18}$$

[14, 24]

Using the ponderomotive potential, the electron movement can be described in a straightforward way in a hydrodynamic picture. Considering an electron fluid element near the plasma-vacuum interface, its equation of motion is as follows:

$$\frac{\partial\vec{p}}{\partial t} + \vec{v}\cdot\nabla\vec{p} = -e(\vec{E} + \vec{v}\times\vec{B}) \tag{2.19}$$

with $\vec{p}$ as the momentum. This can be rewritten into an equation for the longitudinal component of the fluid element, using the ponderomotive potential:

$$\frac{\partial\vec{p}_L}{\partial t} = e\nabla\Phi - \nabla U_P \tag{2.20}$$

with $\Phi$ as the electric potential. [20]

### 2.2.7 Anomalous Skin Effect and Sheath Inverse Bremsstrahlung

Another heating mechanism that occurs in plasmas with sharp density gradients is the *anomalous skin effect*. This effect denotes the situation when the temperature of the electrons that are heated within the skin layer becomes so large that their mean

free path length exceeds the skin depth, meaning that the heated area is expanding into the overdense plasma beyond the reaches of the laser field [14]. This is similar to the vacuum heating mechanism in that both concern electrons entering overdense layers of plasma by means of kinetic energy acquired from the laser field within a single oscillation period of its electrical field.

If the transit through the skin layer takes longer than one laser period, the laser can interact over several oscillations with the electron. The electron is being reflected from the electron sheath which forms at the edge of the plasma and gains energy with each reflection until it leaves the skin depth in a process known as *sheath inverse bremsstrahlung*. [25, 14]

Yang and Kruer [26] have shown -at least for normal incidence and a moderate intensity range implicit in equation 2.21- that the anomalous skin effect and sheath inverse bremsstrahlung absorption can be considered two limiting cases of the same set of equations describing a single collisionless absorption mechanism. Which mechanism of the two dominates depends on the electron velocity and on the ratio of laser to plasma frequency. The case of $(\frac{\omega}{\omega_p})^2 \gg (\frac{v_e}{c})^2$ implies SIBS, whereas $(\frac{\omega}{\omega_p})^2 \ll (\frac{v_e}{c})^2$ means the anomalous skin effect is going to be the decisive mechanism.

ASE as well as SIBS require for the light pressure $P_L$ to be smaller than the plasma pressure $P_e$ as opposed to the cases of resonance absorption or vacuum heating. This condition can be expressed in two ways:

$$\frac{P_L}{P_e} = \frac{2I_0/c}{n_e k_B T_e} \approx \frac{660 I_{18}}{160 n_{23} T_{keV}} < 1 \tag{2.21}$$

where $I_{18}$ refers to intensity in units of $10^{18}\,\mathrm{W/cm^2}$, $n_{23}$ to the electron density in units of $10^{23}\,\mathrm{cm^{-3}}$ and $T_{keV} = \frac{T}{\mathrm{keV}}$. The condition's alternative formulation is

$$\frac{v_{os}^2}{v_{te}^2} < \frac{n_e}{n_{cr}} \tag{2.22}$$

where $v_{te}$ refers to the electron's thermal velocity, while $v_{os}$ is its quiver velocity in the laser field. [14]

Equation 2.21 is a useful guide for given experimental conditions to determine which pair of absorption mechanisms will be relevant, whereas equation 2.22 allows for a more intuitive understanding in the sense that the type of absorption mechanism depends on the dominant type of electron motion, either the thermal one or that induced by the laser. If thermal motion is dominant, anomalous skin effect and/or sheath inverse

bremsstrahlung will determine the absorption. If the quiver motion dominates, then resonance absorption or vacuum heating (presumably $j \times B$ heating as well) will be the relevant processes for absorption of laser energy in plasma.

## 2.3 Target Normal Sheath Acceleration

The first laser-driven ion acceleration process we shall discuss is *Target Normal Sheath Acceleration* or TNSA. The process operates as follows: The prepulse is ionizing a thin foil with a thickness on the order of $10^{-6}\,\mathrm{m}$. The level of the prepulse is crucial as it determines the scale length of the pre-plasma, which in turn affects the efficiency and mode of laser energy absorption. The prepulse level depends on the laser contrast, which denotes the ratio between ASE intensity and the main pulse's intensity. Means to improve the contrast will be discussed later in this work.

Afterwards the intense main pulse of a focused laser beam (intensities on the order of $10^{18}\,\mathrm{W/cm^2}$) drives out electrons via the ponderomotive force. Huge E-fields (on the order of TV/m) are created at the rear side of the target by electrons which form a sheath on the rear side and field-ionize contaminants on the foil surface (creating p+, carbon-, oxygen- and nitrogen ions in the process) which are then accelerated normal to the rear target surface.

Their energies in our case are on the order of up to 15 MeV and display a two temperature thermal spectral distribution, limited by a cutoff energy. The hot and cold temperatures correspond to the hot electrons and bulk respectively. The proton beam has a divergence of up to $20\,^\circ$, depending on the proton energy. [27, 28]

Figure 2.6 shows the main features of this process. In the following subsections its individual stages will be described in further detail.

### 2.3.1 Effects of Prepulse on Target

There is always laser radiation leaking onto the target before the main interaction, in the form of amplified spontaneous emission during pumping or due to pulses passing through the system before the main pulse. The *laser contrast*, which is the ratio in intensity between this pedestal and the main pulse is an important parameter with far ranging effects on the interaction physics. This *prepulse* ionizes the target front and creates a preplasma with a typical scale length $L/\lambda$ of $0.01 - 0.1$ [14]. For this reason the main pulse never interacts with a solid medium, but instead with an overdense

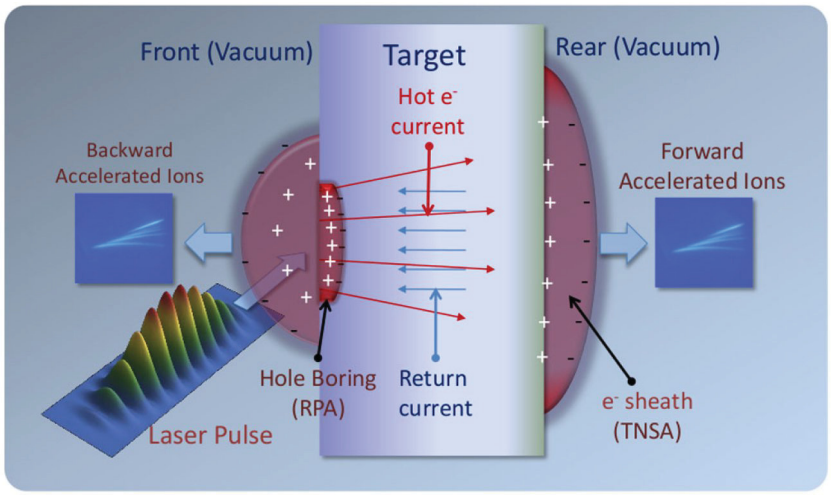


**Figure 2.6** – An illustration of the TNSA mechanism. A laser pulse impinges from the left at an angle. Hot electrons, being accelerated into the target, indicated by red arrows, form a sheath on the rear side, which accelerates ions normal to the target rear side. The graphic also indicates that there is ion acceleration on the front side, but with less advantageous emissivity. There is also a so-called hole-boring effect at the front side due to the laser pressure, which will be discussed in detail in section 2.5. **Macchi et al, Review of Modern Physics, 85, 2013** [13]

plasma limited by a border region with a density profile determined by the prepulse. It also sends a shockwave into the target, which eventually deforms the target's rear side. This has a negative effect on the TNSA mechanism if the deformation takes place before the ion acceleration (see figure 2.7). [28]

In general TNSA is more effective for thinner targets as the maximum electrostatic field at the rear is antiproportional to the square of the thickness, due to the increased electron density at the rear side[29]. However, this destructive effect of the prepulse limits the minimal usable thickness. For this reason, an improved contrast is advantageous if one wants to use thinner targets and improve the interaction. A more in-depth discussion of laser contrast as well as means to improve it –such as an *XPW system* or a *plasma mirror*– can be found in other parts of this thesis (sections 3.2.3 and 3.4 respectively). For this reason, TNSA at the front side is much less efficient as the front side has been deformed by the prepulse and has expanded by the time the main pulse arrives, whereas the rear side remains unperturbed, provided the shockwave has not arrived yet.

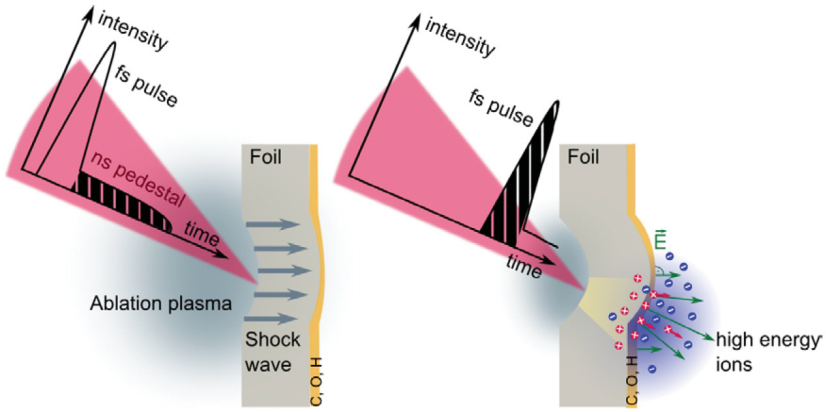


**Figure 2.7** – Deformative effect by shockwave caused by amplified spontaneous emission pedestal. **Zeil et al, New Journal of Physics, 12, 2010** [28]

### 2.3.2 Impact of Main Pulse on Pre-Plasma

Once the main pulse interacts with the pre-plasma a population of hot electrons is generated via jxB heating and other heating mechanisms described previously. It forms an electron cloud which expands into the target and beyond. The absorption of laser energy into hot electrons depends on the experiment, but is often in a range of $10-30\,\%$, although it can also be much higher than that [13]. According to theory the temperature of hot electrons scales with the ponderomotive potential as follows

$$T_{hot} \propto m_e c^2 \sqrt{\left(1 + \frac{2U_p}{m_e c^2}\right)} = \sqrt{{m_e}^2 c^4 + 2U_p m_e c^2} \tag{2.23}$$

[30, 31]. However, experimental results [32] indicate that the ponderomotive scaling overestimates the hot electron temperature. An experimental scaling by Beg [33] which later was refined within a theoretical approach by Haines [34] gives the following scaling (see figure 2.8) for a laser of wavelength $1\,\mu$m:

$$T_{hot} = 215(I_{18}\lambda_{\mu m}^2)^{\frac{1}{3}} \tag{2.24}$$

These hot electrons then move into the target with current densities of up to $j_h = 4.8 \cdot 10^{12}\,\mathrm{Acm}^{-2}$.[13] As these currents would create a magnetic field strong enough to pinch the current and which contained more magnetic energy than in the laser, there has to be a return current, which almost entirely neutralizes the current by the hot

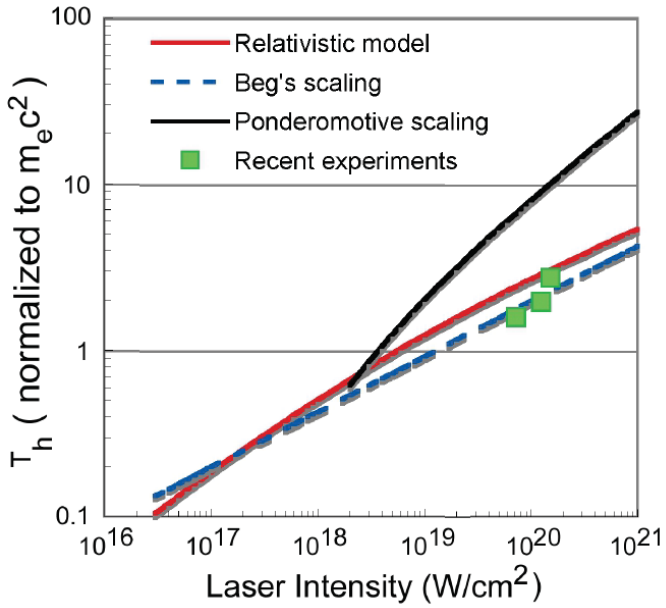


**Figure 2.8** – Different scalings for hot electron temperature dependence on intensity. The black curve indicates the ponderomotive scaling, green squares indicate experimental results from 10 years ago strongly disagreeing with that scaling. The blue curve is Beg's scaling [33], based on earlier experimental results, whereas the red curve is based on a relativistic mode developed by Haines, Beg and others. **Haines et al, Physical Review Letters, 102, 2009** [34]

electrons. [14] As it reaches the rear side of the target a layer of contaminants (a few nanometer thick [35]) is ionized by field ionization. These contaminants result from water vapor or pump oil and consist of hydrogen, carbon, oxygen and nitrogen, with nitrogen less common than the others. If the target is sufficiently heated via current or by other methods it is possible to remove this layer in order to accelerate the target constituents themselves [29, 36]. However, in the experiments described in this work, this was not done and in the case of the biological experiments would actually have been counterproductive as we were interested in the protons.

### 2.3.3 Debye Sheath and Ion Acceleration

The electrons form a *Debye Sheath* close to the ionized rear surface of the target with a Debye length $\lambda_D(T_{hot}, n_{e_{hot}})$. This sheath creates an electric field on the order of $TV/m$.

$$E_s \approx \frac{k_B T_{hot}}{e\lambda_D} \tag{2.25}$$

This electrostatic field only lasts a short while once the interaction with the laser field has stopped as it is only maintained due to a continuous replenishment with hot electrons from the target front, because the electrons in the sheath are rapidly pulled back into the bulk of the plasma by $E_s$. This process is known as recirculation. As soon as these electrons stop arriving (which happens after a time on the order of 100 fs after the start of the main interaction) electron recirculation comes to an end. [29, 31]

The precise acceleration time $\tau_{acc}$ depends on the pulse duration as well as on the intensity [37, 29]:

$$\tau_{acc} = \alpha(\tau_L + t_{min}) \tag{2.26}$$

where $\alpha$ is intensity dependent with values ranging between 1.3 at an intensity of $3 \cdot 10^{19}\,\mathrm{W/cm^2}$ and above and 3 at an intensity of $2 \cdot 10^{18}\,\mathrm{W/cm^2}$ and below. At intensities between those two values, $\alpha$ varies linearly.

$$t_{min} = 60\,\mathrm{fs} \tag{2.27}$$

is the minimal acceleration time and $\tau_L$ is the duration of the laser pulse.

This time is long enough to transfer some energy to the protons via the sheath field. The protons are first as they have the highest charge to mass ratio and therefore experience the strongest acceleration

$$a = E_s \frac{q}{m} \tag{2.28}$$

$C^{6+}$ and $O^{8+}$ ions experience a field that has already been screened by the protons to some extent and which is therefore weaker. They in turn screen the field for ions with an even smaller $\frac{q}{m}$ and after the initial phase the ions along with the electrons move in a plasma cloud in the direction normal to the target surface.

The movement of the ion cloud can be calculated by using the equations of continuity and motion:

$$(\partial/\partial t + v_i \partial/\partial x) v_i = -(Ze/m_i)\partial\Phi/\partial x \tag{2.29}$$

$$(\partial/\partial t + v_i \partial/\partial x) n_i = -n_I \partial v_i / \partial x \tag{2.30}$$

where $v_i$ is the ion speed, $\Phi$ the electrical potential (which fulfills the Poisson equation and is also present in the Boltzmann distribution for the hot electron density), Z is the degree of ionization, $n_i$ the ion density, x the direction of propagation and t is the duration of acceleration. Using these simple ingredients it is possible to come up with a formula for the resultant ion spectrum:

$$dN/dE = \left( \frac{n_I c_s t}{\sqrt{2 E E_0}} \right) \exp(-\sqrt{2E/E_0}) \tag{2.31}$$

where $c_s$ is the speed of sound in the plasma, $E$ the ion energy and $E_0 = Z k_b T_{hot}$. [38]

Another characteristic property of the ion bunches produced by the TNSA mechanism is a low emittance which is a measure of the beam quality. The transversal emittance can be less than $0.004\pi$ mm while the longitudinal emittance can be less than $10^{-4}$ eVs. Typical particle numbers accelerated by one interaction are on the order of $10^{13}$. [29]

## 2.4 Collisionless Shock Acceleration

One way to describe waves is by the movement of certain values of physical properties in space and time (for example pressure, density or local velocity in the case of ordinary sound waves in a gas). Usually, these characteristic curves can't intersect because at any given point in space and time a certain quantity can only have a single value. If the characteristics do cross, there is a breakdown in the continuity of flows which creates a discontinuity. [39]

Such discontinuities in flow variables can also propagate and are known as *shock waves*. In the case of shocks in a collisionless plasma the wave starts out as a soliton. The wave front of this soliton steepens due to non-linear effects. This steepening at some point is stopped by dispersion which tends to widen peaks and a shock wave with a finite thickness results of this equilibrium. The usual dissipating mechanisms due to collision are much too slow in collisionless plasmas and are of no relevance, but dispersion plays a similar role instead. [40]

In our case there are discontinuities in electron density as well as in temperature. The jump in electron density has a two-fold effect: An electrostatic potential hill is created together with a difference in plasma velocity between the two plasma slabs due to

conservation of flow: where density is lower, velocity is increased. To put it differently, in the shock frame there is a constant plasma flow hitting upon an electrostatic potential hill with this increased velocity, $v_s$. Conversely, in the lab frame, the shock is moving through the plasma with velocity $v_s$ (see figure 2.9(a)).

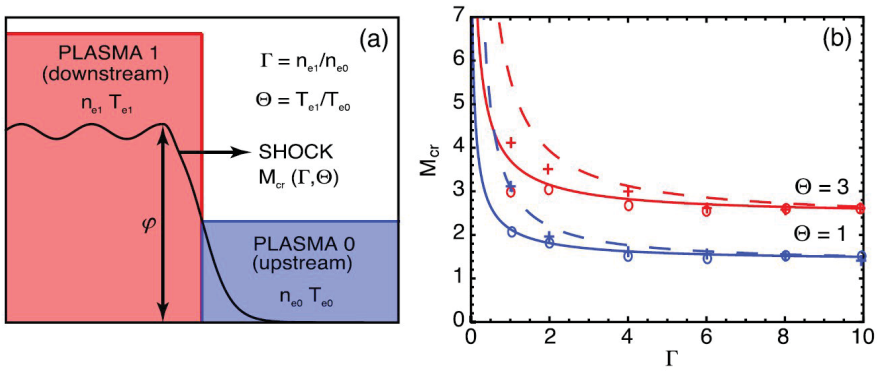


**Figure 2.9** – a) Internal shock structure: Two plasma slabs (depicted in red and blue) are in contact, each with their own electron density and temperature. There is an electrostatic potential difference (black curve, with $\varphi$ as the higher potential in plasma slab 1). The structure as a whole moves along the direction of the electrostatic gradient. Particles may either be trapped in the modulations of the electrostatic shock structure in plasma slab 1 or may be reflected from the shock near the interface between both plasma slabs. b) Electron density ratio $\Gamma$ as well as temperature ratio $\Theta$ determine the critical Mach number of the shock, ie the velocity necessary for ion reflection to occur. Pluses and circles indicate simulation results based on velocity measurements. **Fiuza et al, Physical Review Letters, 109, 2012** [41]

Depending on the kinetic energy of the ions impinging on the shock wave different things can happen. If the kinetic ion energy is much higher than the electrostatic potential energy, they cross the potential hill and are slowed down by it. If their energy is just a bit higher than the electrostatic energy they become trapped in the shock potential structure and move along with it from then on. In case that they have less energy they are reflected from the shock and their final velocity after reflection is

$$v_r = 2v_S - v_b \tag{2.32}$$

where $v_b$ is the velocity in forward direction before the impact of the shock wave. The critical case is when both energies are equal and the wave's Mach number in this case is known as the *critical Mach number*:

$$M_{cr} = \sqrt{2\Theta\left(\frac{1+\mu_{e0}}{\Gamma(1-\mu_{e0}/\Theta)}+1\right)} \tag{2.33}$$

with

$$\Gamma = n_{e1}/n_{e0} \tag{2.34}$$

as the electron density ratio,

$$\Theta = T_{e1}/T_{e0} \tag{2.35}$$

is the electron temperature ratio, with the subscript 1 denoting a property of the downstream plasma and 0 denoting a property of the upstream plasma respectively. Furthermore,

$$\mu_{e0} = \frac{m_e c^2}{k_B T_{e0}} \tag{2.36}$$

Ion reflection occurs when $M_S = \frac{v_s}{c_{s0}} > M_{cr}$, which is equivalent to the condition that the electrostatic energy potential difference exceeds the kinetic energy of the impinging upstream ions in the shock frame. High electron density ratios and low temperature ratios lead to the lowest critical Mach number, ie the most advantageous conditions for ion reflection (see figure 2.9(b)). [41]

## 2.5 Radiation Pressure Acceleration

Another acceleration mechanism is *Radiation Pressure Acceleration* (RPA), which as the name suggests, is based on the light's radiation pressure

$$p = I_L/c \tag{2.37}$$

where $I_L$ is the intensity and $c$ the speed of light in vacuum. For this reason it also requires much thinner foils than TNSA (on the order of several nm, but the precise value depends on the laser system used).

There are several phases and different 'regimes' that can be distinguished, with *hole boring* (HB) as the first one. The HB phase is characterized by the creation of a compressed electron layer created by the ponderomotive force. In order for this to work smoothly it is necessary for the laser focus to be relatively large compared to the targeted foil area as well as homogeneous in intensity so as to accelerate the foil as a

whole and avoid additional heating in the outer regions once the foil begins to bend due to the stronger acceleration in the centre. It is also important to avoid heating in general as much as possible, as otherwise electrons are going to leave the compressed area and the foil might explode (see figure 2.10) [42]. The ideal is an adiabatic compression process, which is entirely different from TNSA where the ion energy increases with the hot electron temperature.

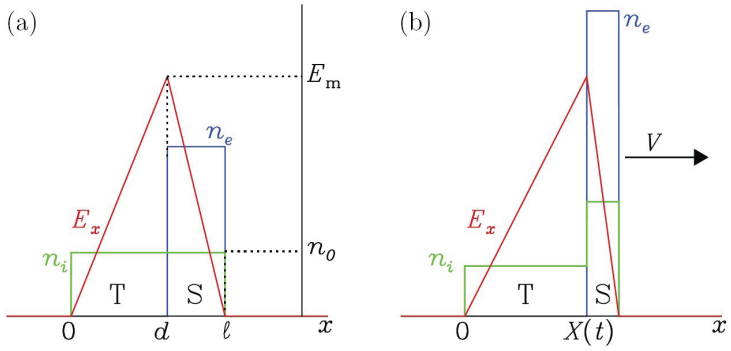


**Figure 2.10** – a) The laser pushes out some electrons from one part of the target (T) into a compression layer (S) with increased electron density $n_e$. The tail area T is charged positively as only ions remain, whereas the compression area is charged negatively. b) Some ions have been pulled into the compression area S and are now being accelerated together with the electrons due to their strong electrostatic field while the electrons continue being pushed by the laser. The tail area T undergoes a Coulomb explosion. **Macchi et al, New Journal of Physics, 10, 2010** [43]

A setup with a steep overdense target, normal incidence and circularly polarization pulses at a high contrast is generally preferred so as to avoid components of the electrical field going into the target as well as $j \times B$ heating[42]. However, there have been results reported with RPA by means of linearly polarized light [44] and there is even a theoretical prediction that at extreme intensities ($I \approx 10^{23}\,\mathrm{W/cm^2}$) RPA at linear polarization would become more effective than TNSA. [45, 46]

Along with the electron compression area described earlier a corresponding electron depletion area is created within the target. The electrical field between the two areas creates a force opposite to the radiation pressure and can be calculated as follows:

$$E_{RPA}^2 = \frac{2(1+R)}{\epsilon_0 c} I_L \tag{2.38}$$

This first phase of the process comes to an end once an equilibrium between the radi-

ation pressure and the electrostatic field has been established.

If the target is smaller than the thickness of the required depletion area, $l_d$, an equilibrium cannot be achieved and the electrons will leave the target area. Therefore, this constitutes a lower limit for target thickness in RPA:

$$l_d = \sqrt{\frac{2(1+R)I_L\epsilon_0}{cn_0^2e^2}} = \frac{\lambda n_c a_0}{n_0} \tag{2.39}$$

with $n_0$ as the electron density in the target before the interaction, R as the target's reflectivity and $a_0$ as the dimensionless laser amplitude defined by the equation

$$a_0 = \frac{eE_L}{m_e c\omega_L} \tag{2.40}$$

[14].

After equilibrium has been achieved, the ions in the compression area are accelerated in laser direction by this field, which also exists within this area. The ion velocity is given by:

$$v_i = \sqrt{\frac{\epsilon_0 E_{RPA}^2}{\rho}} \tag{2.41}$$

with $\rho$ as the ion mass density. The acceleration of the ions to this velocity occurs on the time scale of the inverse ion plasma frequency. [42]

The electrons quickly catch up. This process continues as the compression layer moves through the entire target. Once it reaches the edge of the target and enters into the vacuum the whole target has been accelerated as a single plasma slab driven by the radiation pressure, not unlike a sailing boat driven by the wind, hence this phase is known as *light sail* (see figure 2.11). This process continues until the laser pulse is over. Meanwhile, the ions left behind in the depletion layer undergo a Coulomb explosion. [47]

In principle RPA should lead to monoenergetic spectra because all particles have the same velocity, but in practice the best that can be hoped for are monoenergetic features as the peak becomes broader once the laser pulse is over and the plasma is left to its own devices and experiences Coulomb forces by fast electrons. [42, 31]

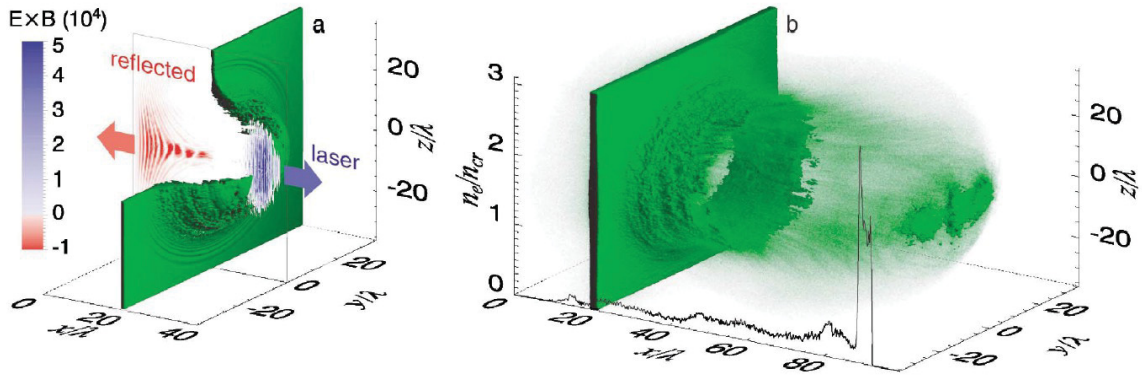


**Figure 2.11** – The images depict two isosurfaces of constant ion density (green) in space for two different times in a simulation [46], a) $n = 8n_{cr}$ at $t = 40 \cdot 2\pi/\omega$ and b) $n = 2n_{cr}$ at $t = 100 \cdot 2\pi/\omega$. In image a), the upper left quarter of the foil is left out in order to show the interior. The laser and its reflected part are also shown. In b), the normalized ion density depending on position is shown as the black curve near the x-axis. **Esirkepov et al, Physical Review Letters, 92, 2004** [46]

## 2.6 Review of Ion Acceleration Mechanisms for Therapeutic Usability

Each acceleration mechanism has its drawbacks and advantages for medical application. One advantage of TNSA, the mechanism that is relevant for the largest part of this thesis, is the relative ease in applying the mechanism and its stability. One can shoot hundreds of times and each time there is a TNSA signal resulting. In addition it is relatively easy to construct a tape target with suitable material. For RPA the target has to be on the order of nanometers and this makes it very difficult to construct a tape target that doesn't tear due to the mechanical strain of acceleration. A disadvantage of TNSA is the quasi-thermal spectrum where for an application monoenergetic particles would be perferred or even necessary in order to target a specific region of tissue. Here, RPA would clearly be an advantageous process to use. On the other hand, depending on the width of the targeted tissue a tailored spectral range out of a wider spectrum could be useful as opposed to quasi-monoenergetic features achieved by RPA. If the position of this peak were controllable, a similar overall irradiation could also be achieved by successive RPA shots.

In terms of the required energy of 250 MeV to reach the deepest tumors, there is

currently no laser-driven particle acceleration process that reaches these energies (see figure 2.12 by Zeil et al for a review of results in 2010), but this is only a matter of applied laser intensity and will most likely be overcome in time as available laser power increases with new petawatt facilities such as ELI being commissioned.

Simulation results are promising cutoff energies in the range of hundreds of MeV/nucleon [44] as shown in figure 2.13.

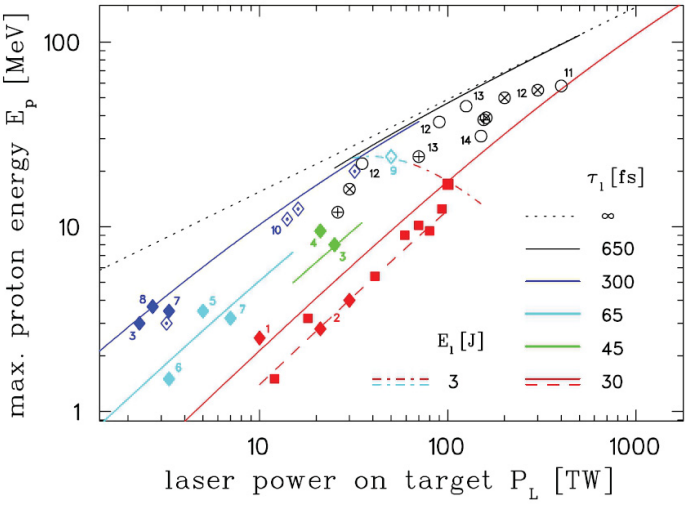


**Figure 2.12** – The maximum proton energy achieved in a number of experiments, depending on the laser power. Different colors denote different pulse durations. The dotted black line denotes an expected fit for the case of a continuous wave laser. It is apparent that for higher pulse duration, ie higher overall energy on target, the proton cutoff energy increases. **Zeil et al, New Journal of Physics, 12, 2010** [28]

If one were to reach such higher energies, one probably would have to switch to electromagnets as the magnetic flux needed to separate 250 MeV from 251 MeV protons by 1 mm at the exit of the magnets would have to go up to $B > 10\,\mathrm{T}$ in a similar geometry as in our experiments. For comparison, the magnetic yokes used in our setup, as described in chapter 4, had an average $B \approx 850\,\mathrm{mT}$.

Finally there is also the possibility that further acceleration mechanisms may be discovered or improved upon, such as the break out afterburner process, which has been used to explain monoenergetic features in ion spectra with reported energies of up to 1 GeV, corresponding to $\approx 83\,\frac{\mathrm{MeV}}{\mathrm{nucleon}}$. [48]

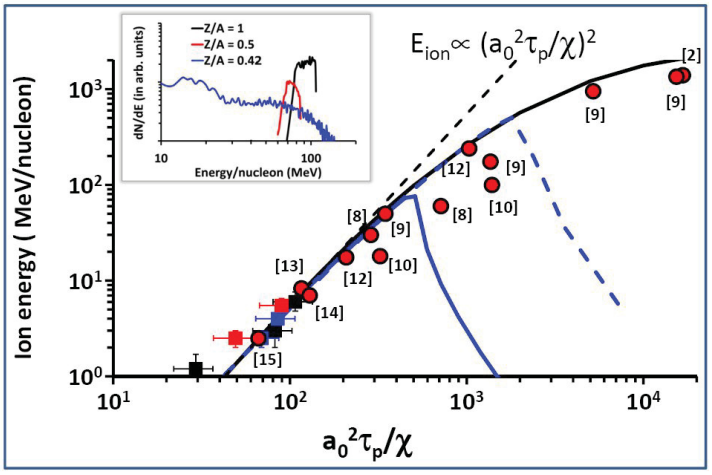


**Figure 2.13** – Scaling by Kar. Squares indicate experimental results, circles indicate simulation results, showing up to 1 GeV per nucleon. Lines indicate different scaling approximations as detailed within the paper. [44] The inlet shows a spectrum from one of the simulations, indicating peaks in the ion energy spectrum. **Kar et al, Physical Review Letters, 109, 2012** [44]

# Chapter 3

# ARCTURUS Laser System

## 3.1 Introduction

The ARCTURUS laser system contains two 200 TW beams which allow us to reach intensities on the order of $10^{20}\,\mathrm{W/cm^2}$ in the interaction area. Such intensities can only be achieved due to the introduction of the principle of chirped pulse amplification (CPA) [8] as otherwise optical components during the amplification process would be damaged as soon as the fluence achieves values above $0.16\,\mathrm{Jcm^{-2}} \cdot \tau/\mathrm{ps}$ with $\tau$ as the pulse duration. [14] The key to the CPA technique is to first stretch or 'chirp' the pulse, reducing its power this way, then to amplify the chirped pulse so that it still remains below the optics' damage thresholds and finally to compress it again temporally, achieving intensities above the damage threshold. The change in pulse duration is achieved by the use of several diffraction gratings, which cause different wavelengths of the laser pulse to travel different optical distances, arriving at the exit of the stretcher device at different times or reverting this difference in the case of the compressor device, so that different frequencies arrive at the same time, making the pulse short again.

In the case of the ARCTURUS facility there are two CPA stages involved, one in the preamplifying frontend and the other employed for the main amplification process of the beams. In this section these two stages will be discussed as well as the main component devices of the laser system as they were at the time of the experiments dicussed in this work.

## 3.2 Frontend

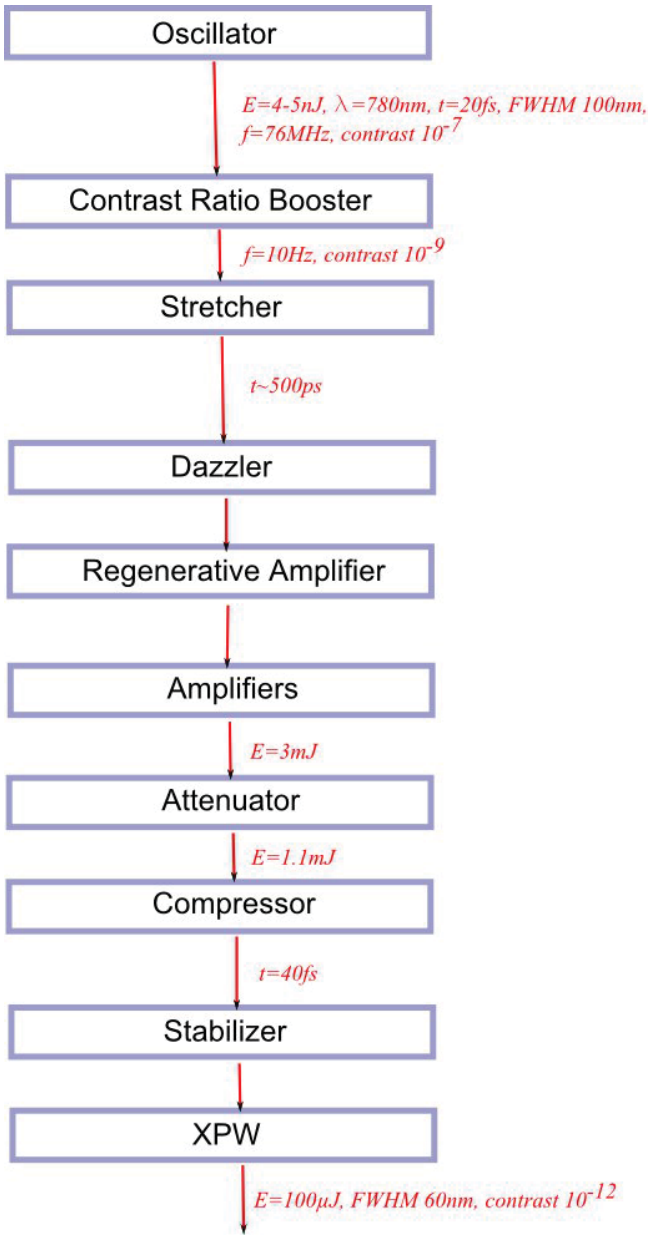


**Figure 3.1** – Schematic of the frontend of the ARCTURUS laser system containing first CPA stage and XPW

### 3.2.1 Oscillator

The laser system consists of multiple components. At the beginning of this chain there is a Ti:Sa oscillator which generates pulses of $\approx 25\,\text{fs}$ duration at a frequency of 76 MHz. Each of these pulses has an energy of $\approx 4 - 5\,\text{nJ}$, a central wavelength of 780 nm and a spectral FWHM of $\approx 100\,\text{nm}$. [49]

### 3.2.2 Contrast Booster and PreAmplifier

Next the pulses enter the so-called contrast booster, where a pulse picker reduces their frequency to 10 Hz and where they are amplified to energies in the mJ range. Due to a saturable absorber the contrast improves by two orders of magnitude. Next, the pulses are stretched for the first time to $\approx 500\,\text{ps}$ before being further amplified in a regenerative amplifier -comprising a pumped crystal in a cavity, seeded by the pulse-, as well as a five pass butterfly pre-amplifier, before being attenuated again to 1.1 mJ. After this the pulses are recompressed and the first CPA stage is complete. [50, 51, 49, 52]

### 3.2.3 Wizzler and XPW

The XPW device is a fibre in which a process takes place which improves the pulse's contrast. This process is called cross polarized wave creation (abbreviated as 'XPW' where the 'X' indicates the crossed direction of the polarizations involved). In this process a wave of a polarization perpendicular to the incoming one is created in an anisotropic medium with a proportionality to $I^3$ where I is the intensity of the incoming beam. Given that this process is so highly nonlinear, it is clear that this can increase the contrast as weaker parts of the beam (prepulses, ASE) produce far less of these perpendicularly polarized components. At the exit of the fibre the pulses therefore have improved contrast, but a lot less energy, only $\approx 100\,\mu\text{J}$. A Wizzler[1] is used in order to measure the pulse at this point and to see whether the process has the desired results. The contrast achieved can be on the order of $10^{-12}$ [50, 52].

### 3.2.4 Stretcher

Next the beam is coupled into the stretcher for the second, main CPA cycle. The pulses are stretched to $\approx 500\,\text{ps}$ by means of a telescope construction and two gratings.

[1] by FastLite

The stretching occurs due to dispersion which leads to beam paths of different lengths depending on the wavelengths of the different pulse components. A chirp is introduced. [51, 49, 52]

### 3.2.5 Dazzler

The Dazzler[2] is a programmable dispersive filter and in our case is used to control the phase of the pulse after it passes the stretcher. This comes in handy when compensating for phase-distortions created during the subsequent path of the beam. Its main components are an accousto-optic crystal made of $TeO_2$ and a radio frequency generator. [53, 52]

### 3.2.6 Regenerative Amplifier, Mazzler and Pre-Amplifier 2

Afterwards the pulse enters a second regenerative amplifier which also contains a Mazzler[3]. The Mazzler is a programmable gain filter and is used to control the spectral shape of the pulse. This is necessary due to the phenomenon of gain narrowing, which occurs due to certain frequency ranges being amplified preferably, which has an effect on the FWHM of the pulse. The Mazzler, similarly to the Dazzler, also uses an accousto-optic crystal. The frequency component which could be subject to gain-narrowing is diffracted out of the beam path for the most part. The Mazzler is integrated in a regenerative amplifier and its settings are changed in an iterative process in order to optimize the output spectrum. [54, 55] After that, the beam goes through another amplifier with a butterfly geometry. [49, 52]

## 3.3 Main Amplification Stages and Compression

Next, the beam is amplified via pumping and then separated into two main beams and a probe beam (see figure 3.2) with an energy distribution of 70 % for the main beams and 30 % for the probe beam. Each of the main beams is then amplified further in several stages. This amplification works by pumping titanium sapphire crystals with frequency doubled Nd:YAG lasers at a wavelength of 532 nm. The stored energy is then picked up by the seed pulse going through the crystal in several passes. In order to reduce the fluence in order to avoid damage of optical components, the beam is

[2] by FastLite
[3] by FastLite

widened to approximately 8 cm in diameter by two lenses in a telescope setting. The amplified pulse is then compressed in a compressor that consists of two grating pairs which compensate the chirp introduced by the stretcher. The compressed pulses have a duration of approximately 25 fs and an energy of approximately 3 J [55, 52]. Optionally their contrast can be improved further by sending them through a plasma mirror, which will be described in the following section.

## 3.4 Plasma Mirror Construction and Characterization

### 3.4.1 Basic Principle of a Plasma Mirror

Like the XPW (see section 3.2.3), a plasma mirror is a means to improve the laser contrast, i.e. the ratio between peak and prepulse or ASE intensity. This is achieved by focusing the beam with a parabolic mirror onto an antireflectively coated glass substrate which is very transparent ($> 99.75\,\%$ of laser light passes through in our case[4]) until it becomes ionized. Therefore the prepulse is transmitted whereas the main pulse with its leading edge ionizes the substrate surface and is reflected by it. The reflected pulse has an increased contrast as the prepulse has been filtered out. In order to transport the beam further along the beam line, it has to be recollimated by a second parabola which compensates the divergence introduced by the first one in a telescope-like setting in which the parabolas' optical distance is twice their focal length.

A basic requirement for the geometry of a plasma mirror is to limit the intensity in order to prevent a premature plasma ignition of the substrate which would lead to reflection of part of the prepulse. In this case the plasma mirror surface would also no longer be flat when the main pulse arrives and would distort the beam propagation. This can be avoided by making the beam area on the substrate sufficiently bigger than the area in the focal plane: The parabolas are placed in such a way that the focus is located in front of or behind the substrate. One has to make sure in order to maintain a telescope-like setup of the parabolas that the deviation from the "ideal focal position" in both cases is exactly opposite to one another (this means it deviates by the same amount but with a different sign). In our case we aimed for a limiting value of $5 \cdot 10^{16}\,\mathrm{W/cm^2}$ as this was the highest efficiency for reflectance in the case of plasma mirror 1. [56, 57]

[4] technical data by Layertec, EKSMA

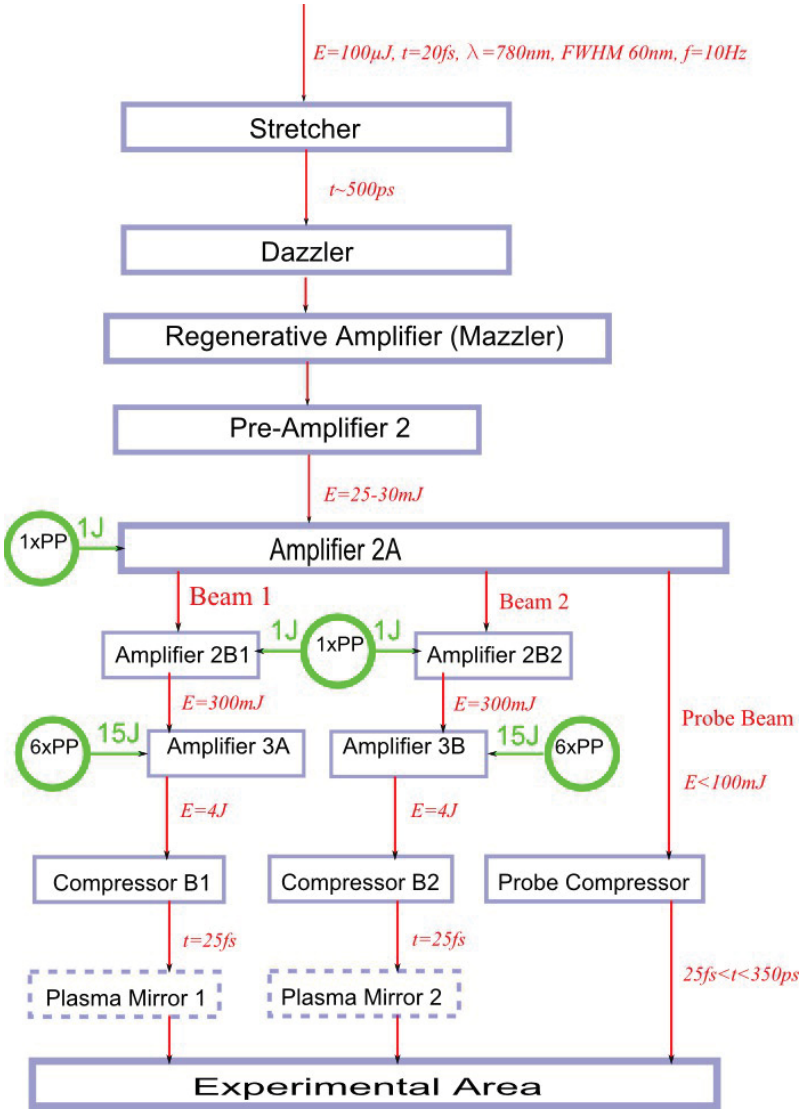


**Figure 3.2** – Schematic of the main amplifiers of the ARCTURUS laser system. Green circles symbolize frequency doubled Nd:YAG pump lasers which pump the Ti:Sa crystals with light at a wavelength of 532 nm. The plasma mirrors, which serve to improve the contrast further, are optional, depending on whether the experiment in question requires more energy or a better contrast.

### 3.4.2 Optical Setup

The starting point for the optical construction is a parabolic mirror with a radius of $r = 6.35\,\text{cm}$ and some geometrical constraints based on dimensions and positions of

the optics (e.g. they have to be big enough to accommodate the beam) and the vessel used. As is usually the case in laser plasma physics the parabolic mirrors used are so-called off-axis parabolas, which means they are cut as a segment from a bigger "parent parabola" and redirect the beam at an angle to the incoming beam. This angle is called the off axis angle $\Theta_{OAP}$. Let us further assume we want to use the same parent parabola as in plasma mirror 1, then these conditions lead us to a parabola with a "parent focal length" of 1524 mm and an off axis angle $\Theta_{OAP} = 9.94\,^{\circ}$. The next step was to determine the precise position of these parabolas, so that the plasma ignition could be triggered optimally.

The intensity of a Gaussian beam at a distance $z$ from the focal plane and a radial distance of $r$ from the optical axis is defined as follows:

$$I(r,z) = \frac{E_p}{\Delta t w(z)^2/2} \cdot \exp\left(-2\frac{r^2}{w(z)^2}\right) \tag{3.1}$$

where $E_p$ is the pulse energy, $\Delta t$ its duration and $w(z)$ the beam radius at the point where the intensity has fallen off to $1/e^2$ of its central peak value. [58]

As we care about the peak intensity, we set $r = 0$. Then, considering that $\frac{(\Delta x_{I0})^2}{w_0^2} = 2ln(2)$ with $\Delta x_{I0}$ as the full width half maximum beam diameter at the focal position, the peak focal intensity $I_0$ results as

$$I_0 = \ln 2 \frac{E_p}{\Delta t \pi (\frac{\Delta x_{I0}}{2})^2} \tag{3.2}$$

Inserting the relation for beam waist development $w(z) = w_0\sqrt{1 + \frac{z^2}{z_R^2}}$ into 3.1 with $z_R = \frac{\pi w_0^2}{\lambda}$ as the Rayleigh length as well as taking into account the beam quality factor $M^2$, the dependence of the peak intensity on position follows:

$$I(z) = I_0 \left(1 + \left(\frac{\lambda z M^2}{\pi w_0^2}\right)^2\right)^{-1} \tag{3.3}$$

Inserting 3.2 in 3.3 yields

$$I(z) = \ln 2 \frac{E_p}{\Delta t \pi (0.589 w_0)^2} \left(1 + \left(\frac{\lambda z M^2}{\pi w_0^2}\right)^2\right)^{-1} \tag{3.4}$$

Rearranging to $z$:

$$z(w_0) = \frac{\pi w_0^2}{\lambda M^2}\sqrt{\frac{\ln 2 E_p}{I(z)\pi(0.589 w_0)^2 \Delta t} - 1} \tag{3.5}$$

In the current case we assume the following values: $E_p = 4\,\mathrm{J}$, $\Delta t = 25\,\mathrm{fs}$, $\lambda = 800\,\mathrm{nm}$, $M^2 = 1$ and $I(z) = 5 \cdot 10^{16}\,\frac{\mathrm{W}}{\mathrm{cm}^2}$ as the intensity for the threshold case. This gives

$$z(w_0) = 3.93\frac{w_0^2}{\mu m}\sqrt{2.034 \cdot 10^5 \left(\frac{w_0}{\mu m}\right)^{-2} - 1} \tag{3.6}$$

Inserting some example values for $w_0$ results as: $z(10\,\mu\mathrm{m}) = 1.77\,\mathrm{cm}$, $z(15\,\mu\mathrm{m}) = 2.66\,\mathrm{cm}$, $z(20\,\mu\mathrm{m}) = 3.54\,\mathrm{cm}$ for the offset of the parabolas from the focused case.

The optical setup thus achieved is displayed in figure 3.3.

### 3.4.3 Experimental Characterization

In order to characterize the plasma mirror built in the context of this thesis, its reflectance was measured by changing the position of the substrate and measuring the reflected energy on a calorimeter placed in front of the second parabola. The measurement was performed by M. Cerchez and R. Prasad. The results are seen in figure 3.4. What can be seen is that close to the focus hardly any energy is reflected, in a distance of around 15 mm a rapid rise sets in which ends in a slowly declining plateau with a maximum at around 20 ps. In order to understand this physically a bit better it was necessary to figure out the dependence of reflectance on intensity. Hence the beam profile was measured at several points along the beam in order to deduce $I(z)$. The result of this measurement is shown in figure 3.5. Unfortunately, no fit for a Gaussian beam converges for these data. This could be due to irregular beam profiles found a few millimeters out of focus (see figures 3.6 and 3.7). They were analyzed by applying radial averaging (i.e. a radial line profile was taken, where for each position the average brightness across all angles was taken), but as there are still inhomogeneities it is possible that the usual definition of "full width half maximum" does not apply here as it presupposes a profile with a Gaussian intensity distribution. For this reason, as an approximation, the minimum beam radius which was measured (18 $\mu$m FWHM, corresponding to $w_0 \approx 15\,\mu\mathrm{m}$ at a position of 1.5 mm from the nominal focus) was used instead to deduce from this an idealized Gaussian beam as far as its longitudinal profile is concerned. Inserting $E_p = 2.23\,\mathrm{J}$, $w_0 = 15\,\mu\mathrm{m}$, $\lambda = 800\,\mathrm{nm}$ and $\Delta t \approx 25\,\mathrm{fs}$ into equation 3.4 the intensity of this beam can be described as follows:

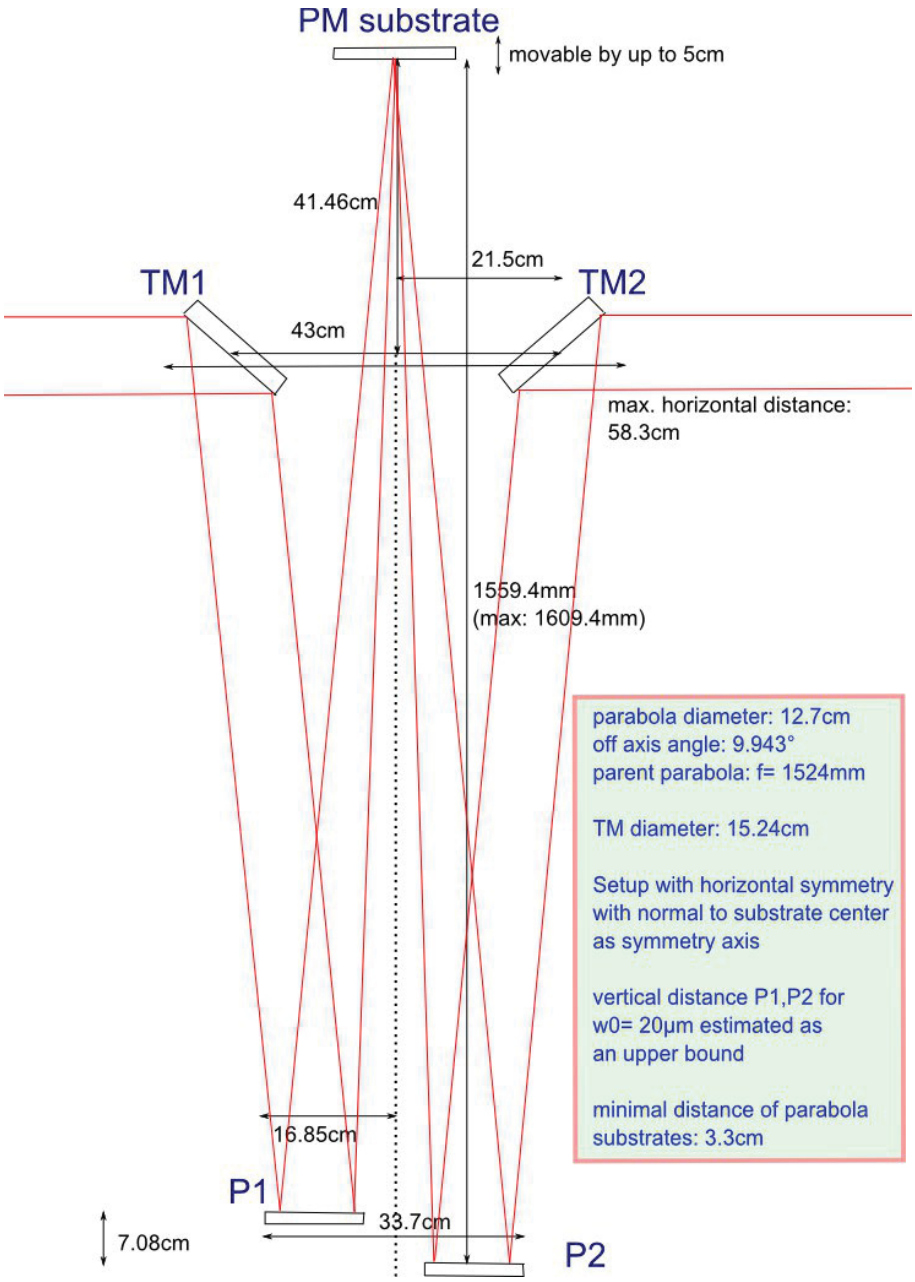


**Figure 3.3** – Optical setup of the plasma mirror. Beam comes in from the left, hits the first turning mirror (TM1), is focused by the first parabola (P1) onto the substrate, reflected by it after ionization, recollimated by parabola 2 (P2) and finally leaves the device after reflection on the second turning mirror (TM2). Ideal conditions for the geometry shown here: pulse energy 4 J, pulse duration (FWHM) 25 fs, focal beam radius: $10 - 20\,\mu$m

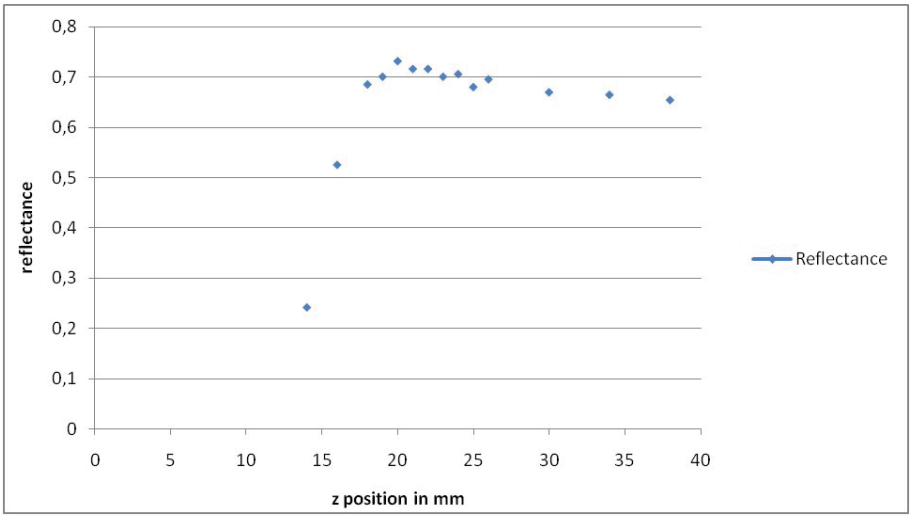


**Figure 3.4** – Reflectance measurement for the characterization of plasma mirror 2. Measurement and graph by M. Cerchez and R. Prasad.

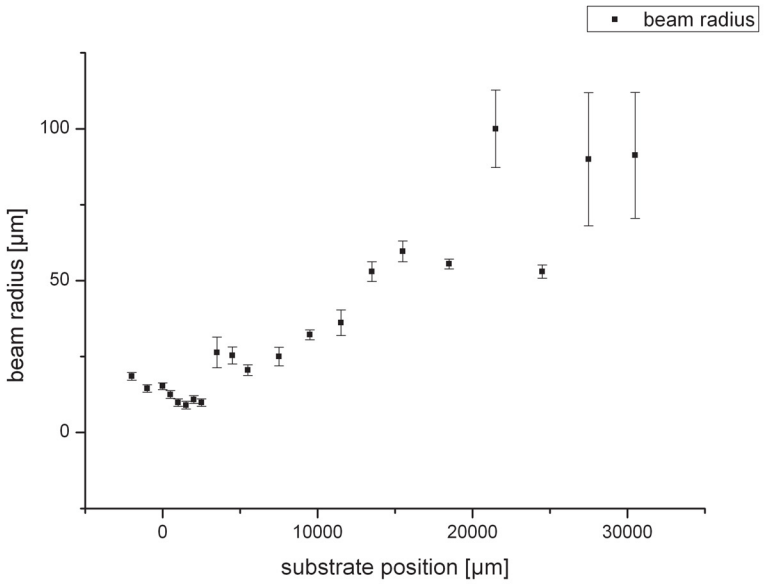


**Figure 3.5** – Position vs beam radius from the z scan of the beam profile.

$$I(z) = \frac{7.92 \cdot 10^{19} \frac{\mathrm{W}}{\mathrm{cm}^2}}{1 + (1.132 \cdot 10^3\,\mathrm{m}^{-1}(z - 1.5 \cdot 10^{-3}\,\mathrm{m}))^2} \tag{3.7}$$

Applying equation 3.7 to the z axis of figure 3.4 yields a graph of intensity vs reflectance

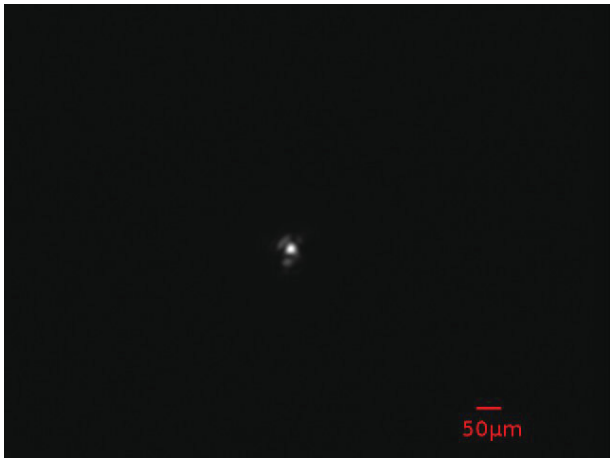


**Figure 3.6** – Beam profile in focal position

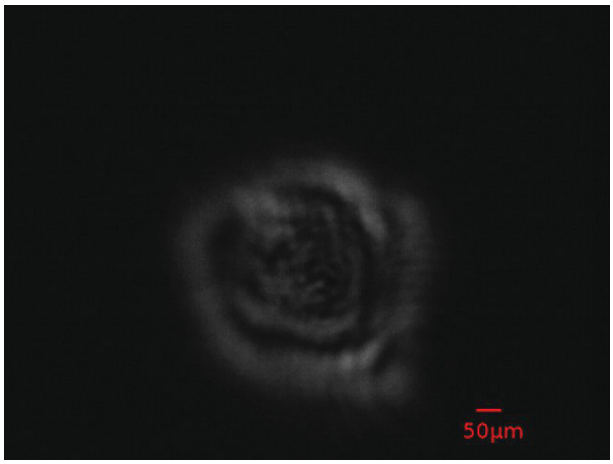


**Figure 3.7** – Beam profile 14 mm from the focal position

as seen in figure 3.8. At first there is a slow increase in reflectance with intensity, which is due to an earlier ignition time in the rising edge of the pulse which causes a larger part of the pulse to be reflected. This increase reaches its peak at an intensity of about $2 \cdot 10^{17}\,\mathrm{W/cm^2}$. After this peak there is a rapid decline in reflectance. The reason is that now the substrate has moved so close to the focal plane that even the prepulse has enough intensity to trigger the plasma ignition and there is no flat surface to reflect the main pulse from, instead there is a bulge which scatters the beam energy, so less of it arrives at the calorimeter.

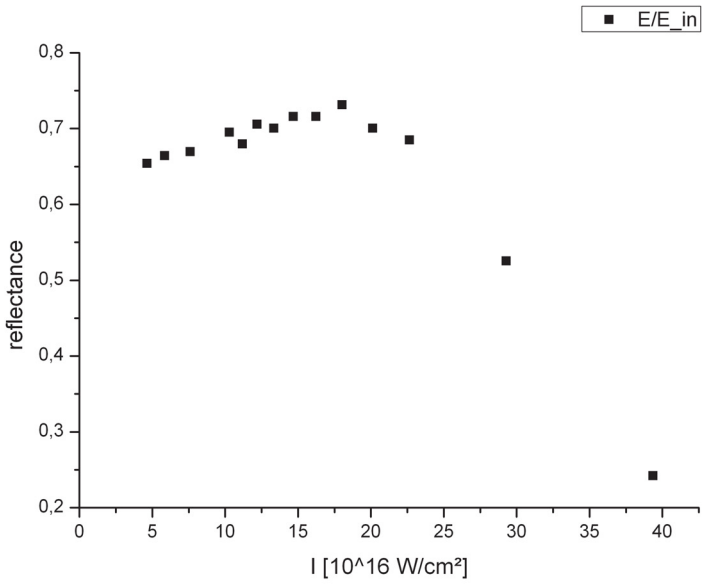


**Figure 3.8** – After translating the positions into the respective intensities the characterizing curve of the plasma mirror looks as in the above figure.

# Chapter 4

# Dose Delivery and Measurement System

## 4.1 Introduction

In this chapter the target and measurement systems for the biological experiments are described as well as the analytical methods employed. In the first part, there is a general overview about the available methods for dosimetry and which methods were chosen by other groups (Belfast, Dresden, Munich, Kyoto) faced with the challenges of performing dosimetry for protons accelerated by laser-driven processes, with an emphasis on the diagnostics used in this work. Next, the design decisions in our case are explained, followed by a detailed description of the dose delivery and measurement system based on these decisions.

## 4.2 Diagnostics and Available Dosimetric Approaches

### 4.2.1 Radiochromic Films

*Radiochromic films* or RCFs are self-developing films which change their optical density in accordance with the dose they are exposed to. This is due to radiation-induced polymerization.[59] With the help of a calibrated scanner it is then possible to determine the dose. Usually they are employed in stacks of several layers. This allows to assign each layer a distinct energy range. There are different types of RCF films, each with

a specific sensitivity in terms of particle energy and fluence. One advantage of this method is that there is immediate qualitative information on the strength of the signal. This was also the method of choice for the Belfast group which used RCF stacks behind the cell port [6]. In our case this was impossible as depending on the type of RCF either the energy range or the fluence at the cell port was too small to be detectable. Instead radiochromic films were used next to the target to assess the proton beam quality prior to the actual measurement or irradiation procedure.

### 4.2.2 CR-39

Polyallyldiglycolcarbonate (*PADC*) or *CR-39* serves as a solid state nuclear track detector. When a particle impinges on the detector it destroys polymer chains. These damages can be made into a detectable track by etching the plates in a caustic solution [60], which in our case was sodium hydroxide with a pH value of 14 at a temperature of 80 °C. Tracks appear because the damaged parts have an etching rate that differs from the undamaged bulk's etching rate. The size of a track depends on the etching time. After washing off the sodium hydroxide, the plate is put into a neutralizing solution of 2 % strong acetic acid, which itself is then washed off. The resulting tracks can be counted by using a microscope. A strength of this method is its accuracy as each track corresponds to a single particle. Another advantage is that electron and X-ray irradiation cause a change in the etching rate, but do not cause tracks like ions do [61, 62]. Additionally, the depth of a track may be used to assess the particle energy. A disadvantage results from the time consuming post-processing procedures such as etching as well as track counting. Additionally, in order to clearly identify tracks it is necessary to avoid overlapping tracks as much as possible, which sets a natural limit to the acceptable fluence. CR-39 detectors were used by the Kyoto group as a primary diagnostic [63] as well as in this work.

### 4.2.3 Imaging Plates

*Imaging Plates* are a detection medium based on luminescence. An active phosphorous layer is situated within a plastic environment[64]. The active medium has the stoichiometric formula $BaF(Br, I) : EU^{2+}$. When hit by a sufficiently energetic particle, an electron is moved from the valence band to the conduction band, before quickly falling down to a metastable state of fluor. Upon irradiation by light with a wavelength of 632.8 nm it moves to a metastable state in the 5d orbital of $Eu^{2+}$ from where it drops

to the 4f orbital of the same ion, emitting light of 400 nm wavelength (see figure 4.1) which can be measured by a scanning device. The process is known as *"photostimulated luminescence"* or PSL. [65]

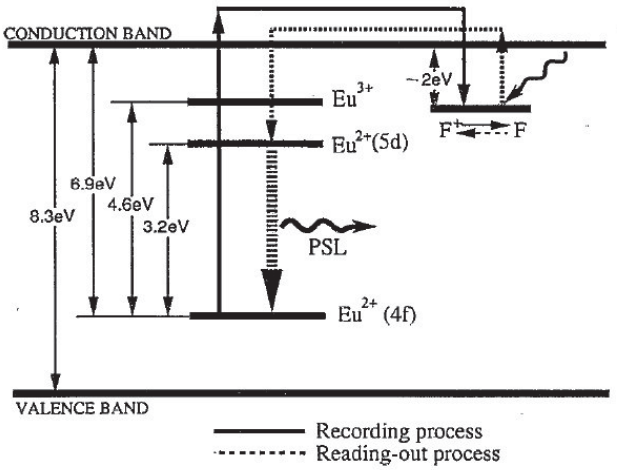


**Figure 4.1** – Energy level scheme of $BaF(Br, I) : EU^{2+}$, the sensitive material within imaging plates [66], image quoted via **Katto, Review of Scientific Instruments, 64, 1993** [65]

Advantages of this medium are its reusability, because it can be deleted, as well as its relatively quick data gathering. Disadvantages are that imaging plates are sensitive to X-ray and electron radiation too and that there is a time dependent loss of signal strength. [67] There is also a need for post-processing depending on the scanner properties.

### 4.2.4 Micro Channel Plate

A *micro channel plate* or MCP is a device with many small channels with a diameter on the order of microns, to which a voltage is applied. When an energetic particle such as an ion hits a channel wall, an electron is set free at some angle. The electron hits the channel wall as well, causing the release of secondary electrons. They constantly gain energy due to the voltage mentioned earlier. Depending on whether it is a multistage MCP, the amplified electron signal either hits a second stage or goes directly onto the phosphorous screen where it evokes the emission of light. [68]

### 4.2.5 Faraday Cup

A *Faraday cup* directly measures the current of the stream of charged particles. If one uses it as a time of flight detector one can also distinguish different energies as they arrive at different times. [69] The Dresden group has used a Faraday cup calibrated against an ionization chamber as one method for dosimetry. [4]The Munich group also used it as a dosimetric method. [5]

### 4.2.6 Ionization Chamber

An *ionization chamber* is a chamber filled with gas which is ionized by the ionizing radiation to be measured. To the sides of this chamber a voltage is applied which attracts charged particles within the gas to the chamber walls. One then measures the current and concludes from this the amount of ionization that took place. [70] Ionization chambers are a recognized standard in medical dosimetry provided they are calibrated against a calorimeter. [71]

### 4.2.7 Scintillators

*Scintillators* are materials that react to the impact of a particle by the emission of light. The Kyoto group employed a plastic scintillator as a time of flight spectrometer, by amplifying and resolving the scintillator brightness in time. [63, 72] The Munich group used a CsI scintillator to control the homogeneity of dose distribution [5].

## 4.3 Design Decisions

There are two principle design approaches possible in irradiating cells with protons: Either a quadrupole magnet is used for (de)focusing of the particles (see e.g. [73]) or magnets are used to disperse the particles according to energy, e.g. by the Kyoto group [63]. In our case we were inspired by the latter approach. Its advantage is that a separation according to energies allows for experiments with a chosen and variable energy range.

As for the dosimetric method, the standard method is to use an ionization chamber [71], but given that the proton energies were low and the experiments had to take place in a vacuum with pressure on the order of $10^{-2}$ Pa, we chose not to use this method.

Instead we made use of the energy dispersion inherent in the setup, which allows to get spectral information from the spatial proton distribution. Using this as a starting point, it seemed logical to employ a diagnostic that is optimally suited to give a spatially resolved map of proton impacts, i.e. CR39. Due to the time consuming nature of the analysis of the plastics, in addition IPs were used as well in order to achieve quicker dose information while still capturing the spatial proton distribution.

## 4.4 Description of System

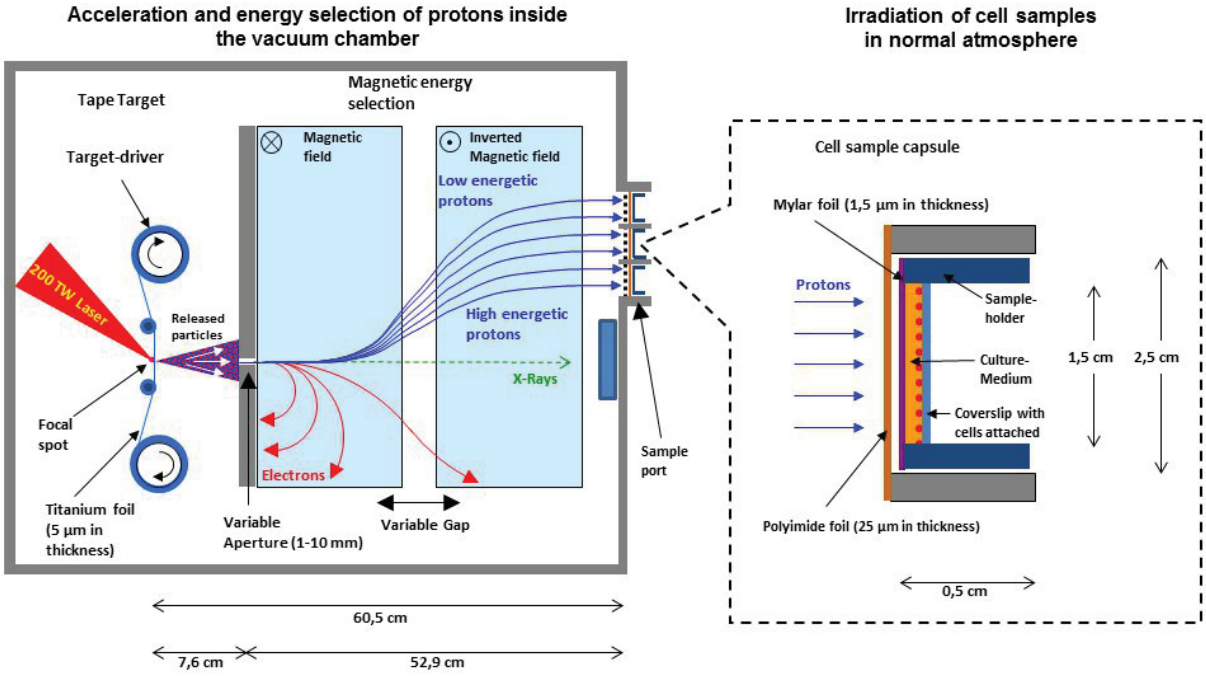


**Figure 4.2** – Irradiation system for LAP. **Raschke et al, Scientific Reports, 85, 2016** [7]

As described in chapter 2 the TNSA process accelerates protons (as well as other ions) to energies in the MeV range and they leave the target perpendicular to its rear side. These particles then enter our actual setup: First they enter the energy selection which consists of two yokes oriented opposite to each other (figure 4.4) which, by way of dispersion, separate the protons according to energy. These protons then hit a number of layers before interacting with the cells. In the following subsection these parts and their function are described in more detail.

### 4.4.1 Tape Target

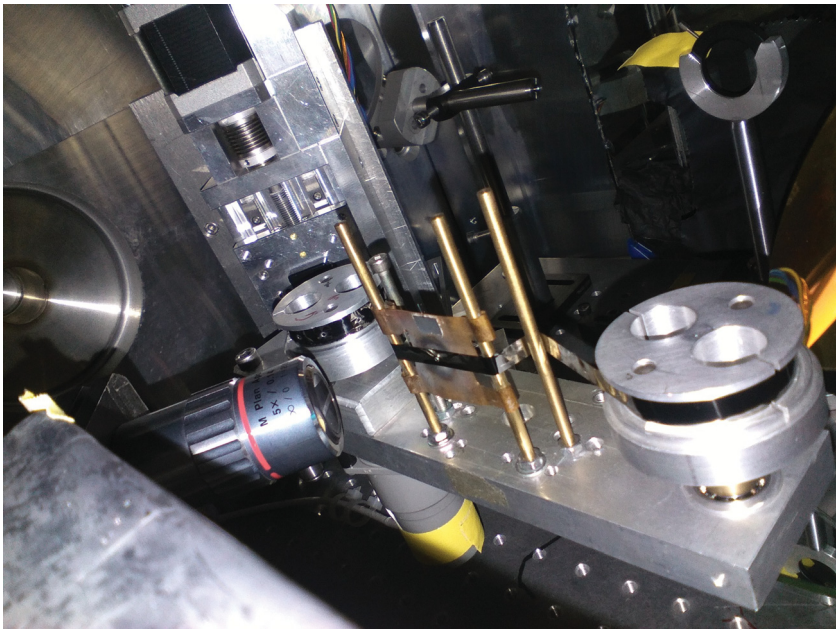

**Figure 4.3** – Tape driver. Two coils are visible, the right one providing fresh target material, the left one collecting shot material. The driving motor is situated below the collecting coil. The tape is protected by two copper shields. On top of the upper copper shield there is an alignment wire. A microscope objective is used for focus diagnostics. Motorized translation stages allow for a precise target alignment on the order of microns.

The tape driver or tape target continuously supplies fresh target material via a motorized reel construction (see figure 4.3). The entire construction rests on a 3D translation stage, which allows for precise alignment in order to place the target into the focus, so that an optimal interaction can be achieved. In the upper part of the construction, there are two coils. One is the supply coil with the remaining target material, the other is the driving coil, whose rotation is driven by a motor. The motor's rotation speed can be varied by applying different voltages to the motor. At a typical operating voltage of 1.7 V, the angular speed is $\omega = 10\,^{\circ}\mathrm{s}^{-1} \pm 0.2\,^{\circ}\mathrm{s}^{-1}$. Besides the coils there are also metal bars in the upper area of the tape driver, which allow for the tape to be mechanically tense. Finally, there are two protective layers of copper which shield the target material from laser radiation (burn lines caused by diffraction patterns from the parabolas due to how they were polished during their production process[1]) except for the position of

[1] oral communication by Prof. Willi

focus. This was necessary as otherwise the tape might get cut, especially in the case of two beam experiments and overlapping burn lines.

As target material we used 5 micrometer thick titanium foil with one item being 10 m long. This allows for at least 700 shots and up to 5000 shots before having to put fresh target material into the chamber. These numbers result from the width of the unusable area of debris resulting from a shot, which is estimated to be 2 mm for the upper estimate on one hand and from the uncertainty of movement due to a single turning on and off cycle of the voltage which was estimated from experience as 14 mm (for the lower estimate). This is the main advantage of a tape driver as a target versus a single foil target holder. Titanium was chosen as a material as it makes the tape mechanically stable and sufficiently thin to be of good use in a TNSA interaction [9].

### 4.4.2 Magnets for Energy Selection

The magnets (see figure 4.4) serve as an energy selection. There are two 10 cm$x$10 cm neodym magnets fixed within a steel yoke construction with a distance between the two of $\approx$ 1 cm for each of the magnetic yokes. The second yoke serves to compensate the change in output angle introduced by the first one, so that straight entrance of a particle means straight exit as well. The gap between the two yoke constructions is variable so as to control the dispersion, as a larger gap means a larger dispersion due to a longer range of free flight and implicitly a larger effect of the angular difference between particles of different energies.

The magnetic yokes have been designed, constructed and measured by Philipp Weiß, who also built the experimental chamber, in which we placed our setup. The magnetic field strength of one of them is shown in figure 4.5. It was also confirmed in a calibration measurement that the magnets deflect particles as predicted.[10]

For our experiments we chose a gap of 2 cm, leading to a dispersion function displayed in figure 4.6.

### 4.4.3 Cell Ports and Layers

The layers that the protons have to pass after leaving the yokes and entering the cell port system (see figure 4.7) are as follows:

1. 10 $\mu$m of aluminium in order to block the laser light.

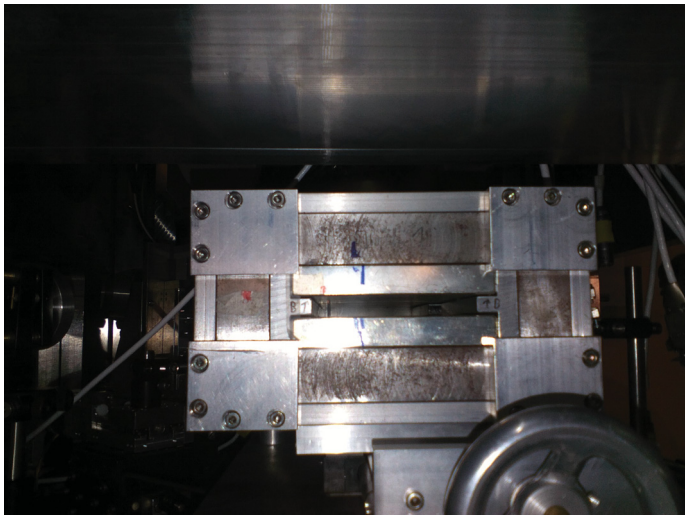

**Figure 4.4** – View on the exit of the double yoke construction. Two magnetic plates are placed in a distance of $\approx 1\,\mathrm{cm}$ of each other in each of two steel yokes respectively. The field between the plates is around $B = 850\,\mathrm{mT}$. In the background, one can see the aperture slit through which the particles enter the energy dispersion. In the lower front part of the image, one can see the crank used to change the gap distance between the yokes.

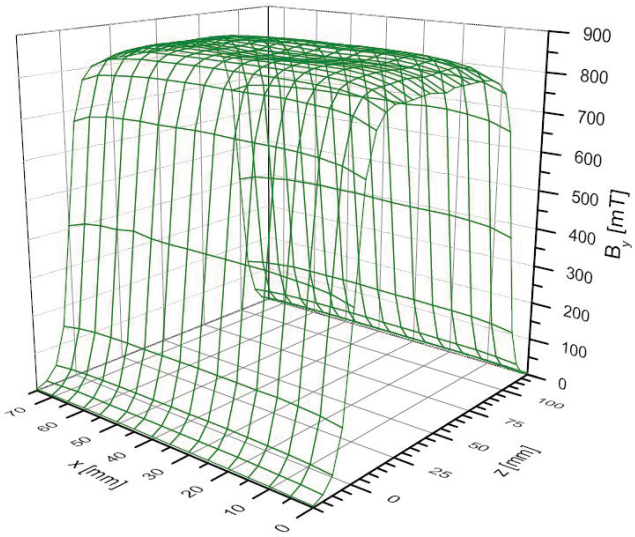


**Figure 4.5** – Magnetic field strength within the first yoke.[10] The second one is similar. **Weiß, Heinrich Heine Universität Düsseldorf, 2011** [10]

2. $25\,\mu\mathrm{m}$ of kapton foil for isolating the vacuum

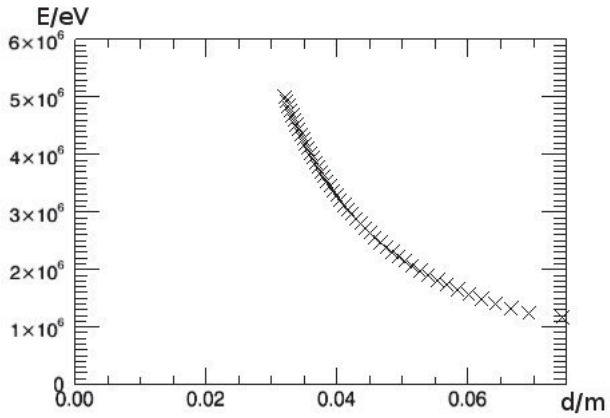


**Figure 4.6** – Dispersion of the double yoke (gap 2 cm) in port area. This graph was created by the particle tracer program (see section 4.6.1). The x-axis shows the distance from the zero point, i.e. the point a non-deflected particle would hit whereas the y-axis indicates the proton energy.

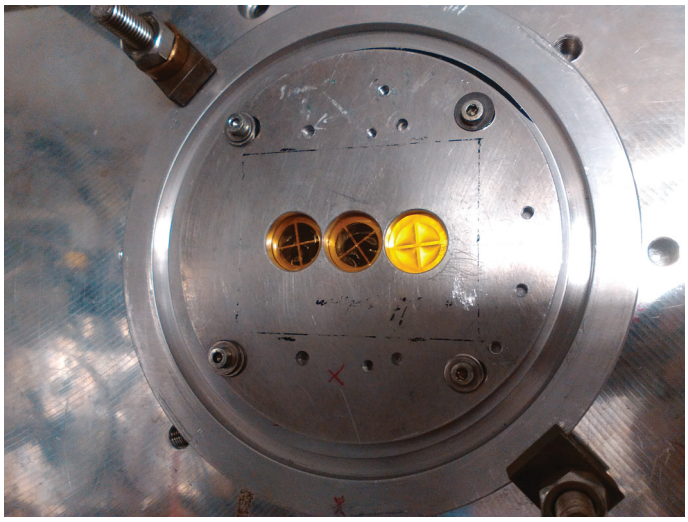

**Figure 4.7** – Outside view of the cell port flange. There are three ports, each with a different energy range arriving. Each port isolates the vacuum inside the chamber from the outside air by means of 25 $\mu$m polyimide foil supported by a steel grid. In the displayed situation the rightmost port was in use and aluminium foil was added. The inner diameter of the ports is 25 mm, the usable diameter of the cell holders 15 mm.

3. Next they encounter the mylar foil (1.5 $\mu$m thick), which is on one end of the cell holder; this cell holder also contains cell medium (15 $\mu$m).

4. Finally there is a 5 $\mu$m thick monolayer of A549 cancer cells, which are attached to a cover slide.

## 4.5 Energy Transfer from Protons to Cells

### 4.5.1 Stopping Power, Linear Energy Transfer and Bragg Peak

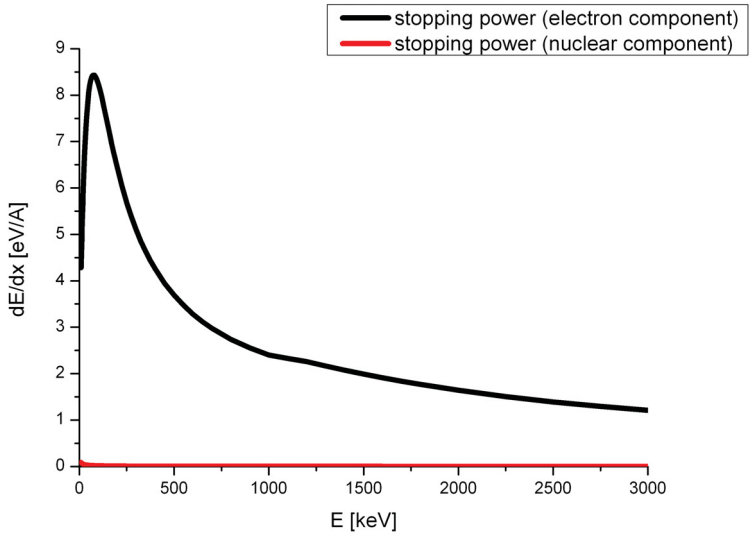


**Figure 4.8** – Stopping power of water for protons. It is evident that the stopping power is dominated by the effect of the electrons (black line), while the stopping effect caused by the target's nuclei (red line) is negligible.

Protons as opposed to x-ray radiation deposit their energy to a large extent localized within the so-called *Bragg Peak*. [74] This comes about as follows: The *stopping power* of ions in a material describes the energy transferred per crossed distance depending on the energy of the particle. It is given as:

$$S(E) = -\frac{dE}{dx}(E)$$

(see figure 4.8) With this curve, it is possible to predict the deposition of energy within the material depending on position, i.e. the distribution in space of the *linear energy*

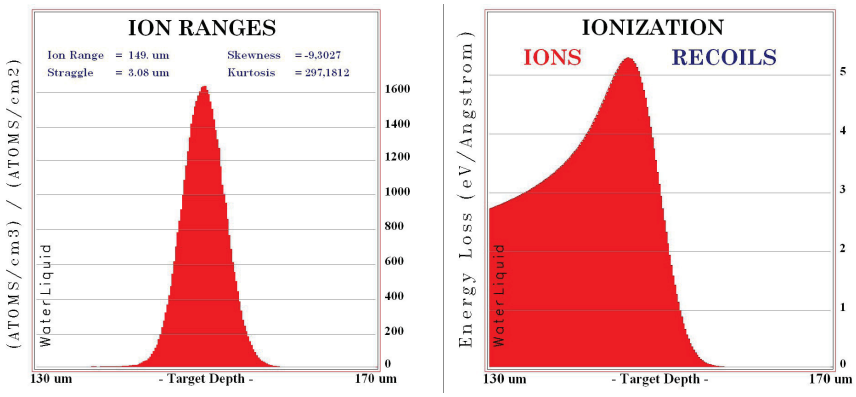


**Figure 4.9** – This figure shows both the distribution of simulated ions in SRIM (simulation run with $\approx 10^5$ 3 MeV protons in water) as well as the average linear energy transfer of a 3 MeV proton depending on position within water in the region near the Bragg peak. Compared to figure 4.8 the maximum energy loss is lowered due to statistical fluctuations of the particle trajectories within the medium. Nevertheless, a qualitatively similar, inverted shape to the stopping power curve is apparent.

*transfer*, which is defined as:

$$LET(x) = \frac{dE}{dx}(x)$$

In practice the curve is somewhat 'washed out' as there are stochastic effects due to different particles experiencing different sequences of scattering processes (see figure 4.9). The stopping power of compounds (as is the case in our setup) can in general be calculated as a linear superposition of the stopping power of their component elements, which is proportional to the square root of their atomic weights. This principle is known as *Bragg's rule* and the accuracy stopping predictions using this rule is better than 20 %[74, 75]. The remaining inaccuracy results from differences in the electron structures that are specific to each compound. To take into account effects of molecular bonds on stopping power, an approximation (later named *cores-and-bonds approximation* (CAB)) was introduced by Both et al [76], which distinguishes the contribution to the stopping power by atomic 'cores' from that originating from molecular 'bonds'.

### 4.5.2 Ionization and Cell Damage Events

If one integrates this *Bragg curve* $LET(x)$ along a region of interest, one can determine the deposited energy along this region. This is relevant, as this energy causes biological effects of interest. Secondary fast electrons, so called *delta rays* are responsible

for causing various types of cell damage, more so than the protons themselves. [77] These damages include base damages, single strand breaks as well as double strand breaks in the DNA structure [78]. In addition, there is also indirect damage due to radiation-induced water radicals which can chemically interact with the DNA and other macromolecules in the cellular environment, causing additional cell damage. Among the possible damages, double strand breaks (DSBs) stand out as they have the strongest effect on biologically relevant end points such as cell death. Another mechanism of DNA damage is the so-called *bystander effect*, in which cells that were not themselves traversed by ionizing particles, but which are neighbouring cells that were, also exhibit biological damage [78].

Actual cell death can occur in several fashions: *Mitotic death* and *apoptotic death* are the principle modes for irradiated cells. The former describes cells that are unable to divide properly due to radiation damage, whereas the latter describes programmed cell-death, i.e. the cell kills itself. Mitotic death is the dominant form of the two in radiation contexts. The effect of radiation on cells also depends on the cell type as well as on its stage within the cell cycle and its level of oxygenation. For example, irradiated tumor cells that lack in oxygen may not die as opposed to oxygenated cells receiving the same treatment. [78]

The effect of direct damages by delta rays appears to strongly depend on the precise path of the ionization track caused by secondary electrons, relative to the position of the DNA strand in question. There are indications that clustering of damages has a more potent effect than spread out damages do. [79] This is another reason why spatial and temporally inhomogeneous radiation might be more damaging to cell tissue than homogeneous and continuous radiation. Spatial clustering could also lead to a potential shift in the balance of direct and indirect damage, as on the one hand it can cause more severe direct damage, but on the other hand fewer water radicals may be created. We were able to observe such a shift, but the cause is still subject to debate [7].

There are dose rate effects documented in literature [78], with a higher dose rate usually contributing to reduced cell survival. The reason is that repair mechanisms such as repair of double strand breaks can take place during irradiation if it takes longer [78]. This dependence was found to be strongest in the dose rate range of 0.01 Gy/min..1 Gy/min, with less of a dependence below or above this interval. In our case the fractionation method (one shot approximately each 3 s) results in an average dose rate of 0.66 Gy/min, which lies well within this range. When investigating dose rate effects and interpreting results, this has therefore to be taken into account in addition to possible effects of

the exceedingly high 'instantaneous dose rate' during a single proton pulse. The latter dose rate is 9 orders of magnitude larger than the dose rate range mentioned and its effects, if any, are unknown. There might plausibly be some if they were to interfere with mechanisms on the pico- to nanosecond timescale.

There can also occur an *inverse dose rate effect* where the irradiation process takes so long that the cells move into a more radiosensitive stage of their cell cycle, in which case a lower dose rate can actually lead to an increase in biologic damage. As this can happen in a dose rate range on the order of 1 Gy/h [78] and as the cells in our experiments were not synchronized[2], this is very likely of no relevance to our experiments.

## 4.6 Description of Dosimetric Method

The aim of dosimetry in our case is to determine the energy dose deposited in the irradiated tissue. The energy dose is defined as $D = E/m$, with $E$ as the deposited energy within the mass $m$. The mass of the monolayer can be determined by $m = V \cdot \rho$, where $\rho$ is the density of the cell, which is assumed to be the density of water and $V$ its volume. The volume was determined by measuring the irradiated area as well as by information on the thickness of the cell nucleus of the adherent cells as 5 $\mu$m [3]. We also measured the distance from the mylar foil to the centre of the cell layer by moving the focal plane of a microscope to both positions and measuring the vertical movement with a micrometer screw, so as to determine the overall thickness including the cell medium. The remaining task was to determine the deposited energy. It was decided to approach this problem in two steps: First, to determine the proton number distribution within the irradiated area and second to determine the energy deposited by an average proton at a given position.

The first step is performed by evaluation of irradiated dosimetric media and is described in the experimental chapter. The second step is performed via simulations based on the magnetic field and the geometry of the setup and is described in this section. Once both steps have been achieved, it becomes straightforward to determine a dose with a chosen spatial resolution for a chosen target area: Multiplying the proton number in this area by the average deposited proton energy yields the deposited overall energy, which in turn yields the deposited dose once this is divided by the irradiated mass. The deposited dose on the cell layer in the entire port is then calculated by averaging over

[2] oral communication Dr. Raschke

[3] oral communication Dr. Raschke, oral communication Dr. Giesen

all the local doses.

### 4.6.1 Particle Tracer

In order to determine which energies end up where on the cell port, a particle tracer program originally written by Philipp Weiß was modified. The original program used a fifth order Runge-Kutta algorithm to trace charged particles entering into a magnetic field at a fixed angle in order to determine the dispersion relation. [10] This algorithm is closely related to Euler's method of approaching problems posed by differential equation via a discretizing approach [80]. The modifications included taking into account different horizontal and vertical angles of entry to account for the divergence due to the finite width of the entrance slit. As these different angles also imply an energy range at a given position instead of just a single energy, the program was also modified to assess the energy range for each position on the cell port in a 16x16 grid of 1mm steps. The resulting energy map is presented in figure 4.11. The commented program is contained in appendix 8.1.

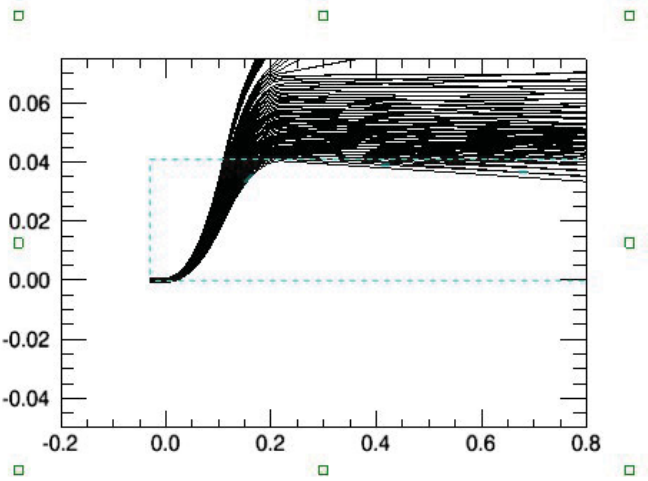


**Figure 4.10** – Simulated trajectories for different energies and angles are overlayed in this image. Each solid line represents a different trajectory. The rectangle made of small, blue, dashed lines represents the area in which the current particle moves, whose trajectory is indicated by slightly longer, thicker, blue line segments. x- and y-axis represent position in meters. The magnetic double yoke is located between $x = 0\,\mathrm{m}$ and $x = 0.22\,\mathrm{m}$

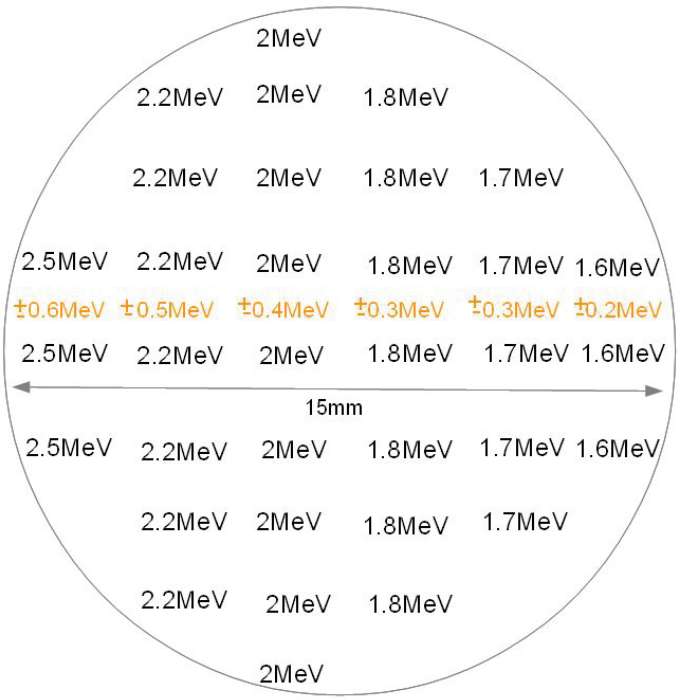


**Figure 4.11** – Map of proton energy ranges depending on position. To improve visual clarity, the original 16x16 map has been reduced to a map containing a horizontal grid of only 6 points along the dispersion axis for this image. The range given is the overall energy range arriving at the area covered by each grid point. The effect of different vertical angles was so small as not to be noticeable.

### 4.6.2 Method to Determine Deposited Energy per Proton

For each proton energy, with which particles impact the cell port, it is necessary to determine the deposited energy per proton within the cell layer. In each case the Bragg peak is located at a different position and depending on the energy this position may be located in front of, within or behind the cell layer of interest. To investigate this in detail for our given settings of layers and energies, the software package "The stopping and range of ions in matter" (SRIM) was employed. SRIM uses the Monte Carlo method to calculate the stopping of ions in matter. It states its accuracy in prediction of stopping as better than 2 % and employs the CAB approach (see section 4.5.1) [75]. The results of these simulations are shown in figure 4.12. As for each initial energy a different energy is deposited within the cell layer, in order to determine the deposited energy for the average impinging proton at a given position, one has to average over

the initial energy range for a given position. This results in a final energy map with position dependent information on the deposed energy per proton at a given position (see figure 4.13)). A similar approach, based on the one described in this work was later used by Ingenbleek [81].

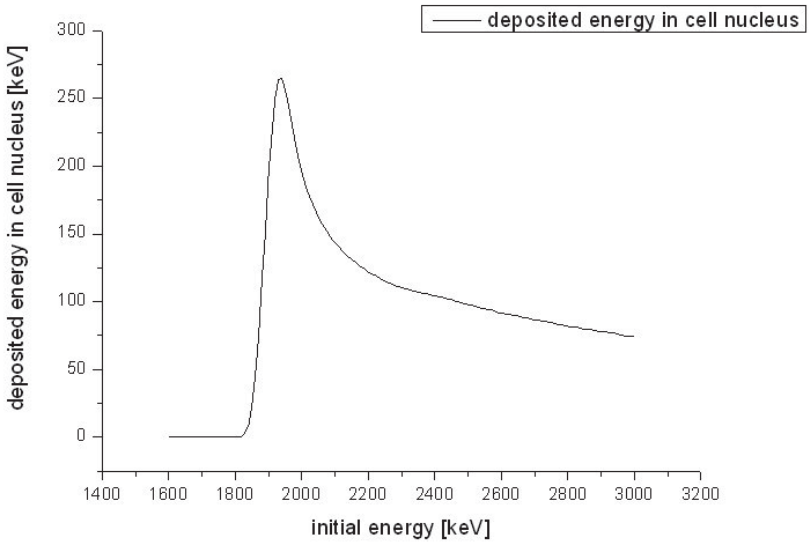


**Figure 4.12** – Energy deposition within the 5 $\mu$m thick cell layer depending on initial proton energy. The adherent cell layer mostly consists of the cell nucleus with only a thin layer of cytoplasm surrounding it (oral communication Dr. Giesen). Below 1790 keV no energy is deposited within the layer. At an initial energy of 1940 keV the maximum energy deposition is achieved 265 keV as shown in the graph. Results were obtained via SRIM simulations.

This is of course an approximation as it supposes no significant change in the proton number density over the local initial energy range covered by the grid point in question. The inaccuracy introduced that way is biggest near the Bragg peak while far from it a spectral deviation from an equal distribution is of little consequence because the deposited energy curve does not depend as strongly on the initial energy. This effect may be reduced by decreasing the slit size, which reduces the energy range at a given grid point. An increase in the number of grid points can also contribute to mitigating this issue, but only up to a point as for any given position there is a finite energy interval arriving, regardless of resolution. If one wanted to avoid the assumption of a local equal distribution entirely and be more precise, one would need to assume a spectrum as a weighing function, which itself unfortunately is subject to shot-to-shot fluctuations.

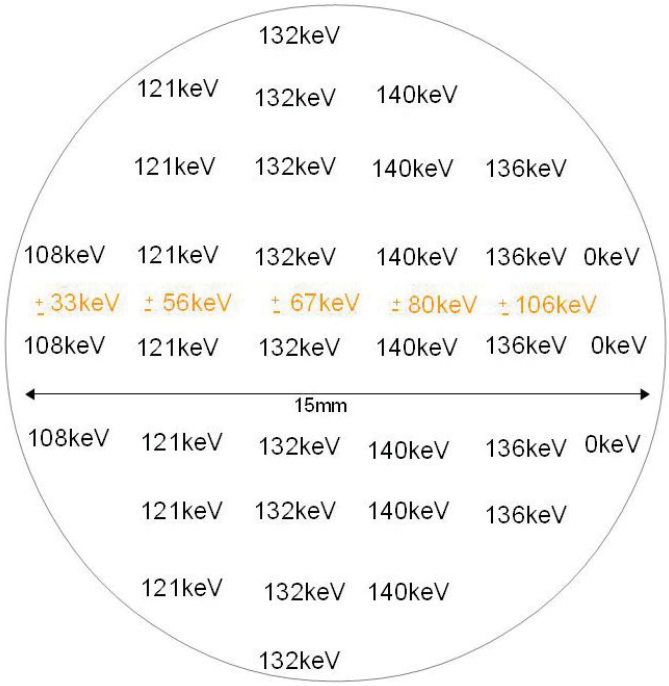


**Figure 4.13** – Map of deposited energy per proton depending on position. To improve visual clarity, the original 16x16 map has been reduced to a map containing a horizontal grid of only 6 points along the dispersion axis for this image. The range given is the standard deviation of final deposited energy per proton in the sense that 68.3 % of initial energies arriving at the area covered by this grid point in the simulation deposit energy within this interval. The effect of different vertical angles was so small as not to be noticeable.

However, to some extent the inaccuracies introduced by this assumption are accounted for by the rather large standard deviation resulting from it (see figure 4.13). A weighted map would move the averaged deposited energy value somewhat but would on the other hand reduce the standard deviation as its variance has to be smaller than an equal distribution, which is the widest distribution imaginable.

The inaccuracy caused by this assumption is difficult to quantify as it depends on the spectrum used as a weighing function. One approach would be to take the standard deviation as a measure. It is readily apparent that it is largest near the Bragg peak ($\pm 78\,\%$) and becomes smaller as one moves to higher initial energies ($\pm 31\,\%$) even though the initial energy range is wider there due to weaker dispersion.

[75, 82]

# Chapter 5

# Dosimetry and Biological Experiments

## 5.1 Introduction

This chapter describes experimental results achieved with the application of the dosimetric method for laser-accelerated protons, which was detailed in the previous chapter. It contains a description of dosimetric measurements with CR39 as well as imaging plates and concludes with a summary of biological results for which the dosimetric method was used.

## 5.2 Parameters of Setup

The basic setup has already been described in chapter 4 (see Fig. 4.2). As parameters we had a distance of 7.6 cm from the interaction point to the entrance of the yoke and a gap size of 2 cm in between the two magnetic yokes.

## 5.3 Dosimetry with CR 39

A CR39 plastic was placed behind the cell port, instead of the cell holder. This means that the only layers the protons would pass were the aluminium and the polyimide foil. After irradiation, the plastic was etched for 15 minutes in NaOH solution and after neutralizing and rinsing was investigated with a microscope. Tracks were counted by

hand on a set of sampled pictures. The sampling occurred in a 1 mm by 1 mm grid. After obtaining the spatial number distribution this was weighted by the averaged deposited energy per proton within the cell and from this a local dose could be derived for each position after dividing the overall deposited energy by the mass of the irradiated volume.

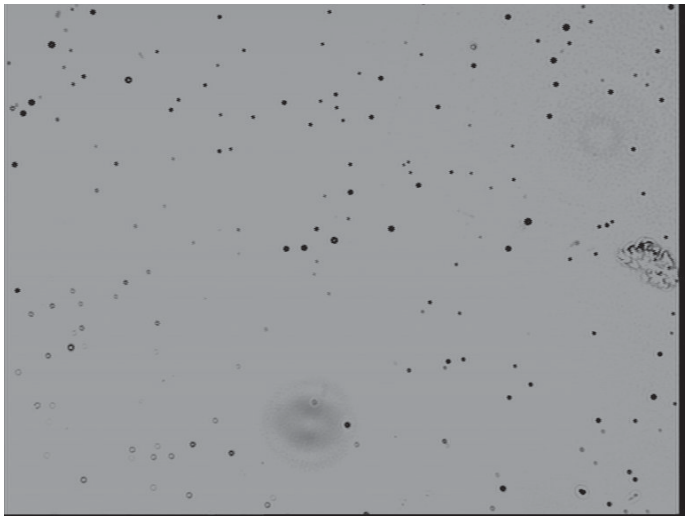

**Figure 5.1** – A typical microscope image (with a magnification of 100) of a CR plastic. This image shows 144 tracks in an area of 127 $\mu$m x 95 $\mu$m. The larger structures on the right and in the lower part are dirt on the CR and damages of the lens respectively.

As an example for a local dose calculation, consider the situation near the centre of the cell port: Within the sampling area located half a millimeter from the centre in both horizontal and vertical direction, 148 tracks were counted. The initial energy of protons arriving in this area ranges from 1.6 MeV to 2.3 MeV. This translates into a range of the deposited proton energies from 0 keV (at 1780 keV and below) to 265 keV (at 1940 keV). The deposited energy per proton is then 136 keV $\pm$ 71 keV. From this follows an overall deposited energy of 20.1 MeV within the sampled area of 12065 $\mu$m$^2$. The areal density of deposited energy is 1.67 $\frac{\text{keV}}{\mu\text{m}^2}$. Taking into account the layer thickness of 5 $\mu$m and the density of the cell layer, which is approximately that of water, $\rho = 1000\,\frac{\text{kg}}{\text{m}^3}$, the result for the local dose in this area is $D_{local} = 53\,\text{mGy} \pm 29\,\text{mGy}$

Next the average was taken over these local doses across the entire cell port (see figures 5.4 and 5.5) to obtain the dose associated with this shot. It was determined as

$$D_{port} = 33\,\text{mGy} \pm 21\,\text{mGy}$$

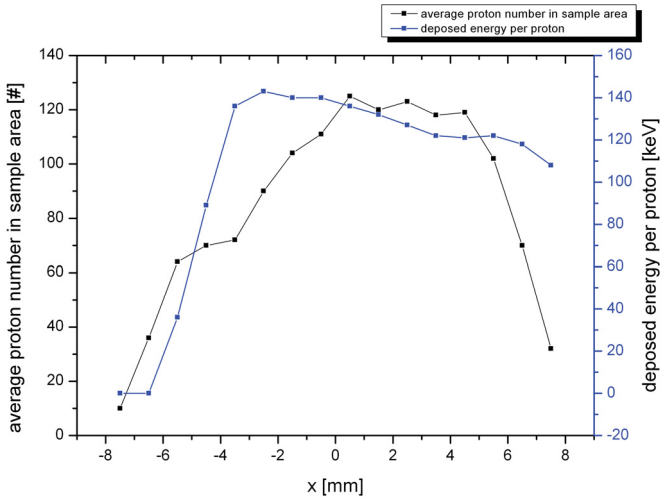


**Figure 5.2** – Black points indicate the average measured proton number within a sample area of 127 $\mu$m x 95 $\mu$m, depending on the position along the dispersion axis. The deposited energy per proton is indicated by the blue dots. The zero position of x corresponds to the centre of the cell port. Lines are meant to guide the eye.

Figure 5.2 shows the average proton numbers (black curve) as well as the deposited energy within the cell layer (blue curve) depending on position within the cell port. Energy is increasing with x. The deposited energy per proton rises quickly, as the proton energy becomes sufficiently high to pass the foils and reach the cell layer. Simultaneously the proton number arriving on the CR 39 rises for the same reason. After this there is a decline in the deposited energy as fewer particles from near the Bragg peak contribute to the averaging process. The fall off in particle numbers at high x values is probably due to the fall off in proton number typical of a TNSA spectrum. What may seem a bit surprising at first is the slow increase in proton number even after passing the energy edge, which is not expected of a TNSA like spectrum. However, several factors have to be considered: For lower energies the spectrometer resolution is smaller, so the number density is expected to be lower. In addition, due to divergence caused by the slit size the edge is washed out and this means there are protons arriving that are not counted and that do not deposit energy, but which still are part of the initial spectrum arriving at the cell port.

If one reconstructs the spectrum from this measurement of proton numbers for our sample shot, TNSA features also become apparent, see Fig. 5.3. This reconstruction was made by assigning weights to each energy within the respective energy ranges for

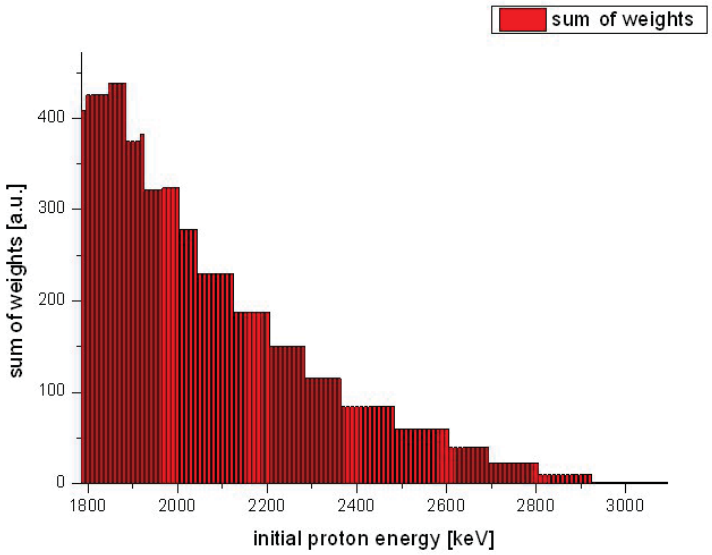


**Figure 5.3** – Taking into account the energy range of the protons arriving at each position, it is possible to make an approximation for the initial proton spectrum which impinges on the cell port. The lower cutoff energy in this graph signifies the minimum energy (1790 keV) which passes the layers of the cell port in order to deposit energy in the cells.

all the positions at the cell port. This approach has an inherent limitation as it starts from the assumption of equal number density within each energy range (see section 4.6.2 for a detailed discussion) and so this reconstructed spectrum should be treated as an approximation.

As this is the dose for a single shot only and thus cannot take into account shot-to-shot fluctuations we also used imaging plates inbetween each shot series on cells as another kind of dosimetric medium.

## 5.4 Dosimetry with Imaging Plates

While in the case of CR39 the counting process is relatively straightforward as each particle corresponds to one track, in the case of imaging plates it is a bit more complicated. This section is dedicated to describing the process by which this becomes possible. For this purpose a program was written in the language IDL, whose function is described in this section and contained in appendix 8.2. The program is loosely based on a program by A. Mick[83] which retrieved a spectrum of a grey value sum over pixel

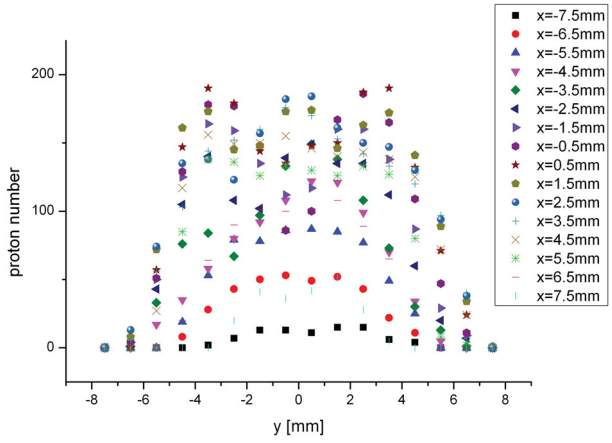


**Figure 5.4** – Number of tracks depending on position in the 1 mm by 1 mm sampling grid. Each of them represents the counted number of tracks within the sample area on the evaluated CR39 at the given position. y is the vertical position on the sampling grid, x the horizontal one.

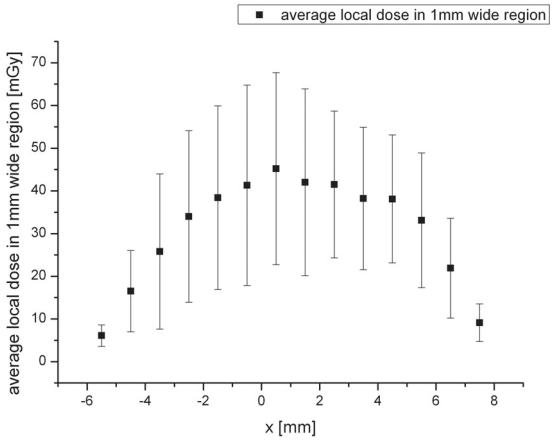


**Figure 5.5** – Average deposited dose within the analyzed area depending on the position along the dispersion axis.

value for the area of the cell port from the scanned Imaging Plate. This is also the first step for the new program.

The process consists of several steps as the scanned results contain the grey values only and what is desired is the proton density for each position. In a first step the program converts the grey values to PSL intensity. The converting function differs from scanner to scanner and often has a logarithmic dependence (see e.g. [84]) due to a

**Figure 5.6** – A scanned image of an IP. The bright area in the center is the irradiated cell port, while the x-like structure is the proton shadow of the supporting grid. Lower proton energies are in direction of the bottom part of the port in this picture which corresponds to the right direction in the cell port picture of figure 4.7.

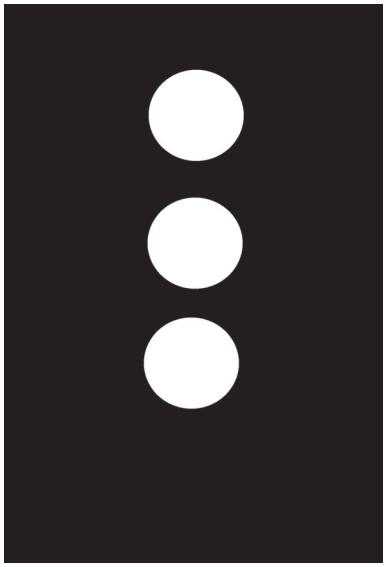

**Figure 5.7** – A mask is created marking the position of the three ports, which can be seen due to the X-ray background if one enhances the original image. This mask is used as a guide for the program to know which parts to analyze.

logarithmic conversion within the scanner in between the photo-multiplying tube and the amplifier [85]. In our case the scanner Bio Step CR35 Bio was used, which has a linear dependence between grey value and PSL:

$$p(g) = 0.0004 \cdot g - 0.0024 \tag{5.1}$$

where g is the grey value of a pixel and p the corresponding PSL value. [86] Proportionality is a sufficient condition to give a statement on shot to shot fluctuation even without an absolute dose value, hence it would be a desirable property of the equation. However, due to the offset, eq. 5.1 does not actually describe a proportional relation. The assumption of proportionality is nevertheless justified as an approximation: For the shot with the smallest signal, where the offset has the greatest effect on the PSL value, there is an average grey value of 242 in the cell port and the systematic error introduced is 2.5 %. For the other 29 shots it is less than 1 %. These values are entirely negligible when compared to the uncertainty introduced by the deposited energy per proton, which is an order of magnitude larger (see figure 4.13). For this reason the grey value could be treated as the PSL value in a first step and only in the end the PSL calibration factor had to be taken into account in order to arrive at the actual dose.

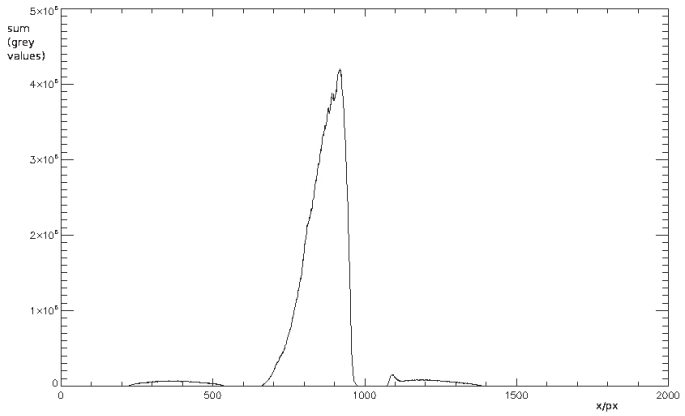


**Figure 5.8** – This image contains the distribution of grey values along the dispersion axis, i.e. the vertical axis in figure 5.6. The x axis shows the pixel number, while the y axis shows the sum of grey values along a line perpendicular to the dispersion axis within the port. Maximum values are at $\approx 4 \cdot 10^6$. To the left and the right of the main signal, two weaker signals in the neighbouring ports are apparent. This is mostly due to the X-ray background, except for a small peak in the right port, which is probably due to very low energy protons barely making it through the layers to be registered on the IP.

As a next step one needs to convert the PSL intensity to the number of protons. While

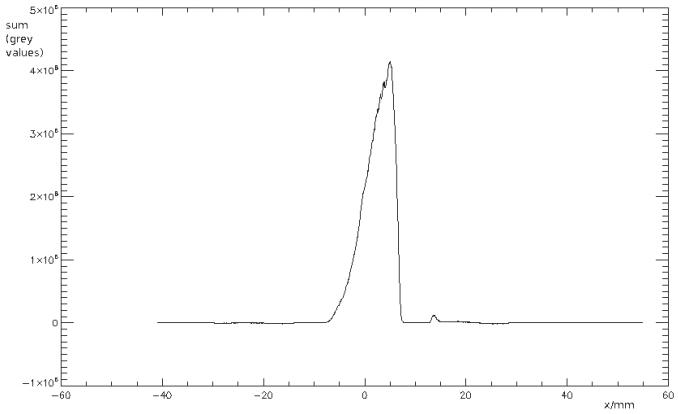


**Figure 5.9** – As a next step, the background was subtracted and the pixel positions changed to distances (in mm), while the zero point was moved to the center of the cell port.

this can reasonably be assumed to be linear in number for each proton energy until saturation sets in (each particle has the same effect), it is unclear how this proportionality depends on energy. For this reason, a calibration has to be applied. We used the calibration described in [67] and the respective functions:

$$c(E) = 0.22039 \exp\left(-\frac{\left(\frac{E}{MeV} - 1.5049\right)^2}{(1.1842)^2}\right) \frac{PSL}{\#p} \tag{5.2}$$

for $E < 2.11\,\mathrm{MeV}$ as well as

$$c(E) = 0.33357 \left(\frac{E}{MeV}\right)^{-0.91377} \frac{PSL}{\#p} \tag{5.3}$$

for $E > 2.11\,\mathrm{MeV}$, where $\#p$ is the proton number (see figure 5.10).

As each position corresponds to an energy range and not to a single energy based on the initial energy map (see figure 4.11) a final energy map for particle energies impinging on the IP was deduced. Afterwards the average was taken over the energy range for each position in order to assign an effective energy calibration factor to each position.

This was done for each point on a grid with a millimeter resolution with subsequent transformation of proton number to a dose in arbitrary units by using the average deposited energy per proton for each position as well as information on the irradiated mass and the final energy map (see figure 4.13). The analysis process in the case of an

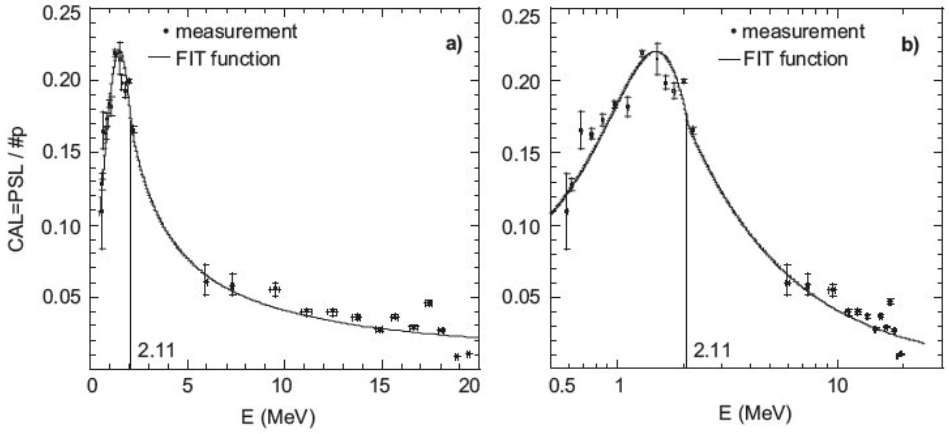


**Figure 5.10** – Calibration performed by Mančić et al [67]: data and fit function shown both with a linear and a logarithmic energy axis. The two different fitting regimes are separated by a solid line at 2.11 MeV. **Mančić et al, Review of Scientific Instruments, 79, 2008** [67]

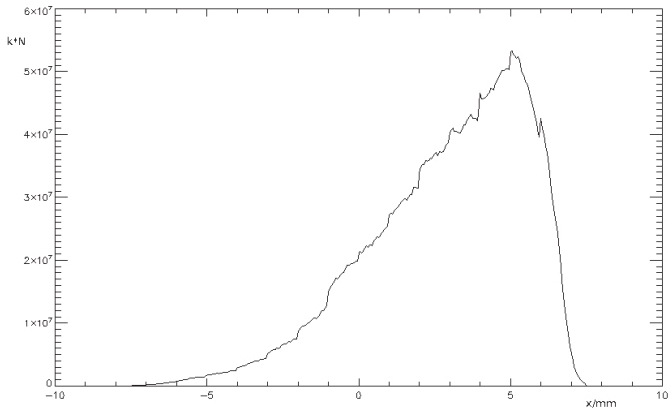


**Figure 5.11** – Proton number distribution within the cell port. The x-axis is position in mm along the dispersion axis and the y-axis gives for each position the overall proton number per pixel width times the calibration factor k (along a perpendicular line).

example shot illustrated by figures 5.6 to 5.11 results in a dose of 109338 (a.u.) for this shot. In a final step, the transition to the actual dose in mGy was done by applying the scanner-specific PSL calibration factor of

$$1/k = 0.0004 \tag{5.4}$$

from equation 5.1, so as to account for the scanner sensitivity, which yields a dose of 44 mGy for the example shot.

The resulting shot to shot fluctuation over the whole set of shots is ±70 % (see figure 5.12). There is no clear trend in how the dose per shot fluctuates over the course of a day (see figure 5.13). Causes for this large standard deviation might be variations in laser performance as well as in target focus alignment. The deposited energy dose per shot in the cells is determined as $D = 23\,\mathrm{mGy} \pm 3\,\mathrm{mGy}$, i.e. with a dose uncertainty of 13 %.

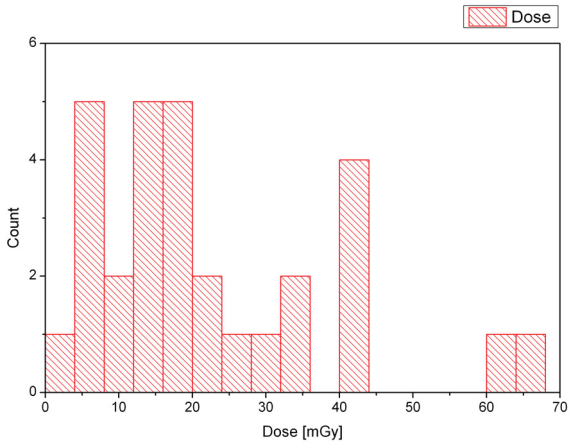


**Figure 5.12** – This histogram illustrates the strong shot to shot fluctuations of the delivered dose. The deposited dose was found to be $D = 23\,\mathrm{mGy} \pm 3\,\mathrm{mGy}$.

## 5.5 Employing Protons for Biological Experiments

The dose deposition and measurement system was used for biological experiments with adherent A549 cancer cells at the ARCTURUS facility in Düsseldorf. The biological methodology and results are explained in detail in [7]. A short summary is given here in order to place the physical results described so far in a wider context and to show the application of the dosimetric method.

### 5.5.1 Biological Endpoints

The aim of the experiment was to compare the effects of pulsed proton irradiation caused by a laser-plasma interaction and continuously accelerated protons as well as

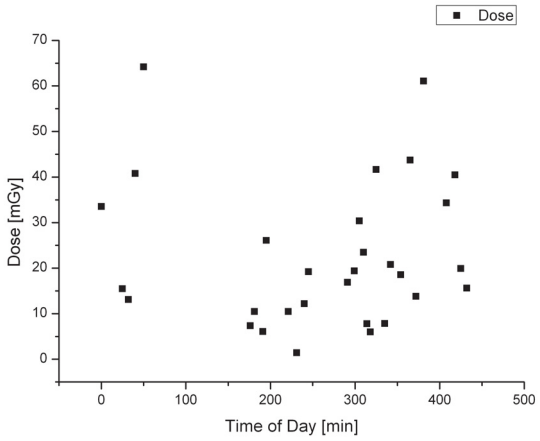


**Figure 5.13** – There is no evident trend in the dose fluctuations over the course of a day. The time of day is given as duration from noon.

irradiation by X-ray. Of specific interest were DNA double strand breaks, i.e. direct DNA damage and its repair over time as well as nitroxidative stress, which is an indirect cause of DNA damage and connected to the creation of radical molecules by radiation. [87, 88, 89, 90, 91]

### 5.5.2 Irradiation with Conventionally Accelerated Protons

The experiments with continuously accelerated protons were performed with a Van de Graaff accelerator at the Physikalisch Technische Bundesanstalt (PTB) in Braunschweig for two different LET values. A scattering gold foil of 0.5 $\mu$m thickness combined with a Faraday cup to measure the proton flux under a scattering angle was used to indirectly determine the number of protons impinging on the cells [7]. These number measurements were performed by Dr. Giesen and PTB staff, whereas the SRIM simulations to determine the deposited energy per proton for this setup were performed by the author of this work.

### 5.5.3 Main Results

The dose response curve for DNA double strand breaks with laser accelerated protons was found to be linear (see figure 5.14). We did not see a significant difference in DNA double strand break damage or in the repair of such damage between conventionally accelerated protons and the laser accelerated proton pulse (see figure 5.15).

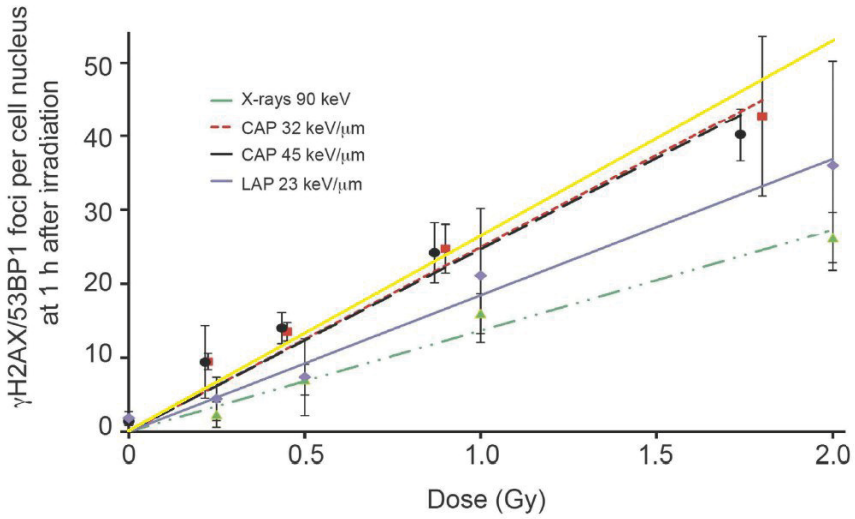


**Figure 5.14** – Dose response curves for different irradiation modalities. The x-axis indicates the dose used for irradiation and the y-axis the number of foci of a biological marker, which serves as an indication for DNA double strand breaks. CAP stands for conventionally accelerated protons (black and red data points and fit lines) and LAP for laser-accelerated protons (purple data points and fit line). In addition, there was also irradiation with X-rays (green data points and fit line). No significant difference was found between LAP and CAP. The LAP dose is based on the evaluation of an irradiated CR39 plastic in the cell port for one typical laser shot. The yellow line, added for this graph, results as a fit for the LAP data points if the results from the IP evaluation of 30 shots are used instead. The similarity to the dose response by the conventionally accelerated protons is apparent. Foci measurements by Raschke. **Raschke et al, Scientific Reports, 85, 2016, modified** [7]

This is consistent with what other groups have found. [4, 92, 5] There was a clear difference in the nitroxidative stress response which was measured with the help of the marker nitrotyrosine (see figure 5.16). The nitrotyrosine levels were significantly lower for the cells irradiated with the pulsed protons accelerated by laser-plasma interaction than for the cells irradiated with the conventionally accelerated protons from the Van de Graaff generator. To our knowledge this is the first time a difference was found between laser-accelerated protons and conventionally-accelerated protons with regards to their biological effects. A preliminary interpretation of this result points to the short time scale of dose deposition, comparable to that of radical production as a possible

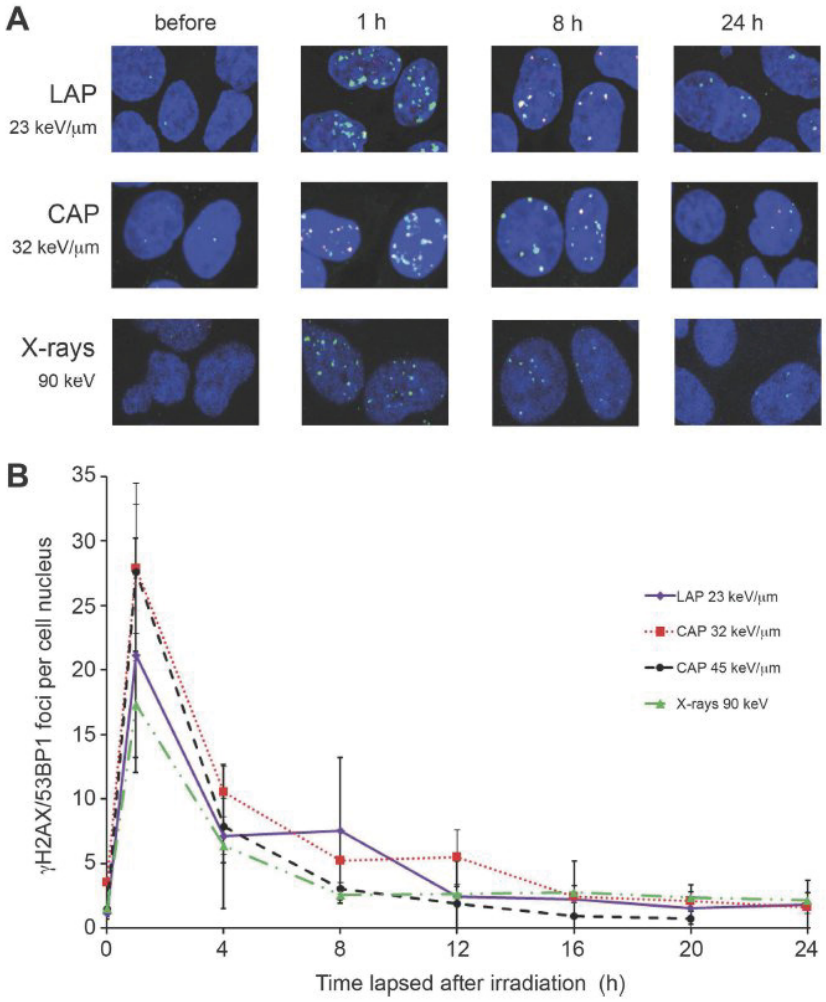


**Figure 5.15** – A) Microscope images of foci in cells at different times after irradiation for different irradiation modalities. B) Kinetic measurement which shows the repair of DNA damage over time. The repair curve looks similar for all four irradiation modalities. Measurements by Raschke. **Raschke et al, Scientific Reports, 85, 2016** [7]

cause of this difference. [7]

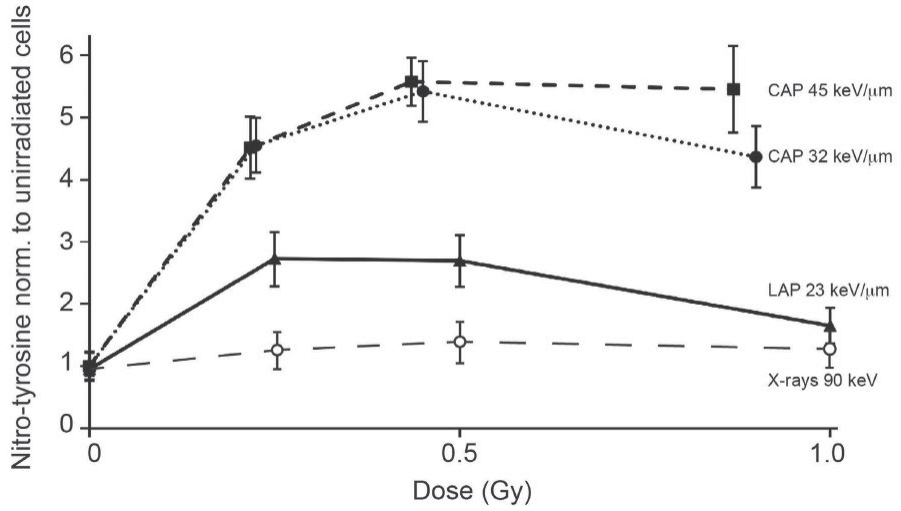


**Figure 5.16** – Nitrotyrosine measurements by Raschke for different doses and irradiation modalities. Nitrotyrosine serves as a marker for nitroxidative stress. There is a clear difference between cells irradiated with proton pulses resulting from laser-plasma interaction and those accelerated from a Van de Graaff accelerator. This holds true over the entire investigated dose range. **Raschke et al, Scientific Reports, 85, 2016** [7]

# Chapter 6

# Ion Acceleration in Two Beam Experiments

## 6.1 Introduction

Different combinations of target and laser parameters lead to different physical effects in general and to different absorption as well as ion acceleration processes in particular (see chapter 2 for details and examples). Within the last decades a wide variety of different conditions and outcomes has already been investigated by modifying the laser and the target parameters. For the most part, solid or gas targets have been used. Applying several laser pulses to a target and varying the delay between them allows for an even wider range of target conditions to be explored due to the effect of the first laser on the target. Therefore, what was originally a solid target has become a plasma in some state by the time the second interaction takes place, provided both beams do not arrive simultaneously.

If the shifted pulses overlap in time, one could consider the experiment a laser-solid interaction with a single modified laser pulse. However, if the pulses do not overlap, it may be more appropriate to consider both interactions independently, one a laser-solid interaction - which of course is also a kind of laser-plasma interaction due to the effect of the prepulse, but where the target geometry is still recognizable from the solid state one - the other a pure laser-plasma interaction, where the plasma may exhibit a geometry very different from the original target. This difference is characterized by a modified electron density profile with an increased scale length, naturally affecting the acceleration processes taking place. Hence, in these cases, the resulting ion spectrum

is really a superposition of two ion spectra from two separate interactions. The ARCTURUS facility offers opportunities to investigate these kind of combined or modified interactions with the help of femtosecond pulses at relativistic intensities.

Markey et al [93] performed double beam experiments, varied the energy ratio of their beams and found that for some settings an increase in cutoff energy and a reduction in particle number in the normal direction occurred, comparing the two beam case to the single beam case. They found that their settings also influenced the angular distribution of the protons. As they performed their experiments at the Vulcan Petawatt facility, their laser parameters were different from ours, with pulse durations of 750 fs and pulse energies on the order of 100 J, while investigating two delay settings, 750 fs and 1.5 ps.

Jürgen Böker [11] performed two beam ion acceleration experiments at the ARTURUS facility with varying details. The experiments concerned femtosecond delays as well as picosecond delays of up to 100 ps and more, with a focus on the proton spectra along the normal axis. One main acceleration process identified in that work was enhanced TNSA in the case of femtosecond delays, where the sheath created by the first interaction is modified by the second one.

Another process described was magnetic vortex acceleration, which was predicted to lead to energetic protons ejected from the target at an angle of about 30 °. [11] In order to build on this work and to investigate further the long delay range of up to 3 ns as well as the acceleration mechanisms taking place and whether they deviate from TNSA, the experiments described in the upcoming section of this thesis were performed. Experimental and evaluative differences include setting up a second Thomson parabola at a 10 ° angle to the target normal as well as an added plasma mirror in the second beam line (see section 3.4). There was an additional focus on particle numbers as well as on ions other than protons. We focused exclusively and in detail on longer delays in the picosecond and nanosecond range for which both laser pulses do not overlap in time.

## 6.2 Setup and Diagnostics

In this experiment we shot with two beams on a 5 $\mu$m thick titanium with the help of the tape driver described in section 4.4.1. The setup is shown in figure 6.1. One beam (beam 2) hit at an angle of incidence of 40 ° while the other hit at 0 °. Our diagnostics were two Thomson parabolas with adherent MCPs aligned at angles of 0 ° and 10 ° to the target rear side, as well as multi-color reflectometry [94]. We varied

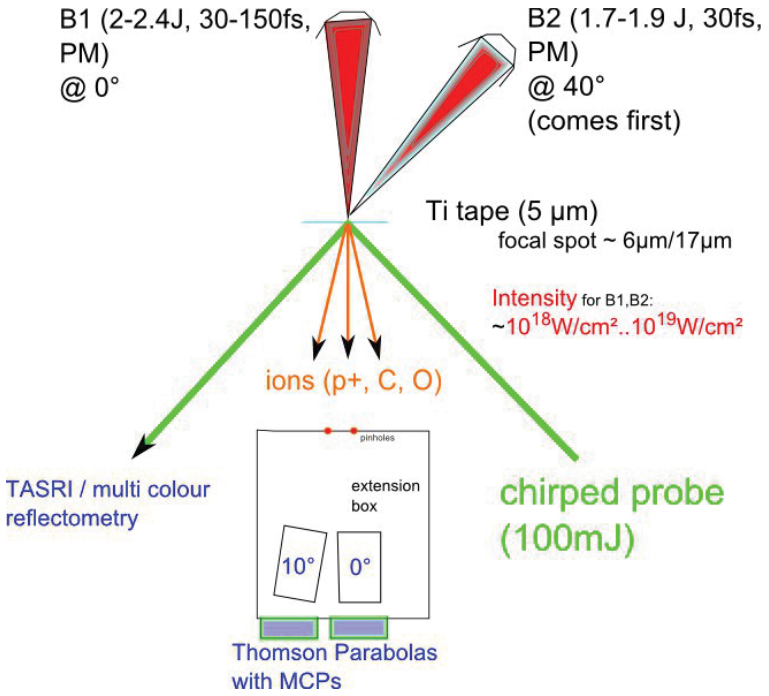


**Figure 6.1** – Experimental setup for the two beam campaign. The pulse energies refer to the energy before compression. Compressor, plasma mirror and beam line account for a throughput of 40 % leading to a combined energy on target of $\approx 1.6\,\mathrm{J}$.

the delay between the two interactions. Most of the time, beam 2 came first. Unless explicitly stated otherwise, all delays mentioned refer to this setting. The delay of beam 1 relative to beam 2 was varied by moving a delay stage in the third amplifier of beam 2 and could be increased by up to 3 ns. For several shots we also had beam 1 come first, with a delay of up to 60 ps before beam 2 arrived on target. We varied the pulse duration of beam 1 as well as the focal spot size of beam 2. A larger focal spot size was advantageous for the overlap between both beams in order to guarantee a common interaction area, whereas a smaller spot size increased the intensity.

Beam 1 was focused at all times, corresponding to a spot size of $6\,\mu\mathrm{m}$, but its pulse duration was varied from 150 fs to 30 fs and its beam energy before compression was in the range of 1.9 J to 2.4 J. This corresponded (with a throughput of $\sim 40\,\%$ of the energy due to passage of compressor, plasma mirror and beam line) to an intensity range of $5 \cdot 10^{18}\,\mathrm{W/cm^2}$ to $3 \cdot 10^{19}\,\mathrm{W/cm^2}$ for beam 1, which impinged at normal incidence. Beam 2 on the other hand was always compressed to 30 fs and for two out of three shot series it was defocused to a spot size of $17\,\mu\mathrm{m}$ in order to guarantee a better overlap

between both beams. For the final shot series it was focused in order to achieve higher intensities. Its beam energy varied from 1.7 J to 2.1 J before compression, corresponding to an intensity range of $3 \cdot 10^{18}$ W/cm$^2$ to $2 \cdot 10^{19}$ W/cm$^2$ for beam 2, which hit the target under an angle of incidence of 40 °. We varied the interaction conditions as described above and did a delay scan for each of them.

This thesis focuses on the results of the Thomson parabola evaluation, specifically of the heavier ions from the contaminant layer, i.e. carbon. The author of this work participated in the experiments, which were a collaborative effort, and evaluated the carbon ion data discussed in the following sections. One aim of the analysis of the carbon ions was to determine whether there would be any change in the spectra in the case of two beam shots, e.g. a signature of a shock or in general an acceleration mechanism other than TNSA. Other points of interest included the cutoff energies as well as the particle numbers and their dependence on the delay. In both of the latter two cases as well as in looking for signatures of different ion acceleration processes, interesting results were obtained.

## 6.3 Spectral Analysis

The spectra were recorded by taking photographs of the fluorescent screen of the MCP behind each Thomson parabola (figure 6.2). By using the Matlab based program TPA from the University of Belfast[1], it was possible to extract a background corrected Thomson parabola spectrum from this (figure 6.3). For some conditions, this initial step was performed by M. Wiltshire, for other conditions by the present author.

A calibration was performed for ions and protons, relating MCP signal to particle number depending on particle energy (see figure 6.4). The author of this work participated in the experiments as well as in the etching and the production process of track microscopy images of PADC plastics used for this purpose. For C4+ and C5+ a linear fit was obtained (see figure 6.5).

When one considers the case of C4+ (see figure 6.5), while the resulting linear function it is a good fit for the lower energies, the data point for 7 MeV clearly does not conform to the fit. However, there were doubts as to the validity of this data point as it is possible that the track count on the CR39 was inaccurate and hence this data point was ignored and the fit was used even for higher energies in spite of the apparent

[1] in versions by Domenico Doria and Aaron Alejo

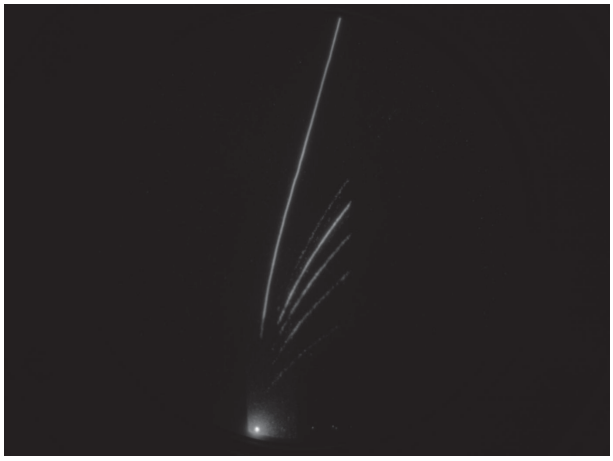

**Figure 6.2** – Picture taken from the 0 ° MCP on a typical two beam shot. In the lower part the zero point due to x-ray radiation can be seen. Different parabola-like traces indicate different ion species depending on their charge to mass ratio. Closer proximity to the zero point indicates a higher particle energy.

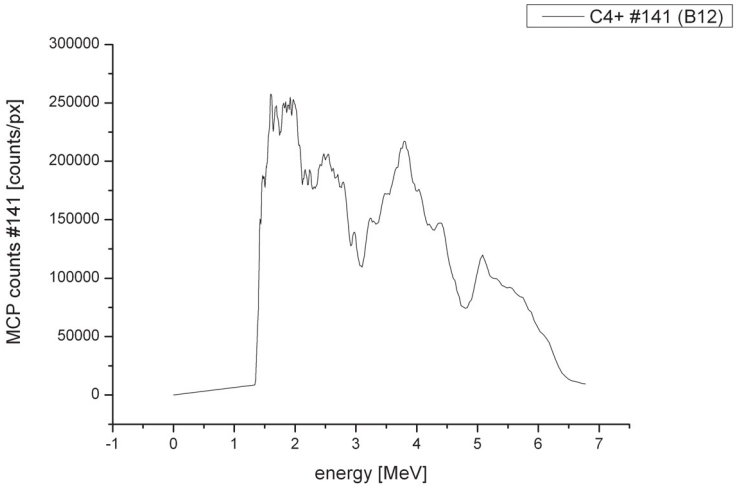


**Figure 6.3** – Background corrected spectrum of C4+ ions in the MCP signal shown in figure 6.2. The peaks indicate brighter parts in the C4+ trace.

mismatch. While this introduces a possible overestimation of the particle numbers of energies above 5.5 MeV, it does not significantly affect the results as most particles are in an energy range below that point. Any resulting overestimate of the number of ions with such energies has a very limited effect on the overall number of ions in the spectrum, which was analyzed. Similar considerations apply to the investigation of the

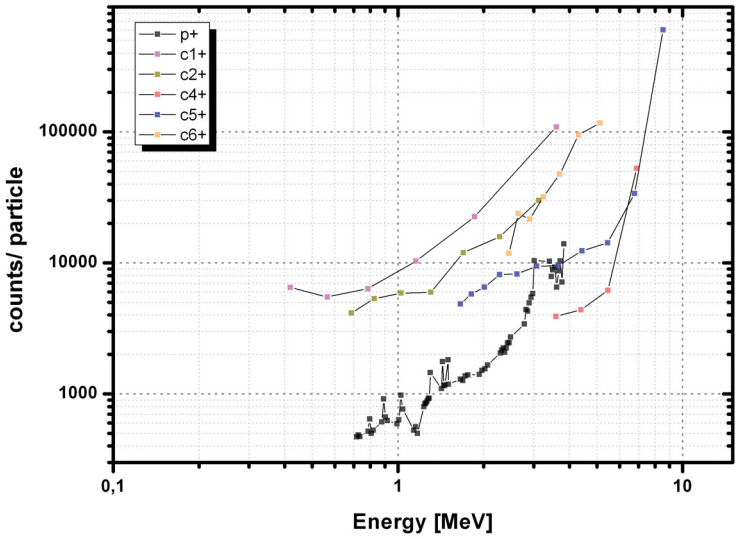


**Figure 6.4** – Calibration of MCP response for different particle types depending on particle energy (graph: M. Swantusch)

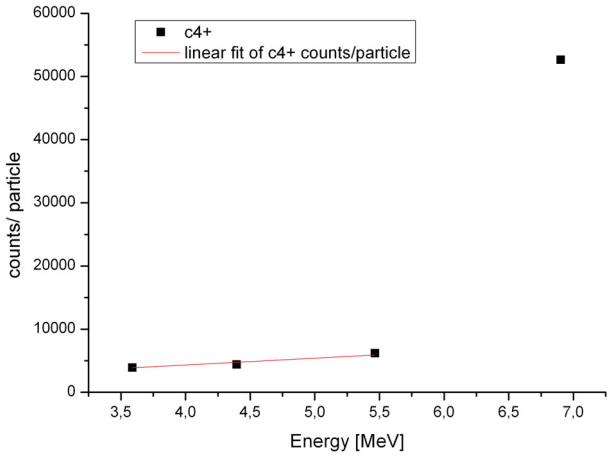


**Figure 6.5** – Linear fit for C4+ calibration.

spectral shape itself as in this energy range the signal is consistently very low and any correction of an overestimate there would not matter for the outcome of a qualitative judgement as it would only further depress an already low signal. The cutoff energy was determined directly from the MCP images without applying this calibration and

therefore is not affected by it at all.

After application of the calibration, the resolution of the MCP was taken into account as the energy resolution of the Thomson parabola has a strong dependence on the energy (figure 6.6) with a larger, i.e. worse, resolution at higher energies. This is due to the reduced deflection of faster particles by the electrical and magnetic fields.

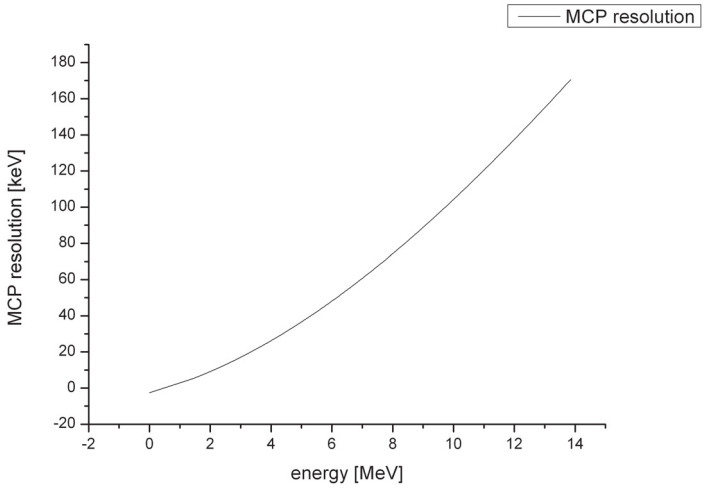


**Figure 6.6** – Spatial resolution of the MCP depending on energy

Taking into account both calibration and resolution significantly alters the appearance of the spectrum (figure 6.7). No evidence of a deviation from TNSA as the dominant acceleration mechanism was found in the spectral shape of the ion signal derived from the 0 ° Thomson parabola MCP images for all shots regardless of shot parameters or delay, because there was no clear deviation from an exponential decay as expected for TNSA (see figure 6.8).

Contrary to this, in the case of the protons from the same campaign, spectral features were discovered which deviate from those expected from a pure TNSA interaction. These will be discussed in Marco Swantusch's thesis. For the C4+ and C5+ ion spectra however, no such features were found.

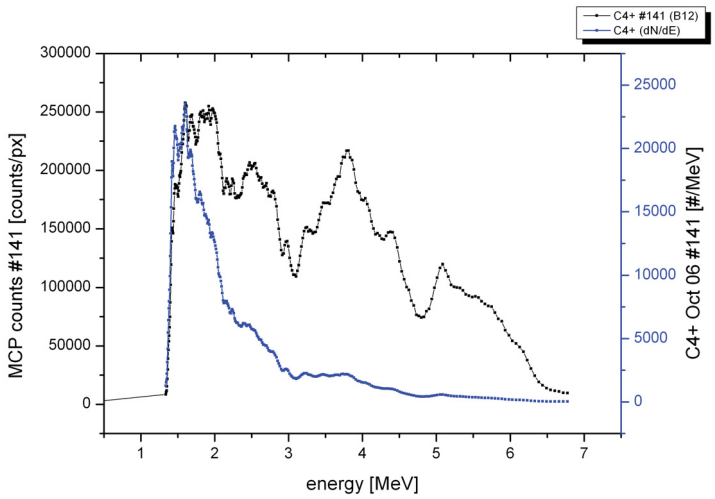


**Figure 6.7** – Application of calibration as well as resolution in order to obtain a spectrum $dN/dE$ (blue) from the original MCP spectrum (black). A clear difference in structure is apparent, as the peaks are gone.

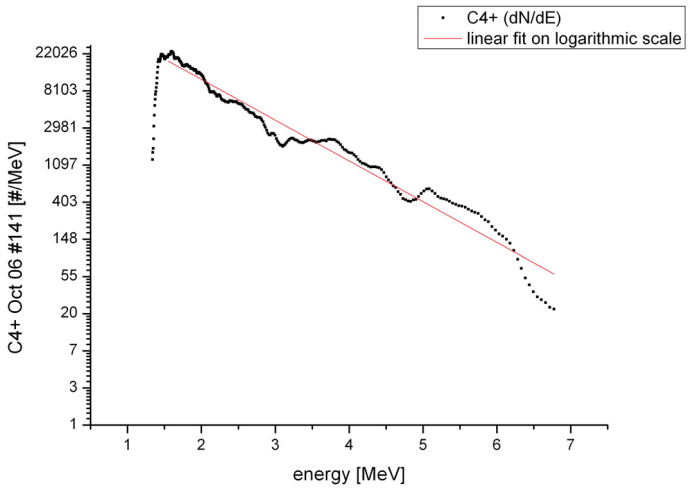


**Figure 6.8** – Mapping the $dN/dE$ spectrum from 6.7 onto a log scale confirms the structural similarity to an exponential decay as is expected from TNSA, because a straight line can be fitted.

## 6.4 Cutoff Energies

After analyzing the cutoff energy depending on time delay between the two beams it was found that for each of the shot conditions analyzed there were peaks. For two sets of conditions where we investigated shorter delays of 200 ps and less ($I_{B2} = 3 \cdot 10^{18}\,\mathrm{W/cm^2}$ in both cases, $I_{B1} = 10^{19}\,\mathrm{W/cm^2}$ and $I_{B1} = 6 \cdot 10^{18}\,\mathrm{W/cm^2}$ respectively), we found those peaks for C4+ at 25 ps (figure 6.9) and 50 ps to 70 ps (figure 6.11) respectively. For C5+ for one condition we found a short delay peak at 25 ps (figure 6.10), similar to C4+, while for the one with lower intensity in beam 1 it was at 50 ps (figure 6.12).

The most pronounced of these peaks is C5+ at 250 ps found during a long delay scan with delay of up to 3 ns for shot conditions of $I_{B2} = 2 \cdot 10^{19}\,\mathrm{W/cm^2}$ (focused) and $I_{B1} = 3 \cdot 10^{19}\,\mathrm{W/cm^2}$ (see figure 6.14). C4+ has an elevated region ranging from 250 ps to 500 ps (see figure 6.13). For these conditions we did not find any clear peak in the early delay range, possibly there is one at C5+, but if so it is not exceptionally pronounced. If one normalizes the result to the single beam cutoff energy, there is a peak for C4+ at a delay of 125 ps.

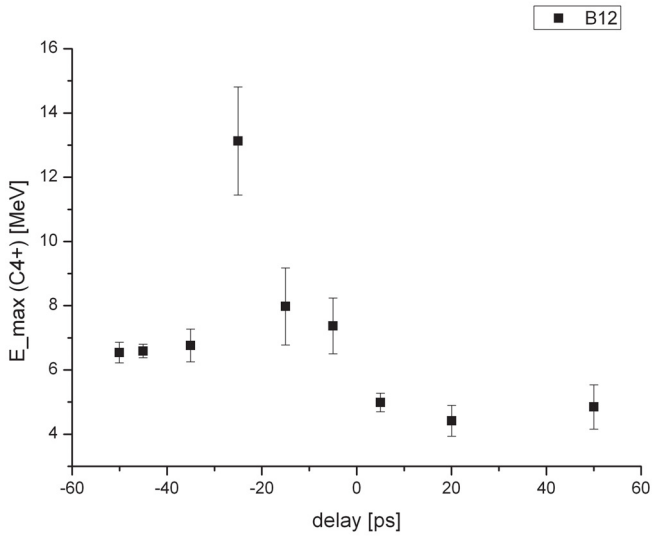


**Figure 6.9** – Cutoff Energies: C4+. Shot conditions: $I_{B2} = 3 \cdot 10^{18}\,\mathrm{W/cm^2}$ (defocused) and $I_{B1} = 10^{19}\,\mathrm{W/cm^2}$. There is a clear peak when beam 2 arrives 25 ps before beam 1. Negative delays in this graph refer to B2 arriving first.

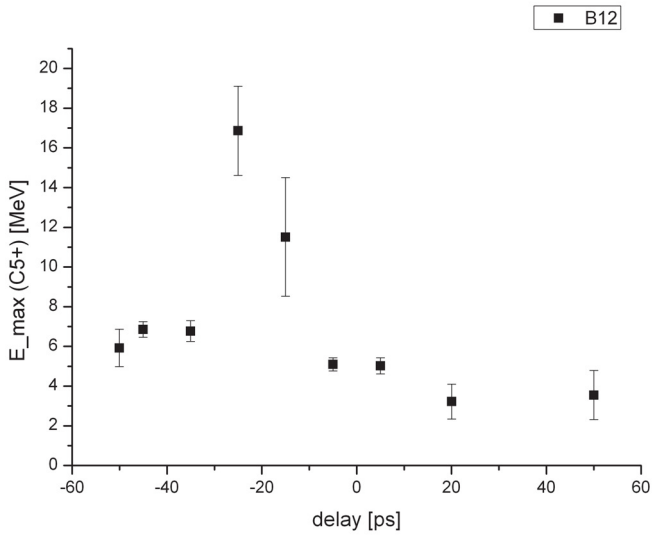


**Figure 6.10** – Cutoff Energies: C5+. Shot conditions: $I_{B2} = 3 \cdot 10^{18}\,\mathrm{W/cm^2}$ (defocused) and $I_{B1} = 10^{19}\,\mathrm{W/cm^2}$. There is a clear peak when beam 2 arrives 25 ps before beam 1. Negative delays in this graph refer to B2 arriving first.

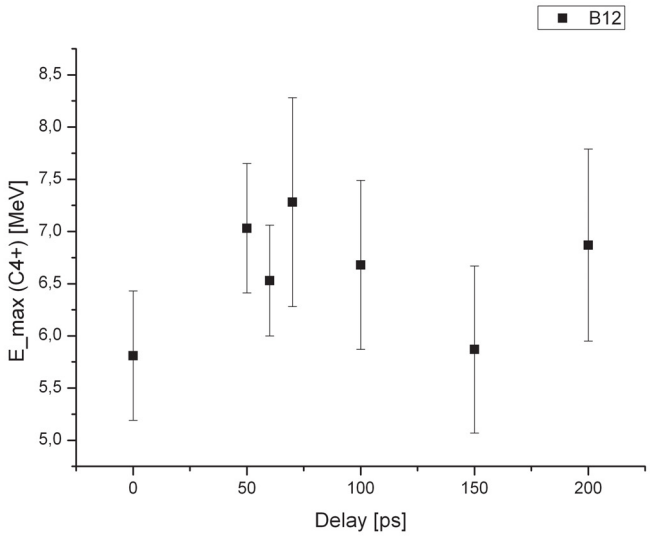


**Figure 6.11** – Cutoff Energies: C4+. Shot conditions: $I_{B2} = 3 \cdot 10^{18}\,\mathrm{W/cm^2}$ (defocused) and $I_{B1} = 6 \cdot 10^{18}\,\mathrm{W/cm^2}$. Increased energies near $50 - 70\,\mathrm{ps}$ delay are apparent. There is an increase compared to the timed case, i.e. a delay of $0\,\mathrm{ps}$ between both beams.

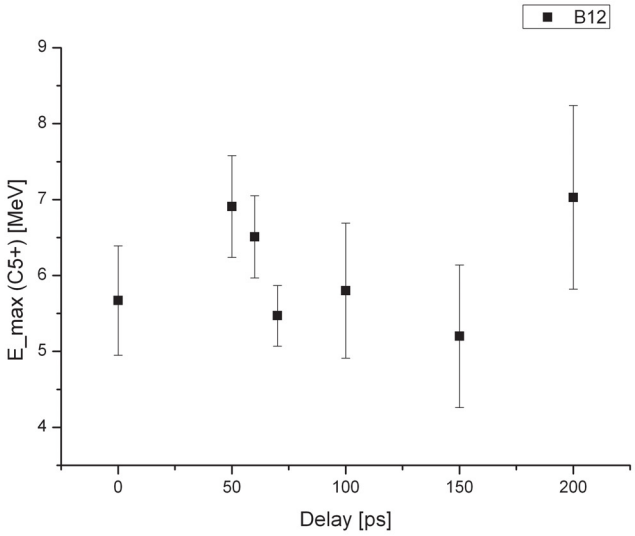


**Figure 6.12** – Cutoff Energies: C5+. Shot conditions: $I_{B2} = 3 \cdot 10^{18}\,\mathrm{W/cm^2}$ (defocused) and $I_{B1} = 6 \cdot 10^{18}\,\mathrm{W/cm^2}$. At $50\,\mathrm{ps}$ and $200\,\mathrm{ps}$ delay, there is an increase compared to the timed case.

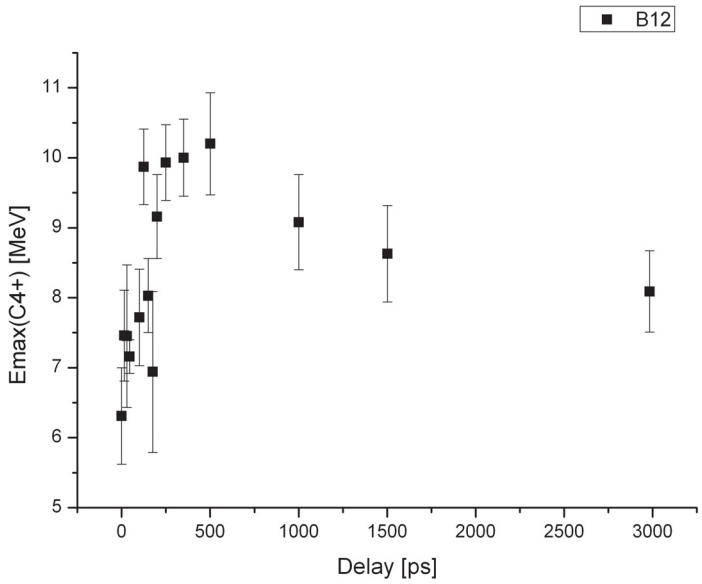


**Figure 6.13** – Cutoff energies of C4+. Shot conditions: $I_{B2} = 2 \cdot 10^{19}\,\mathrm{W/cm^2}$ (focused) and $I_{B1} = 3 \cdot 10^{19}\,\mathrm{W/cm^2}$. C4+ shows an elevated region in the 250 ps to 500 ps delay range

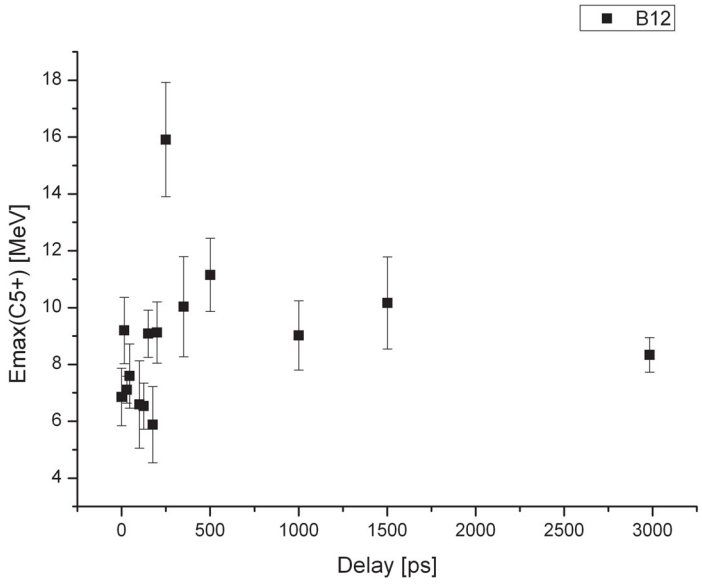


**Figure 6.14** – Cutoff energies of C5+. Shot conditions: $I_{B2} = 2 \cdot 10^{19}\,\mathrm{W/cm^2}$ (focused) and $I_{B1} = 3 \cdot 10^{19}\,\mathrm{W/cm^2}$. There is a clear peak for C5+ at a delay of 250 ps.

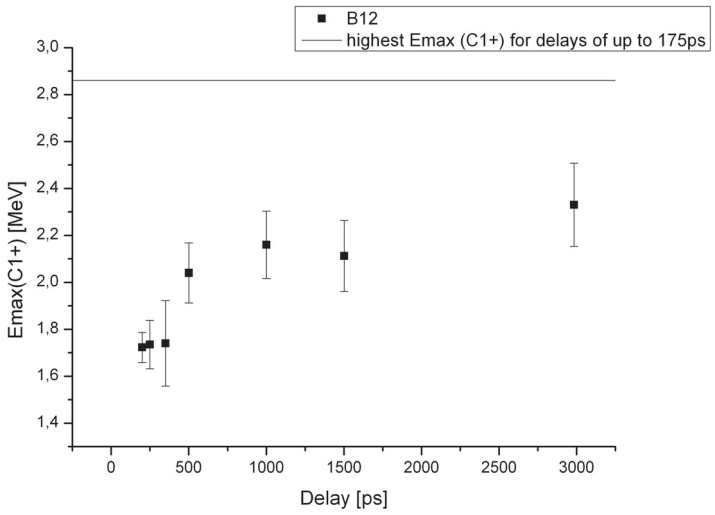


**Figure 6.15** – Delay vs Cutoff Energy C1+ where the black line at $\approx 2.9\,\mathrm{MeV}$ indicates optimal cutoff energy within delay range of up to 175 ps. Shot conditions: $I_{B2} = 2 \cdot 10^{19}\,\mathrm{W/cm^2}$ (focused) and $I_{B1} = 3 \cdot 10^{19}\,\mathrm{W/cm^2}$.

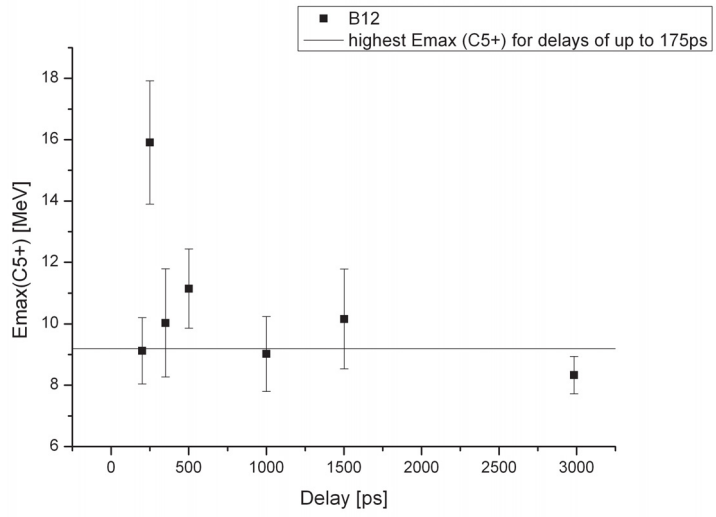


**Figure 6.16** – Delay vs Cutoff Energy C5+ where the black line at $\approx 9\,\mathrm{MeV}$ indicates optimal cutoff energy within delay range of up to 175 ps. Shot conditions: $I_{B2} = 2 \cdot 10^{19}\,\mathrm{W/cm^2}$ (focused) and $I_{B1} = 3 \cdot 10^{19}\,\mathrm{W/cm^2}$. For C5+, there is an increase at longer delays compared to the optimal cutoff energy at short delays.

For the long delay scan, there is a clear increase in cutoff energy for the 250 ps to 500 ps delay range. This increase appears to increase with the charge state. Figures 6.15 and 6.16 clearly show that the optimal delay shifts to this range for higher charge states (C5+) as opposed to shorter delays for low charge states (C1+).

During the long delay scan there were different conditions as far as the energy in beam 1 was concerned. For this reason and in order to account for single beam energy fluctuations and drifts in general, it makes sense to consider the ratio of B12 cutoff energy to the average cutoff energy for single beam shots before and after the two beam shot series for each delay. This normalized, dimensionless quantity will be called *gain* in the following. If one considers the gain for these conditions (see figure 6.17), the increase with charge state in this delay range is still evident.

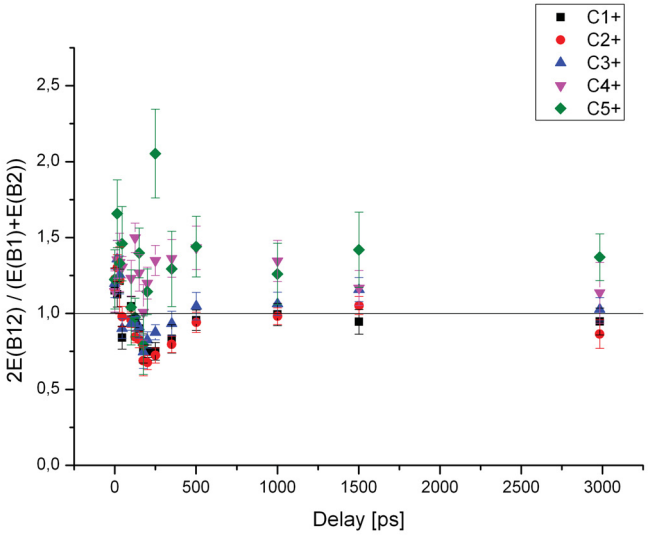


**Figure 6.17** – Gain for C1+, C2+, C3+, C4+ and C5+: ratio of cutoffs B12 and the average of B1 and B2 vs delay. The black line indicates the case where the two beam cutoff is the same as the single beam cutoff. Shot conditions: $I_{B2} = 2 \cdot 10^{19}\,\mathrm{W/cm^2}$ (focused) and $I_{B1} = 3 \cdot 10^{19}\,\mathrm{W/cm^2}$. In the delay range of 250 ps to 500 ps,C4+ and C5+ ions show a higher gain than those with lower charge states.

There is a tendency of an increase in gain with the charge state for all intensity conditions near the peak delays (see figures 6.18 and 6.19 as illustrative measurement results and 6.20 as a condensed result over all measurements). This is not explained by the naturally expected increase in cutoff energy with charge state due to the larger

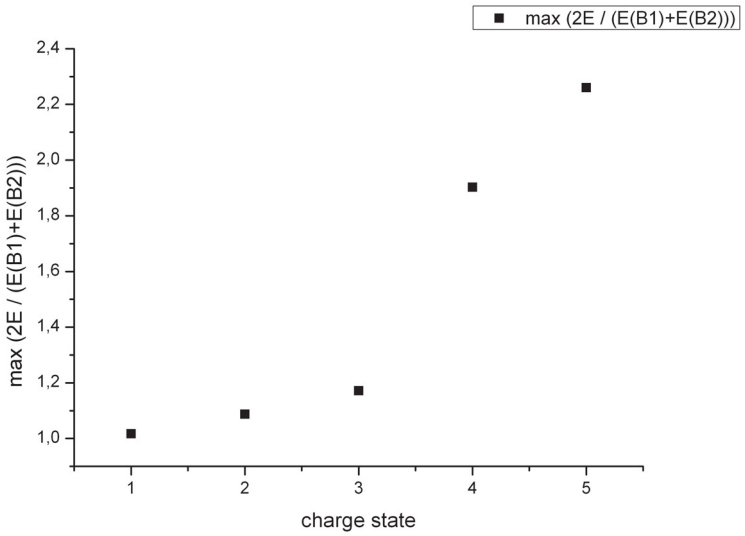


**Figure 6.18** – Charge state vs maximum gain (highest gain value over all delays). Shot conditions: $I_{B2} = 3 \cdot 10^{18}\,\mathrm{W/cm^2}$ (defocused) and $I_{B1} = 10^{19}\,\mathrm{W/cm^2}$. There is a clear increase of gain with charge state, at least comparing C4+ and C5+ to the other ionization stages.

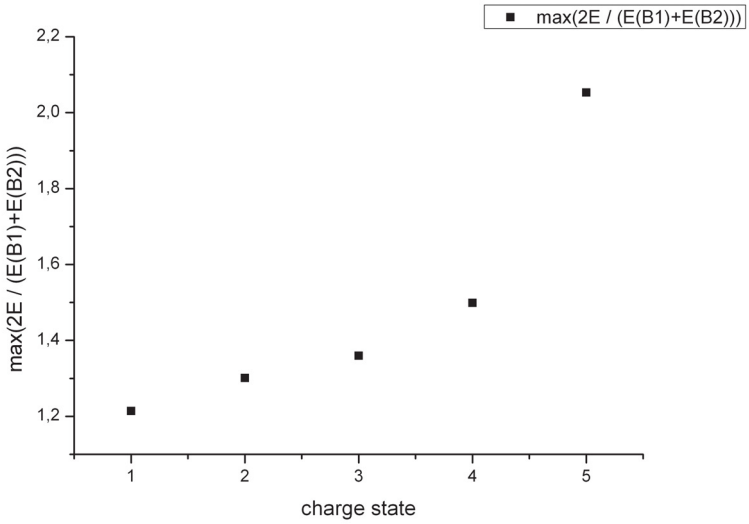


**Figure 6.19** – Charge state vs maximum gain (highest gain value over all delays). Shot conditions: $I_{B2} = 2 \cdot 10^{19}\,\mathrm{W/cm^2}$ (focused) and $I_{B1} = 3 \cdot 10^{19}\,\mathrm{W/cm^2}$. There is a clear tendency of an increase of gain in charge state.

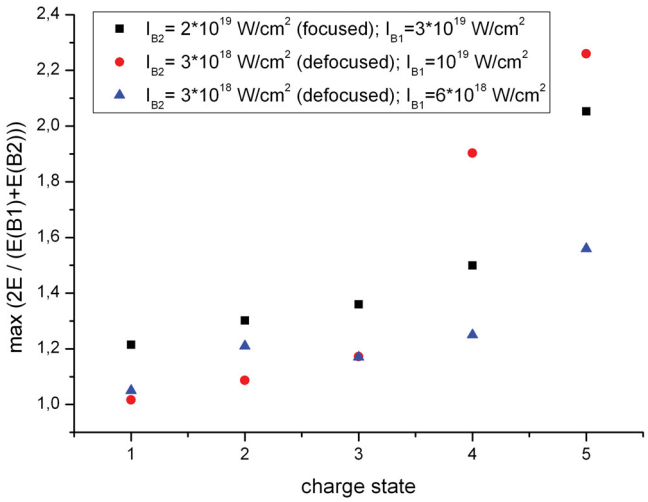


**Figure 6.20** – Charge state vs maximum gain for all analyzed days (highest gain value over all delays for a given day). There is an increase of gain with charge state for all experimental conditions. The gain over delay results for the different conditions are shown in figures 6.17, 6.21 and 6.22 respectively.

acceleration by the electrostatic field, as we are considering the normalized case.

If two beam cutoff energies were to scale with the charge state as do single beam cutoff energies, one would not expect this behaviour. According to one estimate [95], the cutoff energy depends on hot electron temperature $T_h$, laser pulse duration $\tau_L$, ion density $n_i$ as well as charge state $Z$ and mass of the ion species $m_i$ as follows:

$$E_{max} = 2Zk_BT_h \left( \ln \left( \frac{\omega_{pi}\tau_L}{\sqrt{2e_E}} + \sqrt{1 + \frac{\omega_{pi}^2\tau_L^2}{2e_E}} \right) \right)^2 \tag{6.1}$$

Here $\omega_{pi} = \sqrt{\frac{n_i Z^2 e^2}{\epsilon_0 m_i}}$ is the ion plasma frequency and $e_E$ is Euler's number. Considering first the timed case for the interaction of two beams, the ratio of the cutoff energy in two beam to single beam case would reduce to

$$\frac{E_{both}}{E_{single}} = \frac{T_{both}}{T_{single}} \tag{6.2}$$

as all other terms in equation 6.1 cancel out, because they are identical in both cases. The energy ratio in equation 6.2 depends on a property of the respective plasmas only

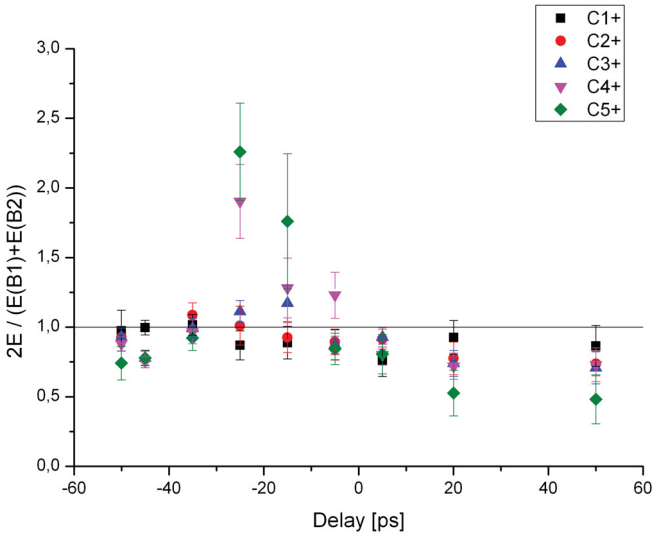


**Figure 6.21** – Gain for C1+, C2+, C3+, C4+ and C5+: ratio of cutoffs B12 and the average of B1 and B2 vs delay. The black line indicates the case where the two beam cutoff is the same as the single beam cutoff. Shot conditions: $I_{B2} = 3 \cdot 10^{18}\,\mathrm{W/cm^2}$ (defocused) and $I_{B1} = 10^{19}\,\mathrm{W/cm^2}$. It can be seen that the peak at 25 ps described earlier is limited to C4+ and C5+. In the peak region, the highest charge states show the highest gain, whereas further away from the peak region, the C5+ gain is actually lower than the gain of the other ion species. Negative delays in this graph refer to B2 arriving first.

and is independent of the accelerated ion type under consideration, contrary to the experimental results (figure 6.20), which show a clear dependence. If the increase in cutoff energy had been found at the timed case, the argument that TNSA cannot explain the behaviour of the gain would be straightforward.

As discussed, the optimal delay is different from the timed case and $\omega_{pi}$ may well differ as the ion density depends on the delay and hence is not identical in the two beam case and the single beam case. A stronger increase of $n_I$ with the charge state due to the expansion of the plasma would be required to explain the observed increase of gain with charge state. There is no apparent reason why an expanded plasma should display a stronger increase of $n_I$ with charge state compared to a less expanded plasma.

Furthermore, it could be argued that the two beam case consists of two separate interactions, making a direct comparison to a single interaction difficult. However, given

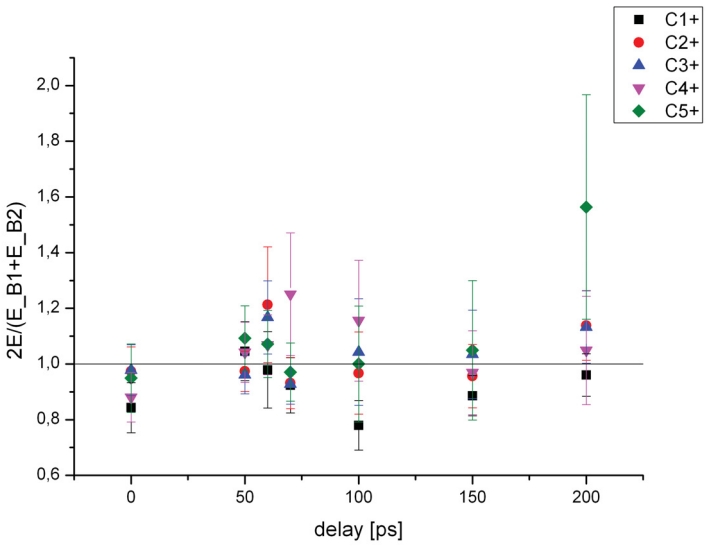


**Figure 6.22** – Gain for C1+, C2+, C3+, C4+ and C5+: ratio of cutoffs B12 and the average of B1 and B2 vs delay. The black line indicates the case where the two beam cutoff is the same as the single beam cutoff. Shot conditions: $I_{B2} = 3 \cdot 10^{18}\,\mathrm{W/cm^2}$ (defocused) and $I_{B1} = 6 \cdot 10^{18}\,\mathrm{W/cm^2}$. There is only a clear increase over the single beam cases at a delay of 200 ps for C5+ ions. Compared to the other conditions, the tendency of an increase with charge state over most delays is not evident.

that the gain depends on the delay, the second interaction is responsible for the increase in cutoff energy and therefore one may compare the second interaction of the two beam case with the single interaction in the single beam case and the above argumentation holds.

The increase of the maximum gain with charge state may therefore suggest the existence of an acceleration mechanism other than TNSA near the optimal delays.

The protons of our data set also show an optimum cutoff energy away from the timed case which will be discussed by Marco Swantusch's upcoming thesis. The same was found after a new analysis of C4+ and C5+ ions in the data of Böker for the double beam cases. However, there is one difference: While for C4+ there was a strong dependence on delay in Böker's data as well, the C5+ data show much less variation in cutoff energy compared to the results presented in this work. There was still some variation, but most of the time the C5+ cutoff energy was located between 9 MeV and 10 MeV.

What can account for the peak behaviour described earlier and for the dependence on delay in general? The main effect of a longer delay on the target conditions lies in an increased scale length as the plasma has had more time to expand. For this reason, the second interaction can differ according to delay.

As will be discussed in the section on the number of ions and their dependence on the two beam interaction 6.5, there can be marked differences in the first interaction between the single beam case and the two beam case. However, there is no reason to assume that there are any delay dependent two beam effects in the first interaction. As the combined prepulse effects are present for all delays and all experimental laser conditions investigated (see section 6.5), they are most likely due to the nanosecond ASE pedestal level, which is assumed as constant within each measurement, as opposed to any pre- or post-pulses. It is therefore assumed in the following that any dependencies on delay by the cutoff energies are exclusively due to different target conditions at the time of the second interaction.

A better absorption usually leads to a stronger interaction as more energy is being transferred to the plasma and in particular to the hot electrons and through them, eventually, to the ions. At least in the case of normal TNSA one would expect a deterioration with increased scale length as a steeper gradient is in general better for most absorption mechanisms. Next, we shall investigate this dependence for the standard absorption mechanisms.

Vacuum heating requires a sharp density gradient as does jxB heating. Anomalous skin heating requires the mean free path of the electrons to exceed the skin depth and therefore a smaller skin depth and implicitly a sharper density gradient is advantageous for this process too (see sections 2.2.5 and 2.2.7).

Resonance absorption is notably different from most other absorption mechanisms in that it actually prefers a somewhat increased scale length for maximum efficiency[14]. The optimal conditions for resonance absorption (see theory section 2.2.4 for discussion) are fulfilled when the Denisov function (figure 2.4) is at a maximum value, implying $\xi \approx 1$.

To assume that we interact with the target at a $0\,^\circ$ angle of incidence would however exclude resonance absorption as an explanation due to $\xi(\theta = 0\,^\circ) = 0$. Even allowing for an angular deviation of up to $1\,^\circ$ due to inaccurate alignment would require an unrealistically large scale length of $L = 23.8\,\mathrm{mm}$ to achieve optimal conditions. However, the second beam whose beam path is along the $0\,^\circ$ axis interacts with an already expanded target and due to the $40\,^\circ$ angle of incidence of the first beam, an asymme-

try has already been imprinted on the plasma expansion. This allows in principle for oblique angles of incidence to occur even in a well aligned setup with normal incidence on the original solid-state target surface.

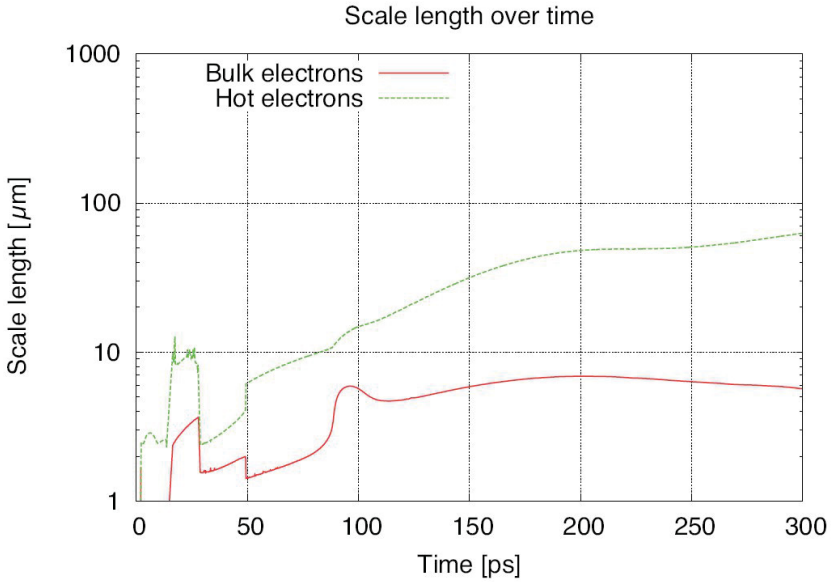


**Figure 6.23** – 1D simulation result by Jürgen Böker [11]. This graph shows the dependence of scale length on delay for conditions considered by him, which were similar to ours, but not identical (same basic experimental setup, but beam 2 did not have a plasma mirror at that time). After an early peak, a rise in scale length of the bulk electrons after 100 picoseconds followed by a stagnation phase or a slow decline is apparent. **Böker, Heinrich Heine Universität Düsseldorf, 2015**

For a quantitative approximation of the scale lengths to be expected at long delays and a qualitative assessment of their dependence on delay, results of a 1D simulation performed by Jürgen Böker were consulted (see figure 6.23) [11]. The situation which was simulated was quite similar to ours, but beam 2 (the beam which arrives first) did not have a plasma mirror at the time. Assuming a qualitatively similar temporal development, but possibly with different durations due to the new plasma mirror (differences in conditions include less energy being deposed which might influence the expansion speed), an optimal scale length of approximately $L = 3\,\mu$m would be consistent with a late peak in cutoff energy as observed in the experiment. From this value one can derive the resulting angle of incidence:

$$kL = 7.854\,\mu\mathrm{m}^{-1} \cdot 3\,\mu\mathrm{m} = 23.562$$

$$\Rightarrow \xi = 2.87 \cdot \sin\theta$$

Setting $\xi = 1$ and solving for the angle of incidence gives

$$\theta = \arcsin(0.349) = 20.4\,^\circ$$

Therefore, if we assume an angle of incidence $\theta \approx 20\,^\circ$ by the second beam with the critical surface resulting from the first interaction and its plasma expansion during the delay, it makes sense for us to observe a peak in the cutoff energy at a late delay, as was indeed the case.

Graph 6.23 also shows a subsequent smooth and slow transition to smaller scale lengths, which also fits well with the smooth decline in ion cutoff energies observed for later delays. Another feature of the dependence of scale length on delay is an early peak (seen at $\approx 25\,\mathrm{ps}$ in the figure) which could explain the early peaks in the cutoff energy that were observed for most conditions (see figures 6.9 to 6.12) as the scale length approaches the optimal value.

As discussed, we varied the intensity during our experiments, which might serve to explain the apparent day to day shift in the peak position which we observed as the development of the plasma expansion would also be expected to change along with the laser parameters. While one could thus be tempted to hypothesize a shift to shorter peak delays with increased intensity and while this would be very plausible as well in view of the proposed explanation, experimentally this is not consistently the case for all observed peaks. The dependence of optimal delay on intensity of the beams therefore remains an open question.

To summarize, our results concerning the ion cutoff energies qualitatively fit very well with the temporal behaviour one would expect from an expanding plasma, approaching and then passing the optimal scale length for resonance absorption. How the absorbed energy is further transferred to the ions is of course a separate matter, but also of interest. The spectral shapes under $0\,^\circ$ (see section 6.3) show no deviation from what one would expect of TNSA, a process also consistent with some rather unusual behaviour concerning the ion numbers which will be discussed in the upcoming section 6.5.

On the other hand, the dependence of the gain on the charge state which was discussed in this section clearly points in another direction as do the strong spectral peaks that sometimes appear in the 10 ° spectra. They will be treated in detail in section 6.6 and cannot be explained by a pure TNSA interaction. The obvious conclusion is that a combination of TNSA and at least one other ion acceleration process took place during our experiments.

## 6.5 Particle Numbers

What is immediately apparent when analyzing the number of particles is that C4+ has an order of magnitude more particles than C5+ (see figure 6.24 for example). Comparing the cases of single beam and double beam, it is also evident that shots where only beam 2 was used result for all possible parameters and delays in higher particle numbers than shots with both beams (see figure 6.30 for example). In the following, these two results will be discussed.

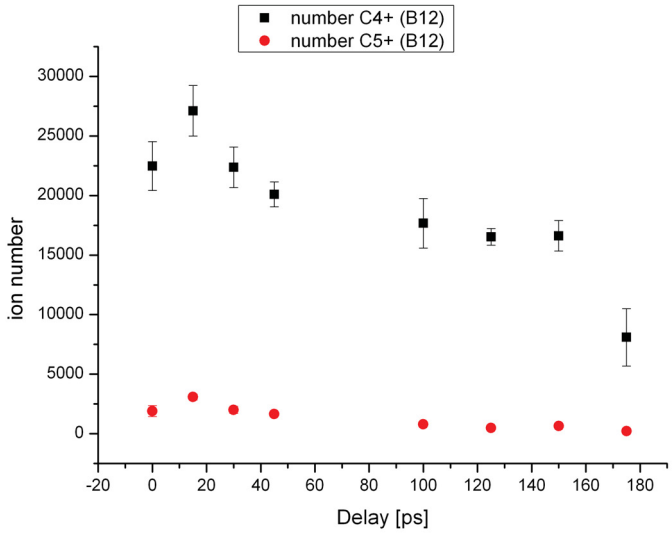


**Figure 6.24** – Particle number vs delay, short delay only ($\Delta t \leq 175\,\mathrm{ps}$). Numbers are integrated over the calibrated spectra on the 0 ° MCP. Shot conditions: $I_{B2} = 2 \cdot 10^{19}\,\mathrm{W/cm^2}$ (focused) and $I_{B1} = 3 \cdot 10^{19}\,\mathrm{W/cm^2}$.

The fact that many more C4+ than C5+ ions impinged on the MCP can easily be accounted for by comparing the ionization potentials and the ionization rates for C4+ and C5+. The ionization potential of C4+ is 64.5 eV whereas the ionization potential

of C5+ is much higher at 392 eV. In [96] Hegelich et al compared collisional and field ionization rates of C4+ and C5+ for a given electric field. The ratio of the collisional ionization rates of C4+ and C5+ they determined was approximately 6, which is roughly consistent with our results, whereas the ratio of the respective field ionization rates was a staggering $5 \cdot 10^{10}$ due to the large difference in ionization potential, which means that only a negligible amount of C5+ ions is created by field ionization.

Another observable effect is that for each condition the numbers depend on delay: For the first set of conditions ($I_{B2} = 3 \cdot 10^{18}\,\mathrm{W/cm^2}$ (defocused) and $I_{B1} = 6 \cdot 10^{18}\,\mathrm{W/cm^2}$), there are increased numbers of C4+ ions at 0 ps as well as at 60 ps with a roughly comparable situation for C5+ ions (see figures 6.25 and 6.26 respectively) .

For the second set of conditions ($I_{B2} = 3{\cdot}10^{18}\,\mathrm{W/cm^2}$ (defocused) and $I_{B1} = 10^{19}\,\mathrm{W/cm^2}$) there are clear peaks for both C4+ and C5+ at 50 ps, while a second peak is seen at 25 ps in the case of C4+ whereas for C5+ there is an increase in particle number as well, but it is not significant (see figures 6.27 and 6.28 respectively).

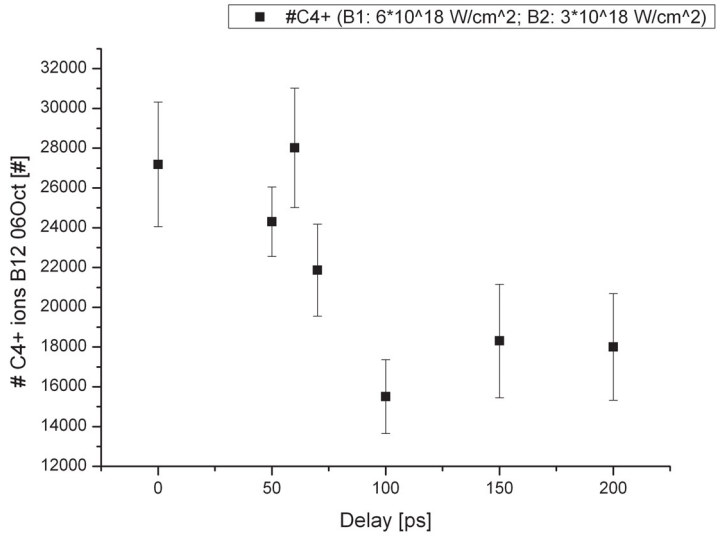


**Figure 6.25** – Particle number vs delay for C4+. Numbers are integrated over the calibrated spectra on the 0° MCP. Shot conditions: $I_{B2} = 3 \cdot 10^{18}\,\mathrm{W/cm^2}$ (defocused) and $I_{B1} = 6 \cdot 10^{18}\,\mathrm{W/cm^2}$.

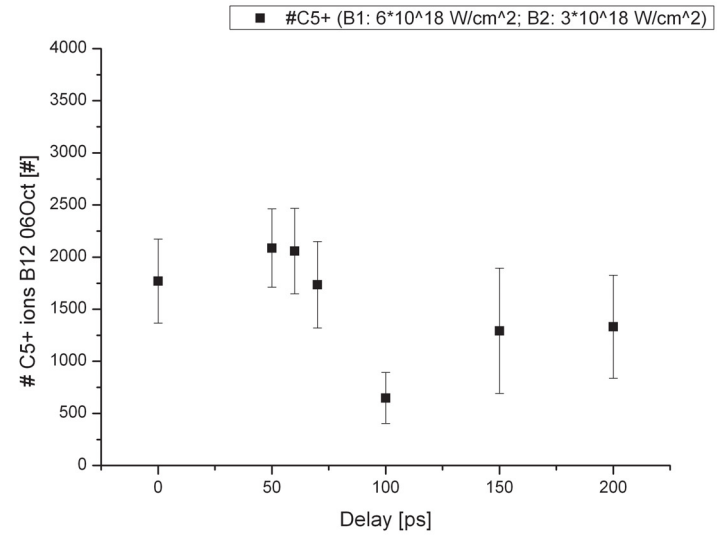


**Figure 6.26** – Particle number vs delay for C5+. Numbers are integrated over the calibrated spectra on the 0° MCP. Shot conditions: $I_{B2} = 3 \cdot 10^{18}\,\mathrm{W/cm^2}$ (defocused) and $I_{B1} = 6 \cdot 10^{18}\,\mathrm{W/cm^2}$.

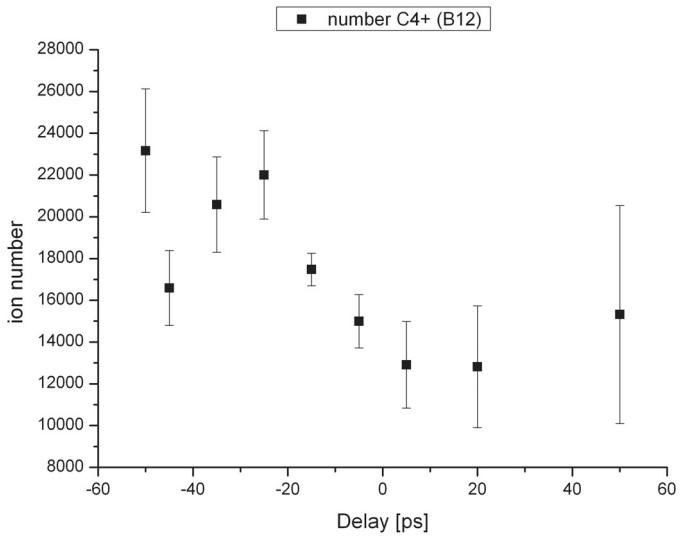


**Figure 6.27** – Particle number vs delay for C4+. Numbers are integrated over the calibrated spectra on the 0° MCP. Shot conditions: $I_{B2} = 3 \cdot 10^{18}\,\mathrm{W/cm^2}$ (defocused) and $I_{B1} = 10^{19}\,\mathrm{W/cm^2}$. Negative delays in this graph refer to B2 arriving first.

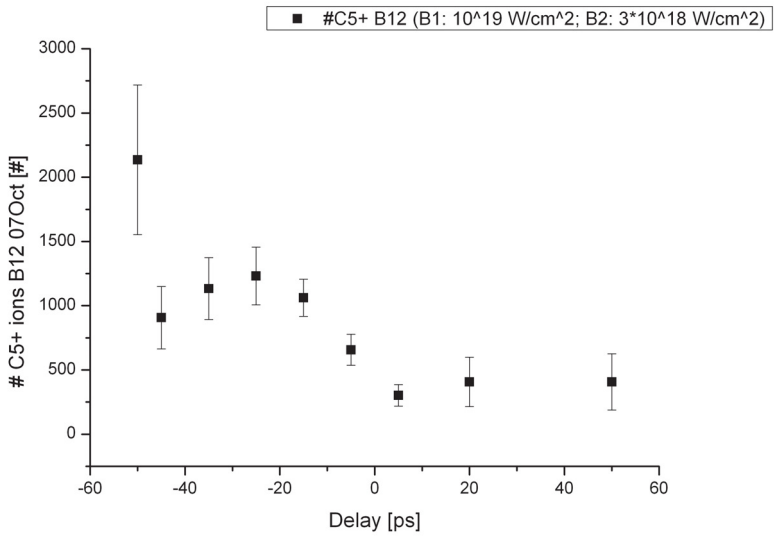


**Figure 6.28** – Particle number vs delay for C5+. Numbers are integrated over the calibrated spectra on the 0° MCP. Shot conditions: $I_{B2} = 3 \cdot 10^{18}\,\mathrm{W/cm^2}$ (defocused) and $I_{B1} = 10^{19}\,\mathrm{W/cm^2}$. Negative delay times in this graph refer to B2 arriving first.

For the third set of conditions (long delay scan, $I_{B2} = 2 \cdot 10^{19}\,\mathrm{W/cm^2}$ (focused) and $I_{B1} = 3 \cdot 10^{19}\,\mathrm{W/cm^2}$) there is a clear peak at 15 ps for both C4+ and C5+, while there is a clear second peak at 1500 ps for C4+, which is not apparent in the case of C5+ (see figure 6.29).

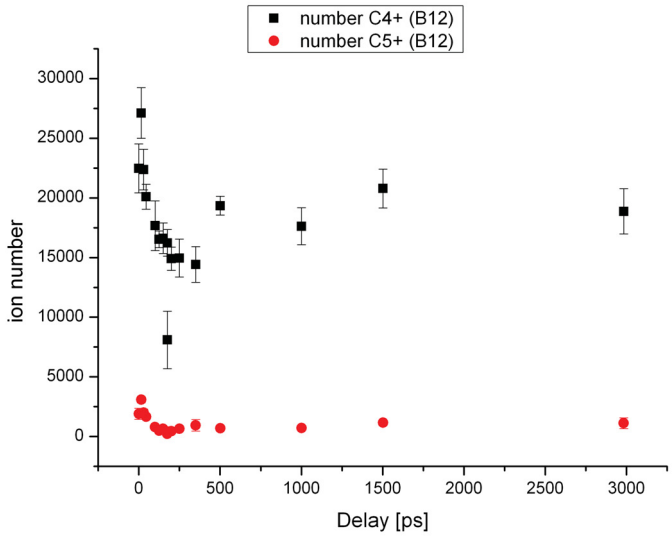


**Figure 6.29** – Particle number vs delay for C4+ and C5+ ions for the long delay scan. Numbers are integrated over the calibrated spectra on the 0 ° MCP. Shot conditions: $I_{B2} = 2 \cdot 10^{19}\,\mathrm{W/cm^2}$ (focused) and $I_{B1} = 3 \cdot 10^{19}\,\mathrm{W/cm^2}$. After an initial increase, both curves show a decrease until about 500 ps, when the numbers appear to stay at a slightly increased level.

Apart from the difference in numbers between C4+ and C5+ and the peaks, there is another noteworthy result from the measurement series, namely that shots with both beams consistently produce fewer ions than shots by beam 2 only. See figures 6.30 and 6.31.

An analysis of the C4+ and C5+ ion data of Böker confirms reduced particle numbers in the two beam case for most modalities, with the exception of an extremely defocused setting (focal spot size of 100 $\mu$m). Reduced numbers in the two beam case were also found in an analysis by Marco Swantusch of the proton data from the campaign described in this work, the results of which will be discussed in his thesis.

At first sight the reduced ion numbers in the two beam case run counter to expectations, as in the two beam case one expects the MCP to accumulate particles from both interactions and the first interaction should be the same as in the case of a single

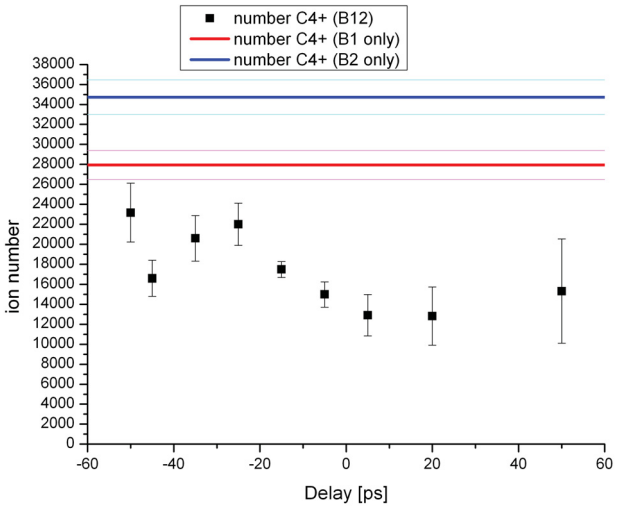


**Figure 6.30** – Comparison of particle numbers for single beam (B1, B2) and double beam shots (B12) for C4+ ions. Numbers are integrated over the calibrated spectra on the 0 ° MCP. Shot conditions: $I_{B2} = 3 \cdot 10^{18}\,\mathrm{W/cm^2}$ (defocused) and $I_{B1} = 10^{19}\,\mathrm{W/cm^2}$. Negative delays in this graph refer to B2 arriving first.

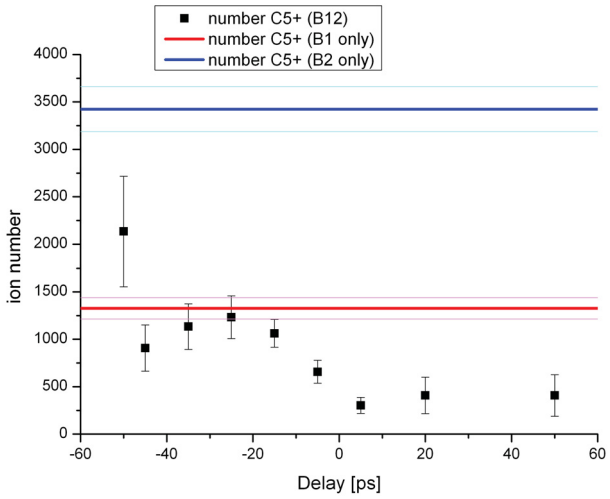


**Figure 6.31** – Comparison of particle numbers for single beam (B1, B2) and double beam shots (B12) for C5+ ions. Numbers are integrated over the calibrated spectra on the 0 ° MCP. Shot conditions: $I_{B2} = 3 \cdot 10^{18}\,\mathrm{W/cm^2}$ (defocused) and $I_{B1} = 10^{19}\,\mathrm{W/cm^2}$. Negative delays in this graph refer to B2 arriving first.

beam shot with only the first beam. Following this line of thought one might easily arrive at the conclusion that the particle number in the two beam case has to be at least as high as in the single beam case of only the first beam arriving. As these graphs unambiguously demonstrate, that is not the case. There is only one possible conclusion, namely that the effect of the first interaction on the MCP signal is different depending on whether it happens in a double beam shot context or in a single shot context. Three possible explanations come to mind, each of which shall be investigated:

1. The second main pulse changes the sheath field and thereby influences the first interaction as it happens. Fewer ions leave the target in the direction of the MCP.
2. The interaction is the same as in the single beam case, but not all ions arrive at the Thomson parabola, due to a disruptive interaction with the subsequent ion pulse or laser pulse.
3. The target is in a different plasma state in the double beam case due to having experienced two prepulses or pedestals instead of just one prior to the first main interaction.

The first explanation can be discounted as the sheath field lasts only on the order of picoseconds at most as this relates directly to the acceleration time of ions (see [96] for an example calculation), whereas even after a delay of 3 ns, i.e. three orders of magnitude more, the effect persists that beam 2 only shots yield higher particle numbers than two beam shots. In the case of sufficiently long delays, the first interaction is already long over by the time the second interaction takes place. The first particle cloud has left the target and has been on its way to the MCP for some time.

The second idea is deserving of closer consideration than the first one and cannot be dismissed as easily. In this model the second interaction or something connected to it disturbs the first particle cloud and changes the number of particles arriving on the MCP. One variation of that approach is that the second plasma cloud might collide with the first one, another that it could create a spatially charged field deflecting the first plasma cloud from the MCP entrance and a third one that the second laser pulse itself may be responsible for disturbing the particle cloud created by the first interaction.

In order to investigate whether effective collision between the two clouds is a plausible idea, consider a relatively slow particle from the first interaction and then ask whether it can be caught in time by a particle from the second interaction in the case of a long delay, i.e. 3 ns. If this is not the case it would stand to reason that collision between

the two plasma clouds cannot possibly serve as an explanation for the reduced particle numbers found in the Thomson parabola traces in the double beam shots.

Let us take a 2 MeV carbon ion as an example particle. Given the limited time of existence of the sheath field during the first interaction, it appears safe to assume that 100 ps after the first interaction it will have reached its final energy and is leaving the target in a direction normal to the sheath field, in the direction of the MCP. It travels at a speed of $v = 0.565 \cdot 10^6$ m/s and within 2.9 ns it crosses a distance of 1.64 cm. Let us assume that for an effective change in direction the collision should occur before our exemplary particle enters the pinhole located at a distance of 70.5 cm from the target as after that both particles involved have a similar trajectory and a collision shouldn't change the trajectory so much as to prevent the particle from being registered on the MCP.

For the remaining 68.86 cm this particle is going to take an additional 121.9 ns. Any particle from the second interaction aiming to catch up with it needs to have a velocity of $v_2 = \frac{70.5\,\mathrm{cm}}{121.9\,\mathrm{ns}} = 0.58 * 10^7\,\mathrm{m/s}$. This corresponds to a kinetic energy $E_2 = 2.1\,\mathrm{MeV}$. From this it is apparent that even for long delays, there is a realistic prospect that some particles from the second plasma cloud will catch up with ions in the first plasma cloud and thus this scenario cannot be dismissed out of hand.

However, if the second cloud were to catch up with the first one, the result would be a new plasma with about double the density and a temperature somewhere in-between both individual cloud temperatures. As the expansion of the plasma depends on its temperature, assuming both plasma clouds have roughly similar temperatures, there is no reason to expect a sufficient reduction in overall particle number arriving at the 0 ° MCP due to any effect by the second particle bunch. This is because the density is significantly increased without a temperature increase sufficient to compensate for it, let alone to further reduce the particle number below that of the single beam case.

As for the idea of a disruptive interaction by the second laser beam with the first ion bunch, it can be rejected as well due to the result of a transparency measurement which showed unambiguously that even after 3 ns delay there is no transmission. It is safe to assume that the expanded plasma cloud from the first interaction has a lower density than the cold plasma remaining in the original target area as the hot electrons, which mostly make up the electrons in that cloud, originally have a density close to critical whereas the target itself is many times overcritical. Therefore, it can be argued that as both of them cannot be underdense, as otherwise there would have been transmission, either both of them have to be overdense or just the original target area even if the

expanded plasma cloud is not. For this reason, the original target area can be assumed to be intransparent. For this reason there is no way the second laser pulse could interact with the accelerated plasma resulting from the first interaction.

Having thus discounted the first two explanations, this leaves us with the third one as the only plausible explanation, namely that the reduced numbers in the two beam case are caused by some effect due to the additional prepulse compared to the case of a single beam with a single prepulse or pedestal. There are several possible ways prepulses might cause such an effect. By means of induced shocks or by creating preplasmas with different scale lengths, they create the pre-conditions for changes in direction or divergence of the resulting ion beam. Due to these effects, depending on the situation, fewer particles may arrive on the MCP in the case of two beam shots than in the case of single beam shots. In the following paragraphs it will be shown why this is a plausible mechanism for our experimental conditions.

In a paper by Santala et al [23] it was demonstrated that the direction of the hot electron beam created by a laser beam incident at an oblique angle depends strongly on the scale length of the pre-plasma with deviations by the electron beam of up to values close to $40\,^\circ$ from the target normal. In the case of scale lengths below $10\,\mu$m a monotonous relation was found. They explained this large deviation by a shift from Brunel type resonance absorption (i.e. vacuum heating, see theory part) to $jxB$ heating, which differ in the direction in which the electrons are accelerated by them. While they only looked at the hot electrons, it stands to reason that the sheath field caused by them would also look different. The added prepulse or pedestal in the two beam case leads to more absorbed energy within the preplasma, which for this reason would have expanded more strongly by the time the first main pulse arrives and which would also exhibit a larger scale length than in the single beam case.

This difference in scale length would subsequently cause a difference in the geometry of the sheath field and ultimately lead to a difference in the direction or starting position of the particle cloud released from the target by the first main interaction. In either case one would then see a different section of the particle beam even if this was the only difference between both cases and hence one would also observe a different particle number when looking under a fixed angle, as was the case in our setup. Given that the maximum particle number would then go in a direction other than normal to the target rear surface, it makes sense that this would cause a reduction in the number of ions arriving at the MCP.

Lindau et al [97] found as well that the ASE pedestal level increasingly changed the

directional deviation of the ion beam from the target normal with increasing level of ASE. This too shows that the prepulse level may be responsible for the reduced numbers of detected ions under a 0 ° angle and hence is able to explain our observations.

To see whether these effects actually might be relevant for our experimental conditions, simulations were conducted with the 1D hydrocode MULTI-fs [98]. The program simulated a 5 ns long prepulse of $10^{10}\,\mathrm{W/cm^2}$ under normal incidence onto a 5 $\mu$m thick titanium foil and then double the intensity for comparison. Figures 6.32a to 6.33b show the simulation results for electron density and electron temperature under these two conditions.

As expected, there is a larger overall expansion, a difference in the position of the critical surface (4 $\mu$m from the nominal front side for the single prepulse case and 6 $\mu$m for the case of two prepulses) as well as a difference in scale length between 1 $\mu$m for the single prepulse case and 1.5 $\mu$m for the two beam case. Data shown by Sentala et al in [23] suggest after applying an approximate linear fit that this difference in scale length might account for about half a degree of difference in emission angle. It seems unlikely that such a small change in angle would lead to a big reduction in particle number resulting from the first interaction in the two beam case compared to the single beam case.

It seems more likely that the large difference in overall expansion (the position of the outer plasma edge in the simulation differs between $-25\,\mu$m and $-35\,\mu$m) could lead to different refraction dynamics in the preplasma, which could change position and shape of the rear side sheath.

There is also a clear difference in temperature between the two cases. This is of relevance as the outward shift in the position of the critical surface is caused by the increased ionization and is not due to the increased expansion in the case of both prepulses.

An increased expansion without a change in ionization would actually lead to a less dense plasma, i.e. a shift of the critical surface closer to the nominal target edge as opposed to the simulation results. The difference in temperature causes a different population distribution in the ionization levels. Given that 1D simulations are prone to overestimating the preplasma expansion[2], it is possible that the actual shift in the position of the critical surface is larger than simulated, while the actual difference in expansion might be smaller.

While these simulation results by themselves do not offer conclusive proof that the

[2] oral communication by Dr. M. Cerchez

differences between one and two prepulses are sufficient to explain the reduced numbers found in the experiment, they nevertheless clearly indicate different target states at the time of the first interaction for the single and two beam case. Furthermore, the effect of the rising edge of the first pulse on the electron density and temperature, which was not simulated here, has to be considered.

If there is a change in refraction and beam path based on differences in expansion due to the increased ASE shoulder of the combined prepulses, the ionization caused by the rising edge would also likely be affected. This would cause a different density profile in general and a different critical surface in particular, affecting absorption and ultimately the number of accelerated ions detected under zero degree during the first interaction.

Therefore, the presence of a second prepulse remains the most likely explanation for the decrease in number of detected ions in the two beam case compared to the single beam case.

Such prepulse effects could also possibly account for some unusual results found in the ion data of Böker, namely a reduction not only in the ion particle number compared to the single beam case, but in rare instances also in the cutoff energies. This does not appear to follow any particular pattern: It clearly occurs for C4+ in a focused case as well as for C5+ in a strongly defocused case, although it is barely significant in the latter case. For all other settings, there was an increase in the cutoff energy compared to the single beam case, similar to results in section 6.4. This does not allow for unambiguous conclusions, but it could be an indication that effects of combined prepulses may also have played a role in the two beam campaign described by Böker [11].

**Figure 6.32**

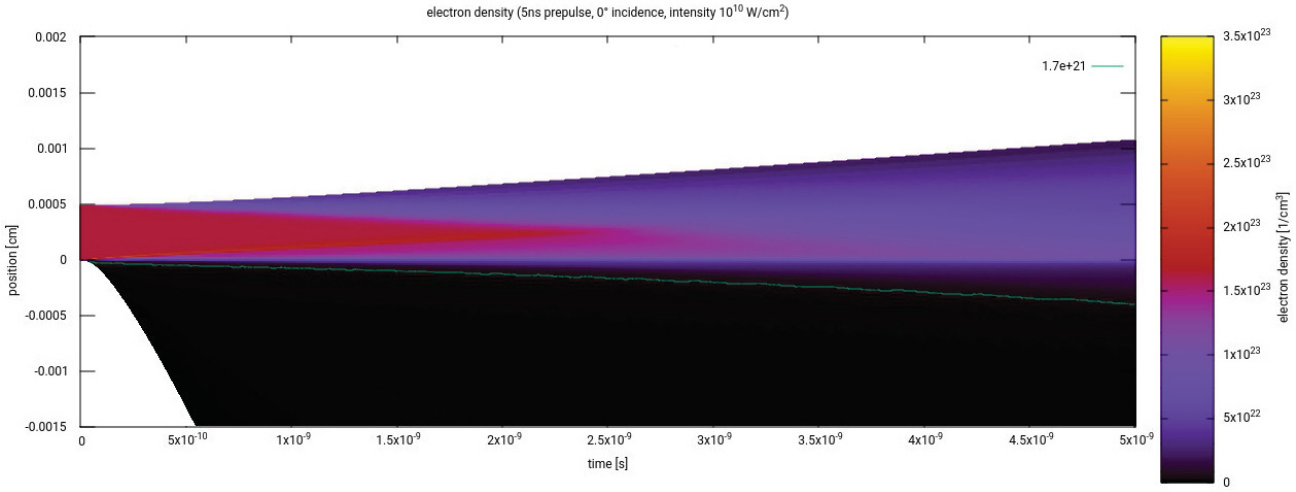


**(a)** Free electron density during a prepulse of 5 ns duration with an intensity of $10^{10}\,\mathrm{W/cm^2}$ under normal incidence on a 5 $\mu$m thick titanium target. 1D simulation with MULTI-fs. Hydrodynamic tables used for aluminium instead of titanium due to availability, ionization energies for the simulated energies are similar. Segment of simulation result ranging from $-15\,\mu$m to $20\,\mu$m. Brighter colours indicate higher free electron density. The turquoise line indicates the position of the critical surface with an electron density of $1.7 \cdot 10^{21}\,\mathrm{cm^{-3}}$.

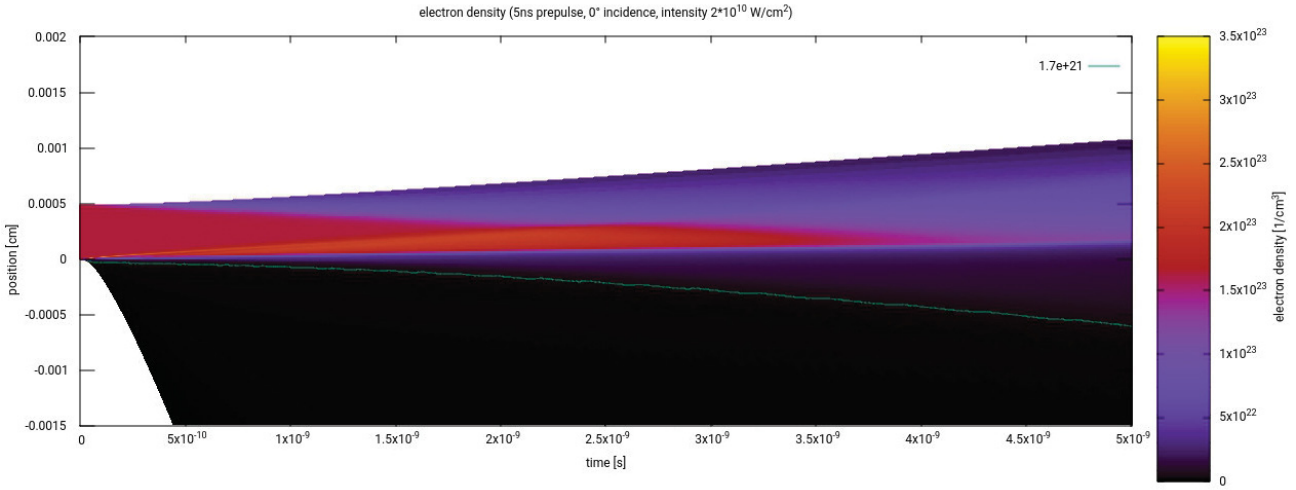


**(b)** Free electron density during a prepulse of 5 ns duration with an intensity of $2 \cdot 10^{10}\,\mathrm{W/cm^2}$ under normal incidence on a 5 $\mu$m thick titanium target. 1D simulation with MULTI-fs. Hydrodynamic tables used for aluminium instead of titanium due to availability, ionization energies for the simulated energies are similar. Segment of simulation result ranging from $-15\,\mu$m to $20\,\mu$m. Brighter colours indicate higher free electron density. The turquoise line indicates the position of the critical surface with an electron density of $1.7 \cdot 10^{21}\,\mathrm{cm^{-3}}$. Compared to the previous simulation, it is apparent that there is an increase in free electron density, which is due to a higher degree of ionization caused by the increased heating (see figures 6.33a and 6.33b).

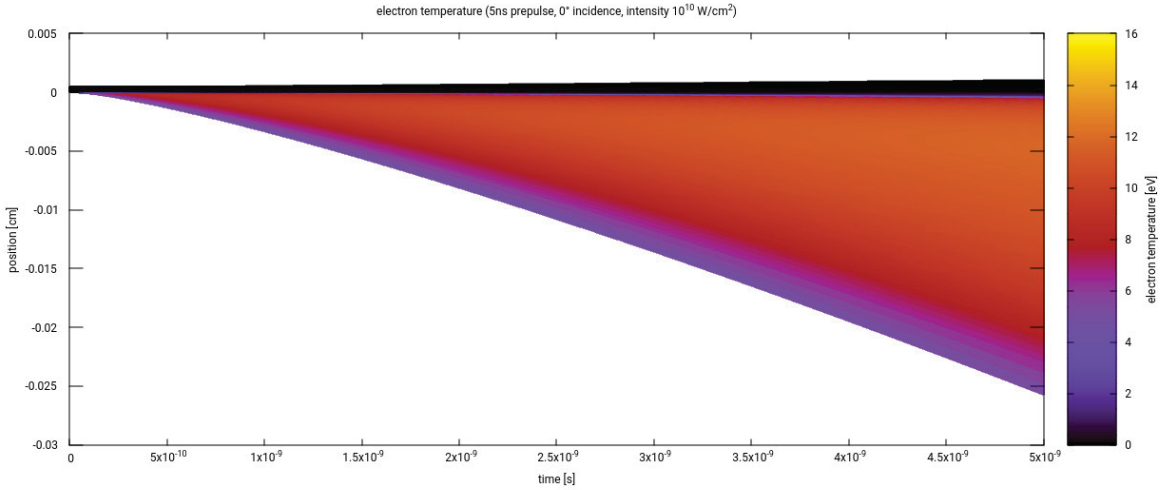


**(a)** Electron temperature during a prepulse of 5 ns duration with an intensity of $10^{10}\,\mathrm{W/cm^2}$ under normal incidence on a 5 $\mu$m thick titanium target. 1D simulation with MULTI-fs. Hydrodynamic tables used for aluminium instead of titanium due to availability, ionization energies for the simulated energies are similar.

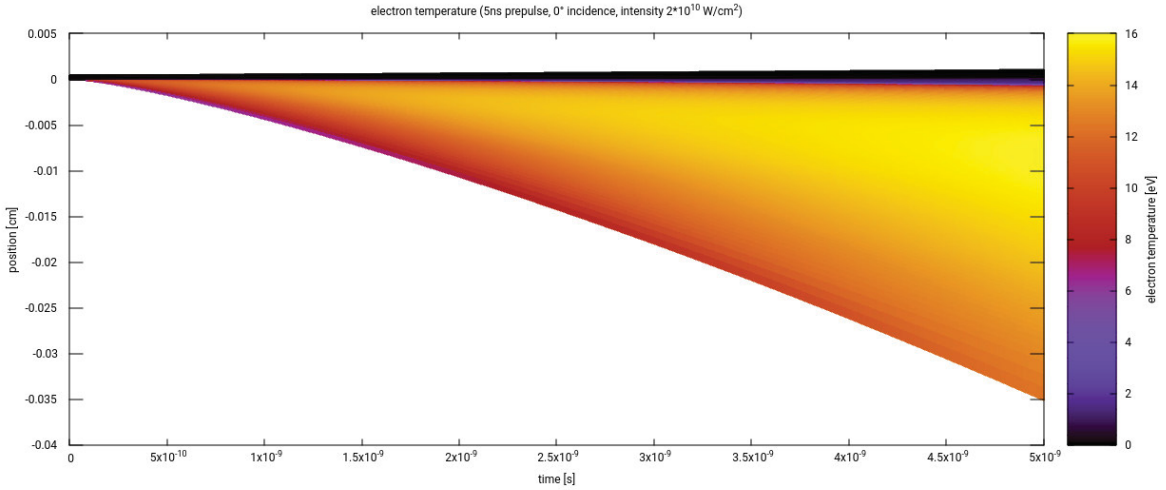


**(b)** Electron temperature during a prepulse of 5 ns duration with an intensity of $2 \cdot 10^{10}\,\mathrm{W/cm^2}$ under normal incidence on a 5 $\mu$m thick titanium target. 1D simulation with MULTI-fs. Hydrodynamic tables used for aluminium instead of titanium due to availability, ionization energies for the simulated energies are similar. Compared to the previous simulation, there is a clear increase in temperature due to the increase in intensity.

## 6.6 Evaluation of 10 ° Thomson Parabola Data

In addition to the results of the 0 ° MCP, the spectra of the 10 ° Thomson parabola were also analyzed and compared to the respective 0 ° spectra. While we were unable to detect with radiochromic films evidence of larger angular deviation of high energy protons due to magnetic vortex acceleration which had been discussed as a possibly mechanism previously [11], interesting results were obtained by investigating the ion signal under 10 °.

Most of the shots have only very little energy or there are no ions at all in the 10 ° MCP traces. Only 74 out of 635 shots on the three analyzed days have a cutoff energy of at least approaching 0.2 MeV/nucleon ($\approx$ 2.4 MeV). Out of these 74 shots there were 12 where there appear to be peak-like features in the spectra. Figures 6.33 and 6.35 are particularly striking examples, the respective spectra can be found in figures 6.34 and 6.36. This is in strong contrast to the evaluation of the 0 ° Thomson parabola data, in which no such features turned up (see section 6.3).

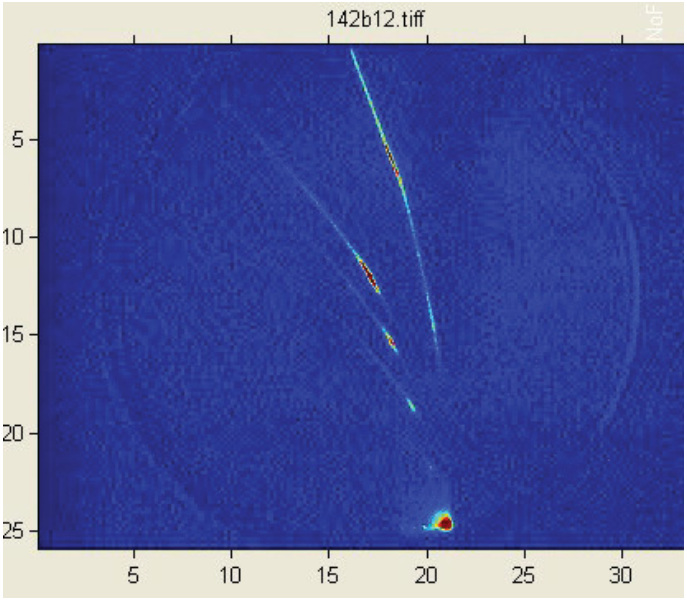


**Figure 6.33** – Contrast enhanced image of peak features in several carbon lines (C1+, C2+,C3+,C4+), strongest in C4+. The long line to the right is the proton trace. Higher energies can be found closer to the bright zero point area near the bottom of the image. For this shot, beam 1 arrived on target 5 ps after beam 2. Shot conditions: $I_{B2} = 3 \cdot 10^{18}\,\mathrm{W/cm^2}$ (defocused) and $I_{B1} = 10^{19}\,\mathrm{W/cm^2}$.

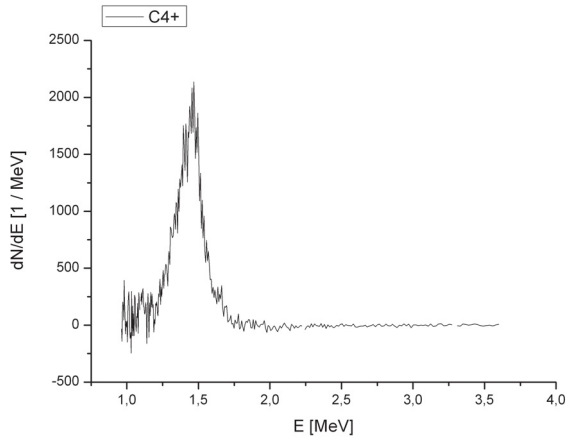


**Figure 6.34** – Spectrum of C4+ signal on the 10 degree Thomson parabola for the shot shown in fig. 6.33. There is a strong peak at 1.5 MeV with an FWHM of 0.15 MeV or 10 % of the energy with the maximum particle number. Shot conditions: Beam 1 had 840 mJ on target at an intensity of $10^{19}$ W/cm$^2$, while beam 2 had 760 mJ on target with an intensity of $3 \cdot 10^{18}$ W/cm$^2$.

In most cases the peaks are located at energies of 2 MeV or less. The majority are located at 1.5 MeV or 1.6 MeV (see figure 6.38). There is one peak feature at 3 MeV for C4+ in one shot (shot No 110 on 6th of October (200 ps delay), conditions: $I_{B2} = 3{\cdot}10^{18}$ W/cm$^2$ (defocused) and $I_{B1} = 6{\cdot}10^{18}$ W/cm$^2$) and a kind of small double feature at 9 and 10 MeV for C5+ in the previous shot (shot No 109 on 6th of October (200 ps delay), conditions as before). The latter one is also one of only two shots where there were any distinguishable peak features in the 10 degree Thomson parabola data for C5+, with the other located at 1.5 MeV at a delay of 15 ps.

Concerning the "peak shots", there is no correlation or apparent trend in the 0 ° MCP spectra of these shots. They are indistinguishable from shots where no ion peaks occurred in the 10 ° signal. There was also no specific delay where these peaks were preferably found. Such "peak-like" shots exist for delays of −5 ps (B1 first) and 5 ps (B2 first), 15 ps, 35 ps, 45 ps as well as 200 ps (see figure 6.37). For all delays where peaks occurred, there were other shots without peaks. Delay and peak ion energy appear to be independent (see figure 6.39).

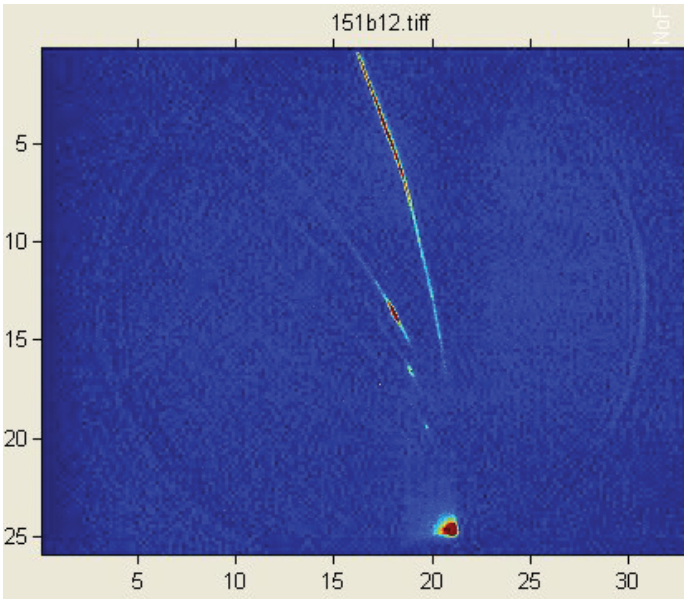


**Figure 6.35** – Contrast enhanced image of peak features in several carbon lines (C2+, C3+, C4+), strongest in C4+. The long line to the right is the proton trace. Higher energies can be found closer to the bright zero point area near the bottom of the image. For this shot, beam 1 arrived on target 5 ps before beam 2. Shot conditions: $I_{B2} = 3 \cdot 10^{18}\,\mathrm{W/cm^2}$ (defocused) and $I_{B1} = 10^{19}\,\mathrm{W/cm^2}$.

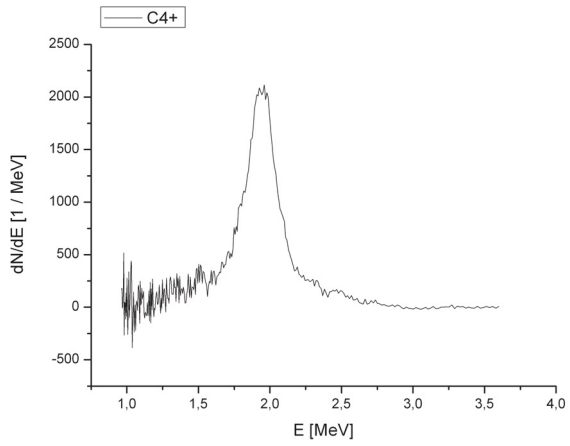


**Figure 6.36** – Spectrum of C4+ signal on the 10 degree Thomson parabola for the shot shown in fig. 6.35. There is a strong peak at 1.9 MeV with an FWHM of 0.26 MeV or 14 % of the energy with the maximum particle number. Shot conditions: Beam 1 had 840 mJ on target at an intensity of $10^{19}\,\mathrm{W/cm^2}$, while beam 2 had 760 mJ on target with an intensity of $3 \cdot 10^{18}\,\mathrm{W/cm^2}$.

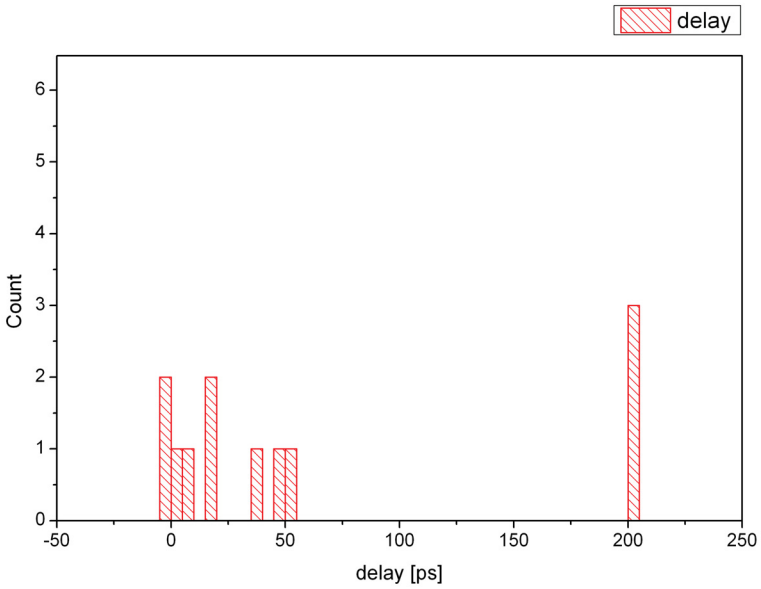


**Figure 6.37** – Histogram showing the delay settings for which peaks were found for carbon ions on 12 shots.

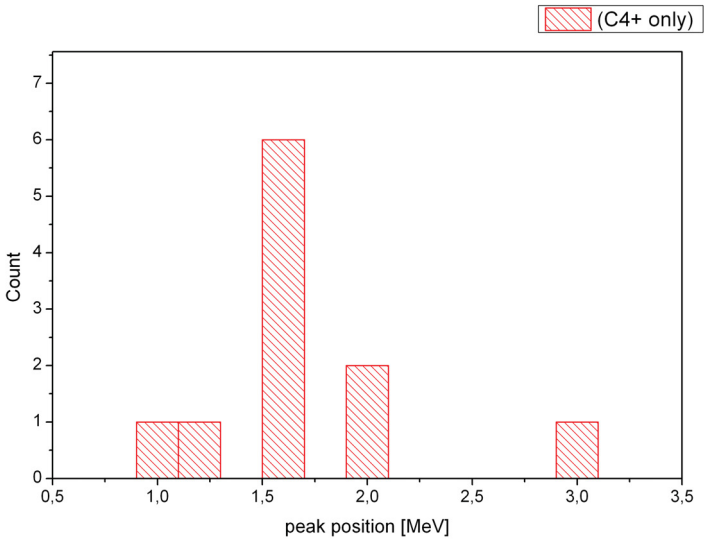


**Figure 6.38** – Histogram of ion energies at which peaks occurred in the C4+ 10 ° spectra. The majority of C4+ peaks (6 out of 11) is found in the energy range of 1.5 MeV to 1.6 MeV.

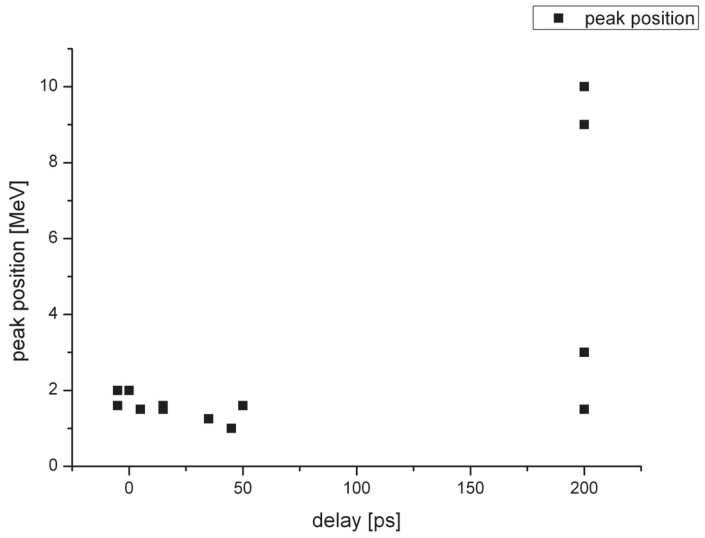


**Figure 6.39** – Delay vs energy of peaks for C4+ and C5+ ions on the 10 degree Thomson parabola. Overall there were 14 peaks in 12 shots. The data point at 15 ps and 1.5 MeV represents a C4+ and a C5+ peak at the same shot. There is no apparent correlation, the delay at which the peak occurs and the ion energy of the peak are independent of each other.

In all shots with peak-like features, they seem to occur with several ion species at the same time, although sometimes some peak features appear much brighter than others. The energies at which these peaks occur are often, but not in all cases, similar or even identical across different ionization stages.

In the analysis of the protons from the same campaign, there were also spectral features found, which clearly deviated from a TNSA like spectrum and which will be discussed in Marco Swantusch's thesis.

In evaluating the 10 ° Thomson parabola spectra, several ion spectra with a peak-like structure were found as described in section 6.6, but without any apparent dependence on the delay between both beams (see figure 6.39). Prime candidates to explain such monoenergetic features are radiation pressure acceleration [99] as well as collisionless shock acceleration [100]. Given that the target area remains overdense for all delays as discussed previously, radiation pressure is excluded as a possible explanation for the features seen in the experiment. In the following we shall discuss the model of a collisionless shock to explain the observations and make an assessment of the plausibility of such an approach.

### 6.6.1 Collisionless Shock Approach

There are two models of collisionless shock waves in plasma which could conceivably explain quasi-monoenergetic structures such as those observed in the experiment. One is by Fiuza [41] and the other by Tikhonchuk [101]. The Fiuza model simply looks at an electrostatic discontinuity between hot and dense areas and cold and less dense areas and derives the optimal conditions for it, whereas Tikhonchuk details the possibility of shocks that result from different layers of ion species which are in contact with one another. Both make predictions for the optimal conditions for the appearance of their respective type of shock wave. In the case of Fiuza, a statement on the scale length results from the calculations while in the case of Tikhonchuk there is a prediction about electron temperature given a certain peak energy.

According to Fiuza [41], the "optimal target scale length for uniform electron heating and ion reflection" is

$$L_{g0} \approx \frac{\lambda_0}{2}\sqrt{\frac{m_i}{m_e}} \tag{6.3}$$

where $\lambda_0$ is the central laser wavelength, and $m_i$ and $m_e$ are the ion and electron mass respectively. After inserting values for C5+ this comes out as

$$L_{g0} \approx \frac{800\,\mathrm{nm}}{2}\sqrt{12 \cdot 1836 + 1} \approx 59\,\mu\mathrm{m} \tag{6.4}$$

Using a shadowgraphy measurement by M. Swantusch as an estimate (see figure 6.40) this scale length would be expected at a delay of about 250 ps. However, in our results we did not find a dependence on the delay with regards to the peak-like structures found in the carbon signal on the 10 ° MCP. During the first interaction, the expected scale length is much lower than this as can be inferred from the measurement (fig. 6.40).

In the Tikhonchuk model [101], the acceleration results from two ion layers being in contact with one another, a heavy one and a light one. If this is to serve as an explanation in our case, the light ion species would be carbon and the heavy ion species would be titanium. This is actually plausible as we have a contamination layer containing carbon which is in contact with the underlaying titanium foil, which, in the target region, has also become ionized by the time the main interaction starts.

Thikhonchuk names two conditions for the validity of his model, namely $Z_1 n_{10} \gg Z_2 n_{20}$

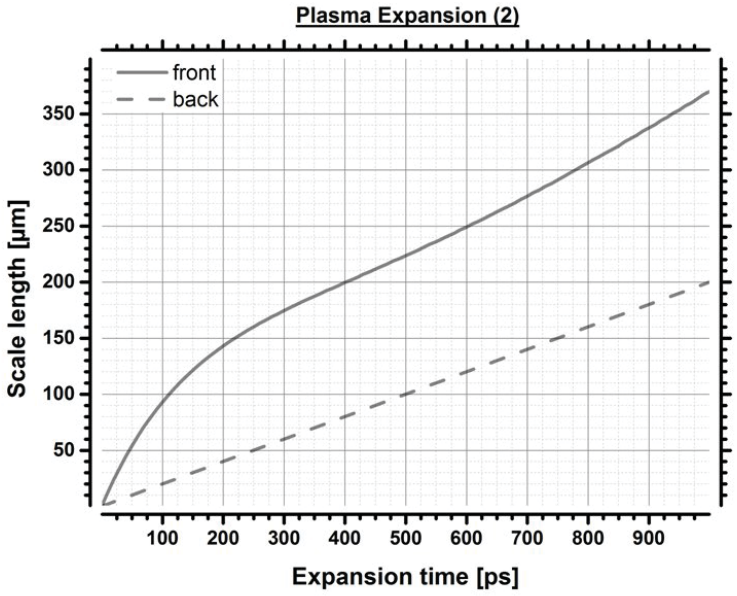


**Figure 6.40** – Scale length of an expanding 5 $\mu$m titanium target under similar conditions. Measurement and graph by Marco Swantusch.

where Z refers to the atomic number and n to the density with the subscript denoting which of the two layers are referred to, as well as $A_1 Z_2 / A_2 Z_1 \gg 1$ as a condition for the charge to mass ratio. While the charge to mass ratio condition is easily fulfilled with atomic numbers of 48 and 12 respectively (as $4 \gg 1$ and the ionization potential of titanium being lower than that of carbon), this is not as straightforward for the density condition. It is necessary to calculate the density for both layers.

The electron density of titanium is $1.25 \cdot 10^{24}\,\mathrm{cm}^{-3}$, which is approximately 720 times the critical density. The density of carbon can be derived, assuming that the contamination mostly manifests itself in the form of saturated fatty acids resulting from contact with human skin. The chemical formulae for saturated fatty acids are in the form of $CH_3(CH_2)_x COOH$. Out of the fatty acids found on the skin surface more than 99 % have carbon chains with x in the range of $14 < x < 18$ [102]. If we set x=16 and take into account that the density of typical fats are found to be about $0.9\,\mathrm{g/cm}^3$ [103] this allows us to estimate the density of carbon in the contamination layer as $\rho_c = 0.69\,\mathrm{g/cm}^3$. From this follows an electron density of $2 \cdot 10^{23}\,\mathrm{cm}^{-3}$ or approximately 120 times the critical density for the idealized carbon layer. The electron density ratio is $n_{e_{Ti}} / n_{e_C} = 6$.

Both conditions for the model are approximately fulfilled. The resulting ion speed of

the lighter ion species is as follows:

$$v_2 = \sqrt{\frac{Z_2 T_e}{A_2 m_p}} \cdot \sqrt{2\left(1 + \frac{x}{t\sqrt{\frac{Z_1 T_e}{A_1 m_p}}}\right)} \tag{6.5}$$

where the indices specify the ion species in question (one corresponding to the heavier species, two to the lighter one), $Z$ is the atomic number, $A$ is the atomic mass number, $T_e$ is the electron temperature, $t$ is time and $m_p$ is the mass of a proton. $x$ refers to the position at which one wants to know the ion speed, with $x = 0$ as the plasma-vacuum interface and positive values denoting areas in the region which is in vacuum at $t = 0$. Considering carbon ions at the very edge of the plasma, i.e. at $x = 0$, this simplifies to

$$v_2 = \sqrt{\frac{Z_2 T_e}{A_2 m_p}} \tag{6.6}$$

Transforming this equation in order to determine the electron temperature results in

$$T_e = \frac{1}{2}\frac{A_2 m_p v_2^2}{Z_2} \tag{6.7}$$

Using $v_2 = \sqrt{\frac{2E_{kin}}{A_2 m_p}}$ results in the much more simplified formula:

$$T_e = \frac{E_{kin}}{Z_2} \tag{6.8}$$

Given that the majority of quasi-monoenergetic peaks were found at an energy of about 1.6 MeV (see figure 6.38) and that carbon's atomic number is $Z = 6$ , this leads to a predicted electron temperature of 267 keV. Given that most of the border layer between titanium and carbon does not consist of hot electrons which are just temporarily passing through this region, this has to be interpreted as the cold electron temperature. This, however, is much higher than one would expect.

In literature, cold electron temperatures in comparable circumstances are usually assumed to be in the low keV range. For example, in one measurement using the ARCTURUS laser system, the cold electron temperature of a roughly comparable solid target was inferred by Brauckmann [104] from x-ray spectra as being in the range of 1.5 keV to 1.9 keV. Antici et al [105] measured by means of interferometry the electron temperature in a different experiment and found a cold electron temperature of 9 eV

with a hot electron temperature of 650 keV. If we were to assume a similar ratio of hot to cold electron temperature (due to similar heating processes occurring), using the previous estimate of a hot electron temperature of $T_{hot} = 1.15\,\mathrm{MeV}$ for our case one would expect a cold electron temperature well below 1 keV, i.e. several orders of magnitude below our target value. While the temperature ratio of hot to cold electron temperatures in Antici's results is uncharacteristically high ($\approx 70000$), even the assumption of a ratio of just 10:1 of hot to cold electron temperature as assessed by Eliezer [106] would not be sufficient to explain such a high cold electron temperature as theory requires of our case (i.e. 267 keV) if the shock explanation according to Tikhonchuk's model is to apply. Incidentally, in the same book, its author also makes the following observation on the expected order of magnitude for the cold electron temperature: "[The cold electron temperature] can be on the order of $k_B T_C = 1\,\mathrm{keV}$" [106].

If there was a specific two beam effect at play to explain such a low ratio of hot to cold electron temperature ($\approx 4$) as well as such a high value of the cold electron temperature, i.e. two orders of magnitude higher than what Eliezer describes as typical, it would probably have to relate to an increased energy absorption as this affects the heating of the bulk as well as the hot electrons. This should imply a dependence on the delay similar to the one found in the ion cutoff energy analysis. However, as discussed in this section, contrary to such a scenario there appears to be no dependence of the appearance by 10 ° peaks on the delay between both beams (see figure 6.39).

The required value for $T_C$ is therefore unrealistically high and hence casts doubt on this type of explanation based on the two models discussed.

Given that both attempts to use collisionless shocks as an explanation for the measured quasi-monoenergetic peaks appear to have failed, one has to look for alternative explanations. One such candidate might be beam filamentation and refraction in combination with locally advantageous conditions for the Fiuza or Tikhonchuk model.

To summarize, at this time there is no satisfactory, conclusive explanation for the quasi-monoenergetic peaks which were observed repeatedly in the carbon signal at an angle of 10 ° to the target normal. However, these peaks unambiguously demonstrate that while target normal sheath acceleration may be the dominant acceleration process, it clearly is not the only one taking place as such peaks are inconsistent with it.

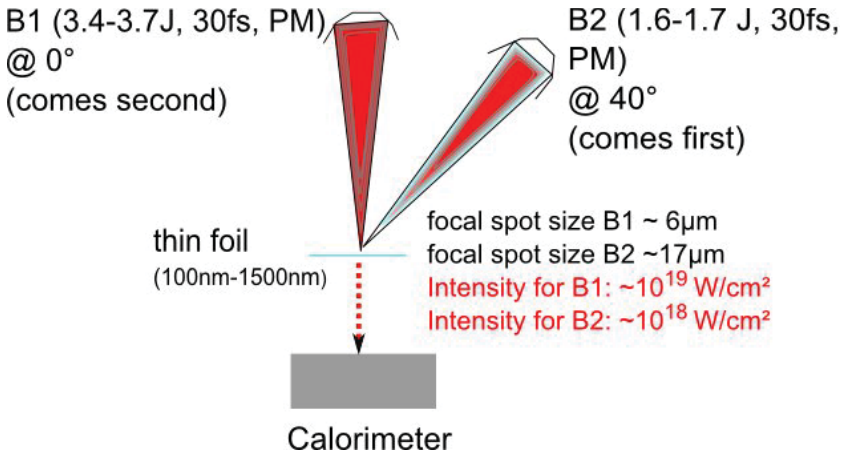


**Figure 6.41** – Experimental setup for the measurement of beam 1 transmission through thin foils with varying delays between the beams.

## 6.7 Transparency Measurements with Thin Foils

In this part of the double beam experiments, we placed a calorimeter behind the target along the 0 ° axis, so as to measure the transparency of the foil depending on the delay between both beams. For the 5 $\mu$m titanium foil used in the previous part of the experiment we did not find a delay at which the foil had become transparent, therefore it can be concluded that the titanium foil remains overdense even 3 ns after the first interaction. Given that by the end of the process there is a hole in the foil, transparency is bound to happen at some point in time later than 3 ns.

For thin foils (ranging from 100 nm DLC foils to 1500 nm thick aluminum foils) the transparency first increased with larger delay until 50 ps where it peaked and then went down again (see figure 6.42). Depending on the foil, it later increased once more.

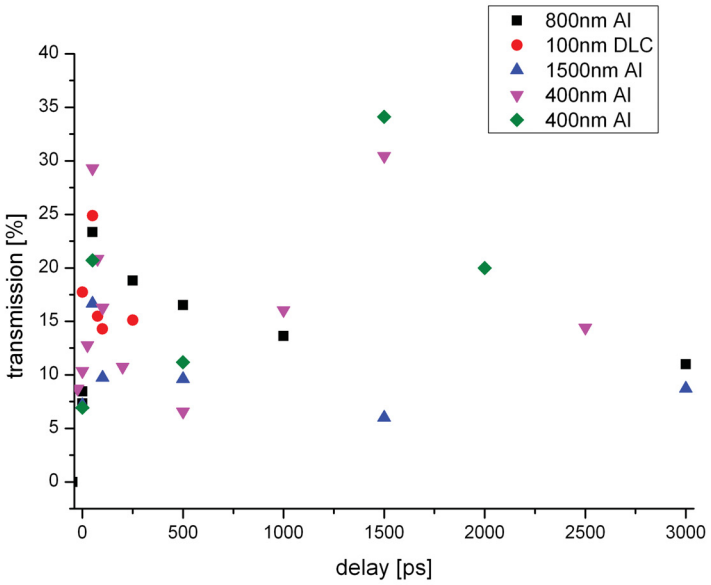


**Figure 6.42** – Transmission measurement of energy on calorimeter, data points for foils of different thicknesses. The 100 nm foil was made of diamond-like carbon, the other targets were made of aluminum. Beam 2, which came first, had an energy of $1.7\,\mathrm{J} \pm 0.1\,\mathrm{J}$ before compression, while beam 1 had an energy of $3.5\,\mathrm{J} \pm 0.2\,\mathrm{J}$. A local maximum of the transmission is found at a delay of 50 ps for all thicknesses. Note that the transmission does not exceed 35 %, i.e. the targets were at no time completely transparent. Not shown here are the results of two additional shot series on 100 nm foils as they showed 100 % transmission in the timed case, likely due to damaged targets.

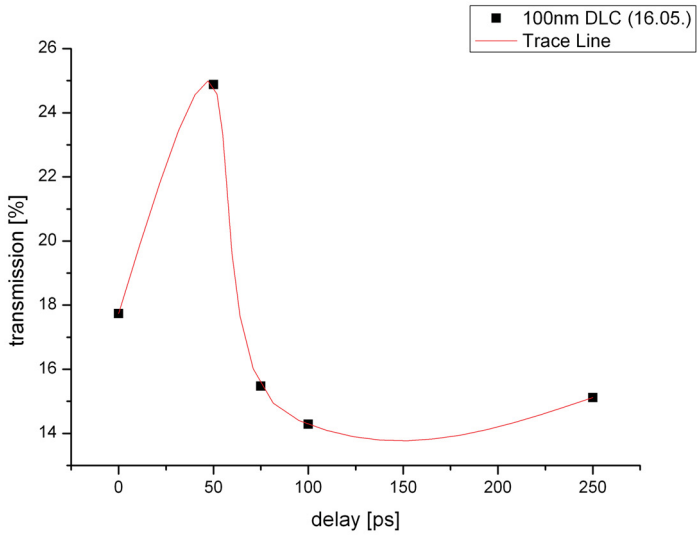


**Figure 6.43** – Transmitted energy on calorimeter, dependence on delay for a 100 nm DLC foil as measured on May 16th. B1: $3.5\,\mathrm{J} \pm 0.2\,\mathrm{J}$, B2: $1.7\,\mathrm{J} \pm 0.1\,\mathrm{J}$ Maximum transmitted energy was 840 mJ. Lines are meant to guide the eye. Measurements on the previous two days with 100 nm foils had been inconclusive and for this reason are not presented here: Several times there was a large transmission in the timed case. We suspect this might have been due to damaged targets. However, all of these measurements show a large transmission at 50 ps and all measurements which took data points for a delay of 100 ps between the beams show a clear decrease in transmission compared to the 50 ps data point. Therefore it can be argued that even the inconclusive measurements support the general observable trend.

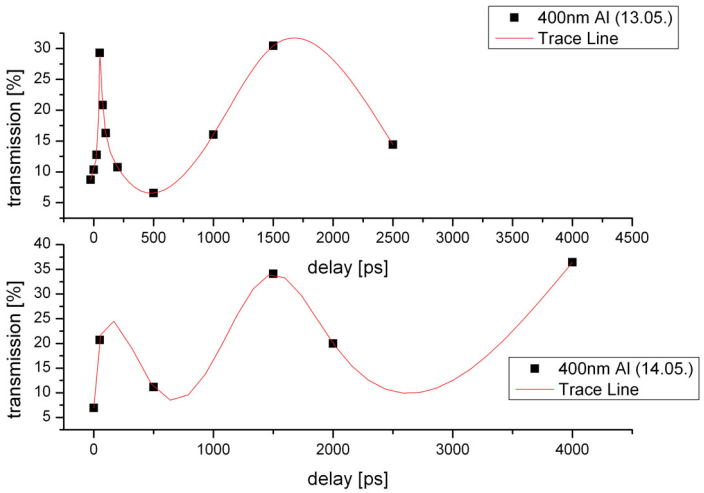


**Figure 6.44** – Transmitted energy on calorimeter, depending on delay for a 400 nm Al foil measured on 13th and 14th of May with similar conditions (B1: $3.4 - 3.6$ J, B2: $1.6 - 1.7$ J, maximum transmitted energy without target $\approx 800$ mJ) Lines are meant to guide the eye. Several peaks are apparent, with a local maximum at 50 ps and another at 1500 ps with a third possible peak at a later time in one measurement. The similarity between both measurements shows that the result is well reproduced.

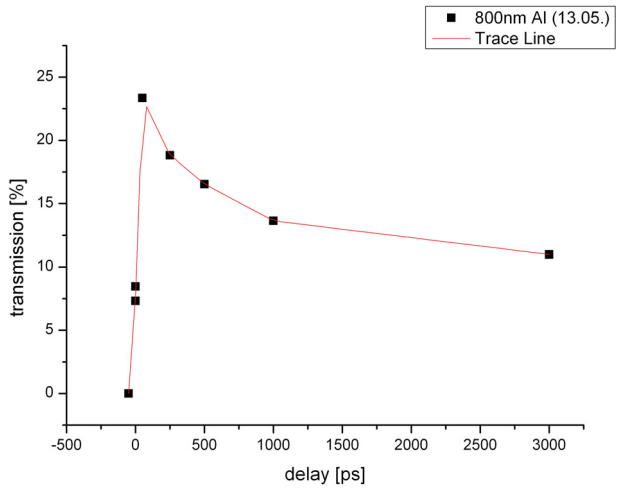


**Figure 6.45** – Transmitted energy in calorimeter, depending on delay for a 800 nm Al foil. Lines are meant to guide the eye. Experimental conditions same as before. There is only a single peak apparent at 50 ps as opposed to the oscillatory structure observed in the previous measurement (see figure 6.44).

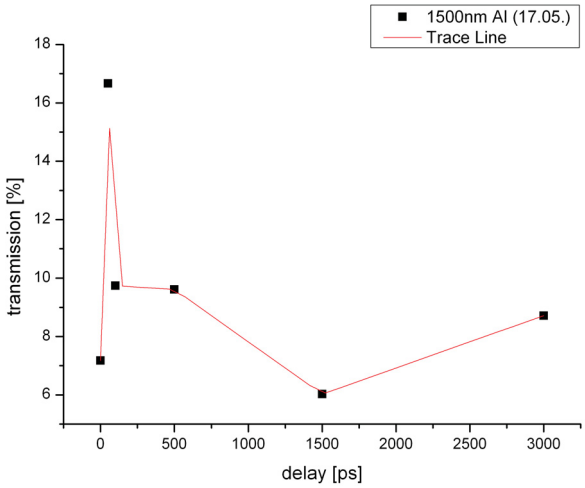


**Figure 6.46** – Transmitted energy on calorimeter, depending on delay for a 1500 nm Al foil (B1: 3.7 J, B2: 1.6 J, maximum transmitted energy without target was 780 mJ). Lines are meant to guide the eye. A peak at 50 ps is apparent and there is a hint at later variations too, although much weaker than in the 400 nm case (see figure 6.44). Another clear difference is that at a delay of 1500 ps there is less transmission than at both earlier and later times, whereas in the 400 nm case, there is a local transmission maximum at the same delay.

These results are qualitatively similar to ones reported by Aktan [107] in that a dip was also reported during transparency measurements. There it was explained due to refraction effects, leading to energy missing the calorimeter, which was also confirmed by observation of the beam at the calorimeter position. [107] In other words, the overall transmitted energy may not have actually gone down, but only the energy registered by the calorimeter. This is also plausible given that one would expect the electron density to decrease with more expansion, leading to a monotonous increase in transparency with delay. It is hard to imagine any mechanism which would cause a repeated increase in electron plasma density in absence of any outside influence after the first interaction. For this reason, it is a logical explanation for the data presented in this work as well.

## 6.8 Summary of Results for Two Beam Experiments

Two beam experiments were performed, investigating the dependency on delay between both beams on several quantities related to carbon ions.

It was found that the particle number decreases in the two beam case compared to the single beam case. While the number does depend on the delay, the fact of the decrease compared to the single beam case does not. This was explained by the combined effect of the two prepulses, which create a different preplasma compared to the single beam case with a single prepulse. Due to the increased temperature of the preplasma on the front side, the degree of ionization is increased and the critical surface moves further outward as the free electron density increases. The scale length also increases, although whether this increase is of consequence is debatable. The different position of the critical surface changes the interaction of the first beam with the preplasma (as there is a reduced intensity at the position of the critical surface) and it is hypothesized that the first interaction becomes less effective, thereby leading to a smaller number of particles arriving on the 0 ° MCP.

There is no clear deviation found in the shape of the 0 ° ion spectra from what one would expect in a TNSA interaction.

There is a clear increase in the cutoff energy in the two beam case compared to the single beam case. The increased cutoff energy normalized to the single beam case ("gain") depends on the delay and the optimum gain is found at a delay $\Delta t \neq 0$, ie not in the timed case. This was explained by advantageous conditions for resonance absorption during the second interaction for the case of the optimal delays. It is hypothesized that an increased absorption, ie energy transfer from laser to plasma, indirectly causes an increased cutoff energy.

Furthermore, the maximum gain, as defined by the highest ratio of cutoff energies between double beam and single beam case over all delays, increases with the charge state. For a pure TNSA interaction, this is not expected, as all charge state dependent effects should cancel out.

Investigating the ion data from the 10 ° Thomson parabola, most shots show hardly any or weak ion traces. However, some spectra exhibit clear peaks with an FWHM on the order of 10 % which strongly deviates from what one would expect of a pure TNSA interaction. They only occur for shots with both beams. More than half of these peaks are in the energy range of $1.5 - 1.6\,\mathrm{MeV}$. There does not appear to be any dependence on the delay. While collisionless shocks are a logical approach, given that RPA is impossible due to the target's intransparency, approximative calculations appear to demand bulk electron temperatures that are much higher than what can reasonably be assumed. Given that there is no preferred delay, relativistic self focusing or filamentation might cause locally advantageous conditions for the creation of such

shocks and serve as an explanation for the peaks.

### 6.8.1 Main Conclusions

The 0 ° spectra indicate that Target Normal Sheath Acceleration is an important process in the two beam interaction. The existence of peaks in the 10 ° spectra as well as the charge state dependent behaviour of the gain clearly show that TNSA is not the only process taking place.

Efficient resonance absorption due to the increased scale length because of the plasma expansion after the first interaction may explain the dependence of the gain on delay.

The combined prepulses can account for the reduced ion numbers in the two beam case. This effect suggests that the first interaction is already different in the two beam case compared to the single beam case.

The apparent independence of the 10 ° peaks from delay as well as the transparency measurements with thin foils indicate that self focusing within the extended undercritical plasma in front of the target has an important role to play as well.

# Chapter 7

# Outlook

This work presented a dose-deposition system and a dosimetric method for cell experiments with laser-accelerated protons. In addition, biological experiments which employed them were discussed. These are of interest for possible medical applications as they indicate different effects on the cell's nitroxidative stress between protons accelerated by laser-plasma interactions at ultra-high dose rates compared to conventionally accelerated protons.

Future improvements of the dosimetric system and method could include automatizing the dose evaluation process of the IPs, so that the dose may be determined immediately after scanning. An element of online dosimetry could also be introduced, e.g. with an MCP in a neighbouring port, calibrated to the cell port to allow for a real time, shot-by-shot assessment of the dose. The effects of different proton pulse lengths on biological endpoints such as nitroxidative stress of cells could be investigated too.

The second part of this work demonstrated some experimental phenomena of ion acceleration in the context of two beam interactions. Among other results it was found that there were certain delays for which an increase in maximum ion energy took place compared to the situation of simultaneous interaction of both beams. This was explained due to improved conditions for resonance absorption at certain scale lengths caused by the plasma expansion after the first interaction. The ion particle number was found to be reduced in the two beam case compared to the single beam case. An effect of the combined prepulses on the first interaction was given as an explanation, which was supported by simulation results with MULTI-fs. Quasi-monoenergetic peaks under $10^\circ$ to the target normal were also measured for some shots, indicating acceleration processes other than TNSA, possibly due to collisionless shockwaves.

If one could cause these peaks deliberately as well as understand and control the mechanism of their creation, it would constitute a big step towards a useful ion output from laser-plasma interactions for medical applications, provided the method can be scaled up to higher energies.

Experimentally, next steps could include probing the front side laser-plasma interaction in order to detect possible self-focusing and in general to pinpoint the precise conditions which cause these peaks. From a theoretical point of view, 2D PIC simulations could be interesting with the same goal in mind. However, if one were to simulate all interactions within a single, detailed simulation, this may prove challenging to perform as the time scale for the entire interaction is in the range of hundreds of picoseconds.

# Chapter 8

# Appendices

## 8.1 Code for Particle Tracer

This is a particle tracer program to determine the initial energy map for the cell port. Energies from 1 MeV to 6 MeV are simulated. The vertical angle range is determined by the edges of the magnetic plates of the second yoke. The horizontal angle range is determined by the geometry of the slit. The program is based on one written by P. Weiß, which was able to give a dispersion relation under 0° using the same Runge Kutta tracer procedure. The main additions were the angle dependence as well as the map creation. Its purpose and output is described in more detail in chapter 4. The initial energy map that was created using 100 proton energy steps, 100 horizontal angle steps as well as 100 vertical angle steps. The program is commented in German.

```
pro zellbeschusstracer2015

  COMMON share1,Bz1,Bz2,gap

;Sven Spickermann, 2015 (ursprünglich basierend auf einem Programm von Philipp Weiß)

;Masse und Ladung eines Protons in kg bzw C
m=9.109e-31*1836
q=1.602e-19
;genähertes Magnetfeld in Tesla:
B=0.85
```

```
;Radius des Zellports:
r_z=0.0075
  Btemp=read_ascii
("E:\Daten und Auswertungen und Spreadsheets etc\diplom_docs\Feld2.dat")
  Bz1=Btemp.FIELD01
  Btemp=read_ascii
("E:\Daten und Auswertungen und Spreadsheets etc\diplom_docs\Feld1.dat")
  Bz2=Btemp.FIELD01
  ;Abstand von Target zur Blende:
  blenden_abstand=0.076
  ;Durchmesser der Blende
  blenden_groesse=0.001
  ;x-Koordinate der Blende
  blenden_eingangsort_x=-0.03
  ;Hilfsvariable für später, um die Trajektorien plotten zu können:
  first=1
  ;Anzahl der Energieschritte
  nen=20
  ;Anzahl der Winkelschritte:
  n_horiz=20
  n_vert_angle=20

   ;Größe der Gap:
        gap=0.02

  liste_effektiver_breiten=dindgen(n_vert_angle,nen)
  liste_vertikaler_winkel=dindgen(n_vert_angle)




  horiz_pixelzahl=16
  vert_pixelzahl=16

  ;Hilfsvariable zum Debuggen
  geaendert=0
```

```
  minimal=dindgen(horiz_pixelzahl,vert_pixelzahl)
  minimal[*,*]=10
  maximal=dindgen(horiz_pixelzahl,vert_pixelzahl)
  maximal[*,*]=-1
  null_grad=dindgen(horiz_pixelzahl,vert_pixelzahl)
  null_grad[*,*]=-5

  minoutput="minimum=["
  maxoutput="maximum=["
  normoutput="norm=["



  ;gesamte protonenzahl bei gegebener Energie
  gesamtprotonenzahl=0
  ;minimale betrachtete Energie:
  minen=1e6
  ;maximale betrachtete Energie:
  maxen=5e6
    ;Quasi Boolean-Variable, bzw Array für verschiedene Teilbereiche
    ;des Ports um zu checken, ob ein Teilchen die Zellen trifft oder nicht:
  trifft_nicht=dindgen(3)
  REPLICATE_INPLACE, trifft_nicht, 1
  ;minimaler Winkel, der sich aus Blendenabstand und -durchmesser ergibt:

  min_vert_angle= -ATAN(0.005/(blenden_abstand+0.2+gap))
  ;maximaler Winkel, der sich aus Blendenabstand und -durchmesser ergibt:

  max_vert_angle= ATAN(0.005/(blenden_abstand+0.2+gap))

  winkeldichte= n_horiz/(max_vert_angle-min_vert_angle)
  ;Array um für jeden Energieschritt die seitliche Ablenkung und die
; Energie abzuspeichern
  output=dindgen(2,nen)
```

```
  ;Array mit den Energien in jedem Energieschritt:
  energien=dindgen(nen)
  effektiv_energien=dindgen(nen,n_vert_angle)
  effektiv_geschwindigkeiten=dindgen(nen,n_vert_angle)

  ;seitliche Ablenkung (Am Jochende) für jeden Energieschritt
  ;(bei geradem Flug, d.h. Winkel etwa gleich Null):
  yout=dindgen(nen)
  youtmm=dindgen(nen)
  gitteryout=dindgen(nen)
  ;Quasi Boolean-Array, um zu erfassen, ob man die seitliche Ablenkung im jeweiligen
  ;Energieschritt schon erfasst hat:
  yout_bestimmt=dindgen(nen)
  REPLICATE_INPLACE, yout_bestimmt, 0
  ;Hilfsmittel um zu sehen, wie oft tatsächlich eine seitliche
  ;Ablenkung erfasst wurde:
  nullgrad_counter=0

   ;Schleife über alle Energien:
    for ien=0,nen-1 do begin
    print, "Beginn Energieschleife"

    ;Bestimme aktuelle Energie:
      en= minen + (maxen-minen)*ien/(nen-1)
      ;Trage aktuelle Energie in Energieliste ein
      energien(ien)= en

 ;Schleife über alle vertikalen Winkel:
  for i_vert_angle=0,n_vert_angle-1 do begin
  print, "Beginn vertikale Winkelschleife"

    IF (n_vert_angle gt 1) THEN vert_angle= min_vert_angle +
 (max_vert_angle-min_vert_angle)*i_vert_angle/(n_vert_angle-1) ELSE vert_angle =
min_vert_angle

    min_horiz_angle= -ATAN(blenden_groesse/(2*blenden_abstand))
```

```
    max_horiz_angle= ATAN(blenden_groesse/(2*blenden_abstand))

    ;zz: Auftreffort in vertikaler Richtung
    zz=0.605*TAN(vert_angle)
    print, "zz:"
    print, zz


    ;Anzahl der horizontalen Winkelschritte beim gegebenen vertikalen Winkel
    ; (Kreis läuft nach oben und unten enger zu)
    n_horiz_angle= ROUND(winkeldichte*(max_horiz_angle-min_horiz_angle))


      effektiv_energie= en_eff(en,vert_angle)
      effektiv_energien(ien,i_vert_angle)= effektiv_energie
      effektiv_geschwindigkeit= vstartp(effektiv_energie)
      effektiv_geschwindigkeiten(ien,i_vert_angle)= effektiv_geschwindigkeit



  ;Schleife über alle Winkel:
  for i_horiz_angle=0,n_horiz_angle-1 do begin
  print, "Beginn horizontale Winkelschleife"

    IF (n_horiz_angle gt 1) THEN
horiz_angle= min_horiz_angle +
(max_horiz_angle-min_horiz_angle)*i_horiz_angle/(n_horiz_angle-1)
ELSE horiz_angle = min_horiz_angle
    print, "H1"
    ;Zusammenhang zwischen seitlichem Entrittsort(y-Koordinate) in der Blende
    ;und Flugwinkel:
    blenden_eingangsort_y=blenden_abstand*TAN(horiz_angle)
    print, "H2"

        ;wenn die Teilchen nicht weit genug kommen, dann mach x größer; ansonsten:
        ;ein Array mit der Größe der Schrittzahl in einer Trajektorie:
```

```
       x=dindgen(1500)/999*50e-9
       print, "H3"
       ;Erstelle die Trajektorie in "yp". "yp" ist ein zweidimensionaler Array;
      ;der erste Index bezeichnet die Variable (hier also x,y,vx oder vy),
      ;der zweite Index den
       ;Schritt innerhalb der Trajektorie
       yp = IMSL_ODE(x,[blenden_eingangsort_x,blenden_eingangsort_y,COS(horiz_angle)*
        effektiv_geschwindigkeit,SIN(horiz_angle)*effektiv_geschwindigkeit],
       'fp', /R_K_V,Max_Steps = 15000)
       print, "H4"

       ;es folgt die Schleife zur Feststellung des korrekten Index
       ;Variablen zur korrekten Indexfindung, um in yp den Schritt angeben zu können,
       ;wo das Teilchen auf Höhe des Zellflansches ist
links=0
mitte=0
rechts=1499
zielwert=0.605
       WHILE (mitte ne ROUND((links+rechts)/2)) DO BEGIN
         mitte=ROUND((links+rechts)/2)
         IF (zielwert gt yp(0,mitte)) THEN links=mitte
         IF (zielwert lt yp(0,mitte)) THEN rechts=mitte
         IF (zielwert eq yp(0,mitte)) THEN BEGIN
           links=mitte
           rechts=mitte
         ENDIF
       ENDWHILE

       ;Erstelle einen Array mit den x-Werten der Trajektorie. Sein Index bezeichnet
       ;den Schritt der Trajektorie.
       xtemp=reform(yp(0,*))
       print, "H5"
       ;erstelle einen Array mit den Elementen aus "xtemp", deren Betrag kleiner als
       ;0.8 ist; nach dem Motto: Diese Elemente interessieren uns besonders.
       xx=xtemp(where(abs(xtemp) lt 0.8))
       print, "H6"
```

```
 ;Erstelle einen Array mit den y-Werten der Trajektorie. Sein Index bezeichnet
 ;den Schritt der Trajektorie.
 ytemp=reform(yp(1,*))
 print, "H7"
 ;erstelle einen Array mit den Elementen aus "ytemp", die
 ;dieselben Indices haben wie die Elemente aus "xtemp",
 ; deren Betrag kleiner als 0.8 ist;
 yy=ytemp(where(abs(xtemp) lt 0.8))
 ;yarr=ytemp(where(xtemp gt 0.605))
 horiz_auftreff=yp(1,mitte)
;yymm ist horiz_auftreff in Millimetern
yymm=1000*horiz_auftreff
zzmm=1000*zz
gittery= ROUND(yymm-45)
gittery=FIX(gittery)
gitterz= ROUND(zzmm+7.5)
gitterz=FIX(gitterz)
IF ((gittery gt -0.1) and (gittery lt 15.1) and (gitterz gt -0.1) and
  (gitterz lt 15.1)) THEN BEGIN
     print, "minimal 12 6:"
     print, minimal[12,6]
     print, "maximal 12 6:"
     print, maximal[12,6]
     print, geaendert
     print, "gittery:"
     print, gittery
     print, "gitterz:"
     print, gitterz
     IF (en/(1e6) gt maximal[gittery,gitterz]) THEN BEGIN
          maximal[gittery,gitterz]=en/(1e6)
          geaendert=1
     ENDIF
     IF (en/(1e6) lt minimal[gittery,gitterz]) THEN BEGIN
          minimal[gittery,gitterz]=en/(1e6)
          geaendert=1
     ENDIF
```

```
ENDIF

 print, "H8"


 ;Beginn Ermittlung yout

 ;"y_trajektorie_jochausgang" ist ein Array mit den y-Koordinaten bei
 ;den Schritten der Trajektorie, die zwischen Ende des Doppeljochs und
 ;dem Punkt 5cm davon entfernt liegen
 ;y_trajektorie_jochausgang= ytemp(where((xtemp gt (0.2+gap)) and
 ;(xtemp lt (0.21+gap))))
 links=0
 mittejochende=0
 rechts=1499
 zielwert=0.2+gap
 WHILE (mittejochende ne ROUND((links+rechts)/2)) DO BEGIN
   mittejochende=ROUND((links+rechts)/2)
   IF (zielwert gt yp(0,mittejochende)) THEN links=mittejochende
   IF (zielwert lt yp(0,mittejochende)) THEN rechts=mittejochende
   IF (zielwert eq yp(0,mittejochende)) THEN BEGIN
     links=mittejochende
     rechts=mittejochende
   ENDIF
 ENDWHILE



 print, "Z7"
 ;Für ein gerade fliegendes Teilchen wollen wir die seitliche Ablenkung
 ;am Jochausgang haben

 ;Wenn der Winkel größer Null ist (er fängt negativ an und überschreitet
 ;irgendwann die Null), dann erfasse die seitliche Ablenkung für diese Energie
 ;(falls Du es noch nicht getan hast) und markiere hinterher,
 ;dass Du es getan hast
```

```
; damit es pro Energie nur einmal geschieht
IF (((vert_angle gt 0) or (vert_angle eq 0)) and ((horiz_angle gt 0) or
       (horiz_angle eq 0)) and (yout_bestimmt(ien) eq 0)) THEN BEGIN
;Erfassung der seitlichen Ablenkung (in Abhängigkeit
;vom Energieschritt) in "yout", indem dort der Wert geschrieben wird,
;der im ersten Element von "y_trajektorie_jochausgang" steht:
print, "Z8"
yout[ien]= yp(1,mittejochende)
youtmm[ien]=1000*yout[ien]
gitteryout[ien]=ROUND(youtmm[ien]-45)
print, "Z9"
yout_bestimmt(ien)=1
print, "Z10"
nullgrad_counter=nullgrad_counter+1
print, "Z11"
ENDIF
;Ende Ermittlung yout

;Text-Ausgabe der Trajektorien (nicht zur Zeit):
print, "Z12"
;xel=n_elements(xx(where(abs(xx) lt 0.7+gap)))
print, "Z13"
;Index = min(where(xtemp gt 0.125))
;print,xtemp(Index-1),xtemp(Index),ytemp(Index-1),ytemp(Index)
;nimm semikolon in vorhergehender Zeile weg, um Ausgabe zu aktivieren



;Ausgabe der Trajektorien als Plot
IF first eq 1 THEN BEGIN
print, "Z16"
  iplot,xx, yy, XRANGE = [-0.2, .8], YRANGE = [-0.05, 0.075]
  print, "Z17"
  first= 0
  print, "Z18"
ENDIF ELSE iplot,xx,yy,/overplot
```

```
        print, "Z19"

        endfor
        print, "Ende horizontale Winkelschleife"

        gesamtprotonenzahl= gesamtprotonenzahl+n_horiz_angle

     endfor
     print, "Ende vertikale Winkelschleife"

     ;schreibe die Energien und die zugehörige seitliche Ablenkung
        ;(bei ca 0°-Einfall) in "output" (verschoben in reine Energieschleife):
        print, "Z14"
        output(0,ien)=yout(ien)
        print, "Z15"
        output(1,ien)=en

       gesamtprotonenzahl=0

  endfor
  print, "Ende Energieschleife"


  ;Ausgabe der seitlichen Ablenkung in Abhängigkeit von der Energie (für ca 0°)
  ;als Plot
  iplot,output(0,*),output(1,*),XRANGE = [0, .075], YRANGE = [0, 6e6], LINESTYLE=6,
       SYM_INDEX=7, TITLE="Ablenkung je nach Energie", XTITLE= 'y/m', YTITLE= 'E/MeV'


;jetzt wird in ein 16x16 Gitter die Energie in MeV der nicht abgelenkten Teilchen
;eingetragen
for ien=0,nen-1 do begin
    print, "Beginn Energieschleife2"
    for z=0,15 do begin
       IF ((gitteryout[ien] gt -0.1) and (gitteryout[ien] lt 15.1)) THEN BEGIN
```

```
          null_grad(gitteryout[ien],z)= energien[ien]/1e6
        ENDIF
     endfor
endfor

;Ausgabe der Ergebnisse:

for y=0,15 do begin
   for z=0,15 do begin
      minoutput=minoutput+string(minimal(z,y))
      IF (z lt 15) THEN minoutput=minoutput+","
   endfor
   IF (y lt 15) THEN minoutput=minoutput+";"
endfor
minoutput=minoutput+"]"

for y=0,15 do begin
   for z=0,15 do begin
      normoutput=normoutput+string(null_grad(z,y))
      IF (z lt 15) THEN normoutput=normoutput+","
   endfor
   normoutput=normoutput+";"
endfor
normoutput=normoutput+"]"

for y=0,15 do begin
   for z=0,15 do begin
      maxoutput=maxoutput+string(maximal(z,y))
      IF (z lt 15) THEN maxoutput=maxoutput+","
   endfor
   IF (y lt 15) THEN maxoutput=maxoutput+";"
endfor
maxoutput=maxoutput+"]"

print, minoutput
print, normoutput
```

```
print, maxoutput


end

;Prozedur zur Bestimmung einer "effektiven Energie", die die korrekte Ablenkung
;in Abhängigkeit vom vertikalen Winkel bestimmt
function en_eff, energy, beta
  return, energy*cos(beta)*cos(beta)
end

;Prozedur zur Bestimmung der Anfangsgeschwindigkeit von Protonen
; in Abhängigkeit ihrer kinetischen Energie
function vstartp, ekin
  E0p=938e6
  return, 299792458.*sqrt(1-E0p*E0p/(E0p+Ekin)/(E0p+Ekin))
end

;Prozedur, die die Ableitungen der Größen x,y,vx und vy enthält,
;damit IMSL_ODE (die Tracing-Prozedur) weiss, wie sie von Schritt zu Schritt
;vorgehen muss
FUNCTION fp, t, y ; y(0)=x, y(1)=y, y(2)=v_x, y(3)=v_y
  COMMON share1
  m_p=9.109e-31*1836
  c_p=1.602e-19
  ;Angabe über das Magnetfeld und was im Bereich ohne Messdaten passieren soll
  Bzz = 1e-3 * INTERPOLATE (Bz1,y(1)/0.005+1,y(0)/0.005+5, MISSING = 0) + 1e-3 *
     INTERPOLATE (Bz2,y(1)/0.005+1,(y(0)-0.1-gap)/0.005+5, MISSING = 0)
    ;Ableitung von x ist vx, Ableitung von y ist vy, Ableitung von vx ist Fx/m
    ;Ableitung von vy ist Fy/m, nach Einsetzen der Lorentzkraft ergibt sich:
    RETURN, [y(2),y(3),c_p/m_p*Bzz*y(3),-c_p/m_p*Bzz*y(2)]
END
```

## 8.2 Code for IP Dose Evaluation

This is the program that was used to get the dose (in arbitrary units) from the Imaging Plate scans. This version puts out only the (uncalibrated) dose output, i.e. the dose in mGy divided by calibration factor k (grey value → PSL) for the cell port on a 16x16 grid. If one multiplies it with the calibration factor given in the Ingenito paper[86], one gets the actual (calibrated) dose map, showing the local dose for each position (neglecting the slight deviation from proportionality due to the offset in Ingenito's formula as discussed in chapter 5).

Older versions were used to create the data used for the graphics in chapter 5 and to move from pixel values on the x-axis to position in mm and from there to energy. The program is based loosely on one by A. Mick, which gave a spectrum of the sum of grey values along a column vs the position of that column in pixel for areas that are filtered by a mask. This is very similar to the first steps by the program included here, everything else is original work by this author. The program is commented in German.

```
;Sven Spickermann, 2017 (ursprünglich basierend auf einem Programm von
; Alexander Mick)

;diese Funktion dient dazu bei Eingabe eines Energiewerts in keV den zugehörigen
;Kalibrierfaktor auszugeben
;(in PSL/#p), basierend auf Mancic et al, Review of Scientific Instruments, 2008.

FUNCTION CALIB, fl
IF (fl LT 2110) THEN RETURN, 0.22039*EXP(-(fl/1000.0 - 1.5049)^2/(1.1842)^2)
      ELSE RETURN,  0.33357*(fl/1000.0)^(-0.91377)
END

;Das Programm dient der Dosisermittlung und benutzt die oben definierte function.

path_in='E:\Daten und Auswertungen und Spreadsheets etc\Mediziner Kammer
        \zellexperiment_feb_13\neue_auswertung_mai_13\ergebnisse_dosimetrie
        \080213\resultsvietere_m100_nachmittags_ip\'
bild_roh=read_tiff(channels=0,path_in+'vietere_m100_nachmittags_iptilt.tif')
maske=read_tiff(channels=0,path_in+'16maskvietere_m100_nachmittags_iptilt.tif')
bild=bild_roh
```

```
OPENW, 1,path_in+ 'import_bild.txt'

printf, 1, bild
CLOSE, 1


;bild1=rot(bild,90)

untergrund=190
width=1337
height=2007
;Position des Zentrums des Zellports in x:
mittelportpos=1073
;der folgende Wert gibt die Position des Zentrums des Zellports in y an
mittelportpos_y=625
;Orientierungsfaktor: Falls die niedrigen Energien oben sind, sollte er 1 sein.
;Sind die niedrigen Energien unten auf dem IP-Bild, so ist der Faktor -1
orientierung=1

exponent_psl= INTARR(width,height)
exponent= INTARR(width,height)
;PSL-Werte für ganzes Bild:
psl= INTARR(width,height)

; Energiebereiche, die auf die IP treffen in keV,
; ermittelt aus separaten SRIM Simulationen.
; Nicht zu verwechseln mit den Energiebereichen, die auf die Zellen treffen.
; (Protonen durchqueren andere Schichten)
; Diese Energien sind deshalb wichtig, weil es für die Umwandlung
; von PSL in Protonenzahl auf die Energien ankommt,
; die auf die Image Plate treffen und nicht auf jene Energien,
; die auf die Zellen treffen.
; Vorgehen in 1mm Schritten.
; Alle Teilchen, die in den jeweiligen Streifen fallen, werden
; (was die Energien angeht) gleich behandelt,
```

```
; d.h. es wird ein einfaches Mittel über den Energiebereich gebildet.

e_anfang=[0.0,0.0,0.0,0.0,0.0,0.0,0.0,0.0,1.0,124.0,233.0,353.0,520.0,
                        624.0,759.0,845.0]
e_ende=[454.0,540.0,701.0,778.0,916.0,981.0,1111.0,1230.0,1349.0,1464.0,1626.0,
             1786.0,1916.0,2043.0,2192.0,2402.0]
n_summe=0

gesamtdosis=LONG(0)
ausgeleuchtete_rasterpunkte=0

mittlere_anzahl=LONARR(16,16)
standardabweichung=FLTARR(16,16)
deponierte_gesamtenergie=LONARR(16,16)
deponierte_e_pro_proton=INTARR(16)
deponierte_dosis=LONARR(16,16)
pixelzahl=FLTARR(16,16)
summe_rasterpunkt=LONARR(16,16)
zugehoeriger_streifen=INTARR(16,16)


; Das Folgende ergibt sich aus SRIM Simulationen, siehe Kapitel 4
; (map of deposited energy per proton depending on position)
; Dies sind die deponierten Energien im Zelllayer pro Proton in keV

deponierte_e_pro_proton=[0,0,36,89,136,143,140,140,136,132,127,122,121,122,118,108]



OpenW, 2, path_in+ 'dosis.txt'

for i=0,15 Do Begin
  for j=0,15 Do Begin
    mittlere_anzahl(i,j)=0
    standardabweichung(i,j)=0
    pixelzahl(i,j)=0
```

```
    summe_rasterpunkt(i,j)=0
  endfor
endfor

for x=0,width-1 Do Begin
    for y=0,height-1 Do Begin
    if (maske(x,y) EQ 0) Then Begin
       ;wir interessieren uns nur für die Zellports, mache Rest von Bild schwarz
       bild(x,y)=0
       endif

    ;nach Auskunft der Herstellerfirma sind die ausgegebenen Grauwerte linear zu PSL
    ;weil die Umwandlung scannerintern geschieht.  Deshalb gibt es
    ;hier keine exponentielle Umwandlung,
    ;nur einen (zur Zeit (des Schreibens dieses Programms) unbekannten)
    ;Proportionalitätsfaktor. Siehe Ingenito et al, Plasma Physics by
    ;Laser and Applications, ENEA, 2015 für den Faktor

; Bei vielen anderen Scannern gibt es stattdessen einen exponentiellen Zusammenhang
; zwischen PSL und Grauwerten. Siehe auch: Paterson et al, 2008, S.3.
; In diesem Fall müsste dies zwingend an dieser Stelle umgewandelt werden,
; da Linearität nicht mehr gegeben ist und es auch
; näherungsweise nicht mehr als proportional angenommen werden darf.

; Beispiel für R=50, G=65535 (da Pixelgröße 50μm und Bild 16bit):
; exponent_psl(x,y)=FLOAT(5*(FLOAT(bild(x,y))/65535.0-0.5))
; psl(x,y)=0.25*FLOAT(10^exponent_psl(x,y))

    psl(x,y)=bild(x,y)

    endfor
endfor

;PSL Werte nach Position:
verteilung=long64(bindgen(height))
;Array für normalisierte Pixelpositionen:
```

```
pixelposition=long64(bindgen(height))
;Analog für y:
pixelposition_y=long64(bindgen(height))
; Array für normalisierte Pixelposition in mm:
posinmm=float(bindgen(height))
;Analog für y:
posinmm_y=float(bindgen(height))
;Array, der sowohl normalisierte Pixelposition als auch PSL-Summe enthält:
posvssumme=float(bindgen(2,height))
;Array, der sowohl normalisierte Pixelposition in mm als auch PSL-Summe enthält:
posinmmvssumme=float(bindgen(2,height))
;Array mit Ort vs Protonenzahl:
anzahl=long64(bindgen(height))

for u=0,height-1 Do Begin
       ;normalisiere Position bezogen auf Mitte des Zellports (Mittelport)
       pixelposition(u)=orientierung*(mittelportpos-u)
       verteilung(u)=0
       ;summiere mit nächster Schleife alle PSL-Werte in einer Spalte auf
       ;(width und height sind anders als man denkt, weil Bild gedreht ist).
       posvssumme(0,u)=pixelposition(u)
       posvssumme(1,u)=verteilung(u)
       ;50μm entsprechen 1px:
       posinmm(u)= 0.05*pixelposition(u)
       posinmmvssumme(0,u)=posinmm(u)
       posinmmvssumme(1,u)=verteilung(u)
       for v=0,width-1 Do Begin
          pixelposition_y(v)=orientierung*(v-mittelportpos_y)
          posinmm_y(v)=0.05*pixelposition_y(v)
          if (maske(v,u) NE 0) Then Begin
          If (posinmm(u) gt (-7.5)) and (posinmm(u) lt 7.5)
            and (posinmm_y(v) gt (-7.5))
            and (posinmm_y(v) lt 7.5) Then Begin
                index1=ROUND(posinmm(u)+7.5)
                index2=ROUND(posinmm_y(v)+7.5)
                ;PRINTF, 2, 'aktueller Index: ', index1,index2
```

```
                ;falls innerhalb des Zellports: in welchem Streifen sind wir?
                zugehoeriger_streifen(index1,index2)=15-ROUND(posinmm(u)+7.5)
                summe_rasterpunkt(index1,index2)=
                     summe_rasterpunkt(index1,index2)+psl(v,u)
                pixelzahl(index1,index2)=pixelzahl(index1,index2)+1
            Endif
           ;verteilung(u)=LONG64(verteilung(u))+LONG64(psl(v,u))
           ;verteilung(u)=LONG64(verteilung(u))-LONG64(untergrund)
         endif
       endfor
endfor

PRINTF, 2, 'Erste Koordinate: links/rechts, Zweite Koordinate:oben/unten.'
PRINTF, 2, 'Bei Ansicht von außen auf Zellport heisst kleine erste Zahl links und
        kleine zweite Zahl oben.'
PRINTF, 2, ' '

for i=0,15 Do Begin
  for j=0,15 Do Begin
    ;PRINT, 'Indices und summe_rasterpunkt am Anfang der for-Schleife: ',
    ;       i,j,summe_rasterpunkt(i,j)
    ;PRINT, ' '
    streifen_in_port=zugehoeriger_streifen(i,j)
    delta_e=e_ende(streifen_in_port)-e_anfang(streifen_in_port)
    for energieschritt=0, ROUND(delta_e/10) Do Begin
          ;bestimme für jeden Energiewert, welche Teilchenzahl dem PSL-Signal
          ;entsprechen würde.
          ;man muss durch den Kalibrierwert teilen, da er PSL/Protonenzahl angibt
          n_summe= long64(n_summe+long64(summe_rasterpunkt(i,j)/
                      CALIB(e_anfang(streifen_in_port)+energieschritt*10)))
    endfor
    ;es ist eine Anzahl, also behandele es als Integer
    n_summe=ROUND(n_summe)
    ;mittlere es über den Energiebereich und schreibe die Protonenanzahl
    ;für diesen Pixel in Ergebnisarray
    n_summe=ROUND(n_summe/ROUND((delta_e/10)+1))
```

```
    summe_rasterpunkt(i,j)=n_summe

    if (pixelzahl(i,j) eq 0) then begin
      mittlere_anzahl(i,j)=0
    endif else begin
      mittlere_anzahl(i,j)=summe_rasterpunkt(i,j)/pixelzahl(i,j)
    endelse
    deponierte_gesamtenergie(i,j)=mittlere_anzahl(i,j)*deponierte_e_pro_proton(i)
    ;in den Faktor in der nächsten Zeile geht Flächengröße eines Pixels,
     ;Dichte und Schichtdicke ein, um die Masse zu bestimmen
    ;innerhalb derer die Energie deponiert wird.
     ;Wenn sich diese Parameter ändern, ändert sich auch der Faktor
    deponierte_dosis(i,j)=ROUND(0.012816*deponierte_gesamtenergie(i,j))
    if (not(pixelzahl(i,j) eq 0)) then begin
      gesamtdosis=gesamtdosis+deponierte_dosis(i,j)
      ausgeleuchtete_rasterpunkte=ausgeleuchtete_rasterpunkte+1
    endif
    PRINTF, 2, i,j,' : ',mittlere_anzahl(i,j),' deponierte Energie: ',
             deponierte_gesamtenergie(i,j),'keV
    PRINTF, 2, 'lokale Dosis: ', deponierte_dosis(i,j),'mGy'
    ;, ' ',summe_rasterpunkt(i,j), ' ',pixelzahl(i,j)
    PRINTF, 2, ' '
    n_summe=0
  endfor

endfor
gesamtdosis=gesamtdosis/LONG(ausgeleuchtete_rasterpunkte)
PRINTF, 2, 'Gesamtdosis für ausgeleuchteten Bereich: ', gesamtdosis, 'mGy'
PRINTF, 2, 'muss allerdings noch mit scannerabhängigem Proportionalitätsfaktor
         (Grauwert->PSL) korrigiert werden.'

Close, 2

;plot,posinmm,verteilung
;write_bmp,path_in+'verteilung_test_mm.bmp',TVRD()
```

```
;nächste Zeilen plotten Protonenzahl/50µm Streifen
;plot,posinmm,anzahl,XRANGE=[-7.5,7.5]
;write_bmp,path_in+'anzahlverteilung_test.bmp',TVRD()

;Verteilung in Vektor umwandeln
;verteilung_vektor=long(bindgen(1,height))
 ;   for i=0,height-1 Do Begin
  ;  verteilung_vektor(0,i)=verteilung(i,0)
   ; endfor

;plotten der Kalibrierfunktion
;(zur Prüfung, ob es Kurve aus Mancic-Paper reproduziert).
;x-Achse in E/100keV, y-Achse in PSL/#p
kalibrierfunktion=FLTARR(200)
For i=0,199 Do Begin
kalibrierfunktion(i)=CALIB(100*i)
endfor
plot,XRANGE=[0,199],kalibrierfunktion


;nächste drei Zeilen für Erstellen des Spektrums

;OPENW, 1,path_in+'verteilung_test_mm.txt'

;printf, 1,posvssumme
;CLOSE, 1

;nächste drei Zeilen für Erstellen der PSL-Datei (als .txt)
;OPENW, 1,path_in+ 'resultsvietere_m100_nachmittags_ip\psl_spektrum.txt'

;printf, 1, psl
;CLOSE, 1

end
```

# Bibliography


[1] S. Bulanov and V. Khoroshkov, "Feasibility of using laser ion accelerators in proton therapy," *Plasma Physics Reports*, vol. 28, pp. 453–456, 2002.

[2] T. Tajima, D. Habs, and X. Yan, "Laser acceleration of ions for radiation therapy," *Reviews of Accelerator Science and Technology*, vol. 2, pp. 201–228, 2009.

[3] A. Yogo, K. Sato, M. Nishikino, M. Mori, T. Teshima, H. Numasaki, M. Murakami, Y. Demizu, S. Akagi, S. Nagayama, K. Ogura, A. Sagisaka, S. Orimo, M. Nishiuchi, A. S. Pirozhkov, M. Ikegami, M. Tampo, H. Sakaki, M. Suzuki, I. Daito, Y. Oishi, H. Sugiyama, H. Kiriyama, H. Okada, S. Kanazawa, S. Kondo, T. Shimomura, Y. Nakai, M. Tanoue, H. Sasao, D. Wakai, P. R. Bolton, and H. Daido, "Application of laser-accelerated protons to the demonstration of dna double-strand breaks in human cancer cells," *Applied Physics Letters*, vol. 94, pp. 181502–1 – 181502–3, 2009.

[4] S. D. Kraft, C. Richter, K. Zeil, M. Baumann, E. Beyreuther, S. Bock, M. Bussmann, T. E. Cowan, Y. Dammene, W. Enghardt, U. Helbig, L. Karsch, T. Kluge, L. Laschinsky, E. Lessmann, J. Metzkes, D. Naumburger, R. Sauerbrey, M. Schürer, M. Sobiella, J. Woithe, U. Schramm, and J. Pawelke, "Dose-dependent biological damage of tumour cells by laser-accelerated proton beams," *New Journal of Physics*, vol. 12, p. 085003, 2010.

[5] T. E. Schmid, G. Dollinger, V. Hable, C. Greubel, O. Zlobinskaya, D. Michalski, M. Molls, and B. Röper, "Relative biological effectiveness of pulsed and continuous 20 mev protons for micronucleus induction in 3d human reconstructed skin tissue," *Radiotherapy and Oncology*, vol. 95, pp. 66–72, 2010.

[6] D. Doria, K. Kakolee, S. Kar, S. Litt, and F. F. et al, "Biological effectiveness on live cells of laser driven protons at dose rates exceeding 109 gy/s," *AIP Advances*, vol. 2, p. 011209, 2012.

[7] S. Raschke, S. Spickermann, T. Toncian, M. Swantusch, J. Boeker, U. Giesen, G. Iliakis, O. Will, and F. Boege, "Ultra-short laser-accelerated proton pulses have similar dna-damaging effectiveness but produce less immediate nitroxidative stress than conventional proton beams," *Scientific Reports*, vol. 6, p. 32441, 2016.

[8] D. Strickland and G. Mourou, "Compression of amplified chirped optical pulses," *Optics Communications*, vol. 55, pp. 447–449, 1985.

[9] S. Spickermann, "Entwicklung eines multischuss-target und detektorensystems für laserbeschleunigte protonen," Master's thesis, Heinrich Heine Universität Düsseldorf, 2011.

[10] P. Weiß, "Aufbau einer experimentierkammer für medizinische anwendungen von laserbeschleunigten protonen," Master's thesis, Heinrich Heine Universität Düsseldorf, 2011.

[11] J. Böker, *Laser-Driven Proton Acceleration with Two Ultrashort Laser Pulses.* PhD thesis, Universität Düsseldorf, 2015.

[12] F. F. Chen, *Introduction to Plasma Physics and Controlled Fusion, 3rd ed.* Springer, 2016.

[13] A. Macchi, M. Borghesi, and M. Passoni, "Ion acceleration by superintense laser-plasma interaction," *Reviews of Modern Physics*, vol. 85, pp. 751–793, 2013.

[14] P. Gibbon, *Short Pulse Laser Interaction with Matter - An Introduction.* Imperial College Press, 2005.

[15] J. Davies, "Laser absorption by overdense plasmas in the relativistic regime," *Plasma Physics and Controlled Fusion*, vol. 51, pp. 1–21, 2009.

[16] H. Hertz, "Ueber einen einfluss des ultravioletten lichtes auf die elektrische entladung," *Annalen der Physik*, vol. 267, pp. 983–1000, 1887.

[17] A. Einstein, "Über einen die erzeugung und verwandlung des lichtes betreffenden heuristischen gesichtspunkt," *Annalen der Physik*, vol. 322, pp. 132–148, 1905.

[18] G. Voronov, G. Dleone, and N. Delona, "Multiphoton ionization of atoms. ii. ionization of krypton by ruby-laser radiation," *Soviet Physics JETP*, vol. 24, pp. 1122–1125, 1967.

[19] W. Kruer, *The Physics Of Laser Plasma Interactions.* CRC Press, 2003.

[20] S. Wilks and W. Kruer, "Absorption of ultrashort, ultra-intense laser light by solids and overdense plasmas," *IEEE Journal of Quantum Electronics*, vol. 33, pp. 1954–1968, 1997.

[21] F. Brunel, "Not-so-resonant resonant absorption," *Physical Review Letters*, vol. 59, pp. 52–55, 1987.

[22] S. C. Wilks, W. L. Kruer, M. Tabak, and A. B. Langdon, "Absorption of ultra-intense laser pulses," *Physical Review Letters*, vol. 69, pp. 1383–1386, 1992.

[23] M. I. K. Santala, M. Zepf, I. Watts, F. Beg, E. Clark, M. Tatarakis, K. Krushelnick, A. Dangor, T. McCanny, I. Spencer, R. Singhal, K. Ledingham, S. Wilks, A. Machacek, J. Wark, R. Allott, R. Clarke, and P. Norreys, "Effect of the plasma density scale length on the direction of fast electrons in relativistic laser-solid interactions," *Physical Review Letters*, vol. 84, p. 1459, 2000.

[24] F. Amiranoff, "Fast electron production in ultra-short high-intensity laser–plasma interaction and its consequences," *Measurement Science and Technology*, vol. 12, pp. 1795–1800, 2001.

[25] P. Catto and R. M. More, "Sheath inverse bremsstrahlung in laser produced plasmas," *The Physics of Fluids*, vol. 20, pp. 704–705, 1977.

[26] T.-Y. B. Yang, W. L. Kruer, R. M. More, and A. B. Langdon, "Absorption of laser light in overdense plasmas by sheath inverse bremsstrahlung," *Physics of Plasmas*, vol. 2, p. 3146, 1995.

[27] M. C. Kaluza, *Characterisation of Laser-Accelerated Proton Beams*. PhD thesis, Max-Planck-Institut für Quantenoptik Muenchen, 2004.

[28] K. Zeil, S. Kraft, S. Bock, M. Bussmann, T. E. Cowan, T. Kluge, J. Metzkes, T. Richter, R. Sauerbrey, and U. Schramm, "The scaling of proton energies in ultrashort pulse laser plasma acceleration," *New Journal of Physics*, vol. 12, pp. 1–16, 2010.

[29] M. Roth and M. Schollmeier, *Laser-Plasma Interactions and Applications*, ch. Ion Acceleration—Target Normal Sheath Acceleration, pp. 1–40. Springer International Publishing, 2013.

[30] S. Wilks, A. Langdon, T. Cowan, R. M., M. Singh, S. Hatchett, M. Key, D. Pennington, A. MacKinnon, and R. Snavely, "Energetic proton generation in ultra-intense laser-solid interactions," *Physics of Plasmas*, vol. 8, pp. 542–549, 2001.

[31] D. Jung, *Ion acceleration from relativistic laser nano-target interaction.* PhD thesis, Ludwig Maximilians Universitaet Muenchen, 2012.

[32] C. Chen, P. Patel, D. Hey, A. MacKinnon, M. Key, K. Akli, T. Bartal, F. Beg, S. Chawla, H. Chen, R. Freeman, D. Higginson, A. Link, T. Ma, A. MacPhee, R. Stephens, L. Van Woerkom, and B. Westover, "Bremsstrahlung and k alpha fluorescence measurements for inferring conversion efficiencies into fast ignition relevant hot electrons," *Physics of Plasmas*, vol. 16, pp. 082705–1, 2009.

[33] F. Beg, A. Bell, A. Dangor, C. Danson, E. Glinsky, B. Hammel, P. Lee, P. Norreys, and M. Tatarakis, "A study of picosecond laser–solid interactions up to $10^{19}\,\mathrm{W/cm^2}$," *Physics of Plasmas*, vol. 4, pp. 447–457, 1997.

[34] M. Haines, M. Wei, F. Beg, and R. Stephens, "Hot-electron temperature and laser-light absorption in fast ignition," *Physical Review Letters*, vol. 102, pp. 045008–1, 2009.

[35] S. J. Gitomer, R. Jones, F. Begay, A. Ehler, J. Kephart, and R. Kristal, "Fast ions and hot electrons in the laser-plasma interaction," *Physics of Fluids*, vol. 29, pp. 2679–2688, 1986.

[36] M. M. Allen, *Ion Acceleration from the Interaction of Ultra-Intense Lasers with Solid Foils.* PhD thesis, University of California, 2004.

[37] J. Fuchs, Y. Y. Sentoku, E. d'Humières, T. E. Cowan, J. Cobble, P. Audebert, A. Kemp, A. Nikroo, P. Antici, E. Brambrink, A. Blazevich, E. Campbell, J. Fernández, J.-C. Gauthier, M. Geissel, M. Hegelich, S. Karsch, H. Popescu, N. Renard-LeGalloudec, M. Roth, J. Schreiber, R. Stephens, and H. Pépin, "Comparative spectra and efficiencies of ions laser-accelerated forward from the front and rear surfaces of thin solid foils," *Physics of Plasmas*, vol. 14, pp. 053105–1, 2007.

[38] P. Mora, "Plasma Expansion into a Vacuum," *Physical Review Letters*, vol. 90, pp. 185002–1 – 185002–4, 2003.

[39] Y. B. Zel'dovich and Y. P. Raizer, *Physics of shock waves and high-temperature hydrodynamic phenomena.* Dover Publications, 2002.

[40] R. Z. Sagdeev, "Cooperative phenomena and shock waves in collisionless plasmas," *Reviews of Plasma Physics*, vol. 4, pp. 23–91, 1966.

[41] F. Fiuza, A. Stockem, E. Boella, R. A. Fonseca, L. O. Silva, D. Haberberger, S. Tochitsky, C. Gong, W. B. Mori, and C. Joshi, "Laser-driven shock acceleration of monoenergetic ion beams," *Physical Review Letters*, vol. 109, pp. 215001–1 – 215001–5, 2012.

[42] O. Klimo, J. Psikal, J. Limpouch, and V. T. Tikhonchuk, "Monoenergetic ion beams from ultrathin foils irradiated by ultrahigh-contrast circularly polarized laser pulses," *Physical Review Special Topics - Acellerators and Beams*, vol. 11, pp. 031301–1 – 031301–14, 2008.

[43] A. Macchi, S. Veghini, T. V. Liseykina, and F. Pegoraro, "Radiation pressure acceleration of ultrathin foils," *New Journal of Physics*, vol. 10, pp. 1–18, 2010.

[44] S. Kar, K. Kakolee, B. Qiao, A. Macchi, M. Cerchez, D. Doria, M. Geissler, P. McKenna, D. Neely, J. Osterholz, R. Prasad, K. Quinn, B. Ramakrishna, G. Sarri, O. Willi, X. Yuan, M. Zepf, and M. Borghesi1, "Ion acceleration in multispecies targets driven by intense laser radiation pressure," *Physical Review Letters*, vol. 109, pp. 185006–1 – 185006–5, 2012.

[45] A. Robinson, M. Zepf, S. Kar, R. Evans, and C. Bellei, "Radiation pressure acceleration of thin foils with circularly polarized laser pulses," *New Journal of Physics*, vol. 10, pp. 1–13, 2008.

[46] T. Esirkepov, M. Borghesi, S. Bulanov, G. Mourou, and T. Tajima, "Highly efficient relativistic-ion generation in the laser-piston regime," *Physical Review Letters*, vol. 92, pp. 175003–1 – 175003–4, 2004.

[47] A. Macchi, S. Veghini, and F. Pegoraro, ""light sail" acceleration reexamined," *Physical Review Letters*, vol. 103, p. 085003, 2009.

[48] D. Jung, L. Yin, D. Gauthier, H.-C. Wu, S. Letzring, B. Dromey, R. Shah, T. Palaniyappan, T. Shimada, R. Johnson, J. Schreiber, D. Habs, J. Fernández, B. Hegelich, and B. Albright, "Laser-driven 1gev carbon ions from preheated diamond targets in the break-out afterburner regime," *Physics of Plasmas*, vol. 20, pp. 083103–1 – 083103–9, 2013.

[49] A.-M. Schroer, *Investigation of ion acceleration from underdense targets using a high intensity short pulse laser*. PhD thesis, Heinrich-Heine University Düsseldorf, 2018.

[50] Amplitude, *Super booster 150$\mu$J - 10Hz High ps/ns contrast - User's Manual*.

[51] G. Cheriaux, P. Rousseau, F. Salin, J. Chambaret, B. Walker, and L. Dimauro, "Aberration-free stretcher design for ultrashort-pulse amplification," *Optics Letters*, vol. 21, pp. 414–416, 1996.

[52] M. Cerchez, R. Parasad, B. Aurand, A. Giesecke, S. Spickermann, E. Aktan, M. Swantusch, S. Brauckmann, M. Toncian, and T. Toncian, "Arcturus laser - a versatile high contrast, high power multi-beam laser system." High Power Laser Science and Engineering (submitted), 2019.

[53] DazzlerSystems, *Dazzler Systems Operating Manual*, 2005.

[54] Amplitude, *Accousto-Optic Programmable Gain Control Filter - Mazzler User's Manual*.

[55] Amplitude, *Pulsar 100 - 100TW/10Hz Femtosecond System - User's Manual*.

[56] B. Dromey, S. Kar, M. Zepf, and P. Foster, "The plasma mirror—a subpicosecond optical switch for ultrahigh power lasers," *Review of Scientific Instruments*, vol. 75, pp. 645–649, 2004.

[57] A. L. Giesecke, *Propagation Dynamics and High Harmonic Generation Using High Contrast Ultrashort Laser Pulses*. PhD thesis, Heinrich Heine Universität Düsseldorf, 2013.

[58] A. Siegman, *Lasers*. University Science Books, 1986.

[59] A. Niroomand-Rad, C. R. Blackwell, B. M. Coursey, K. P. Gall, J. M. Galvin, W. L. McLaughlin, A. S. Meigooni, R. Nath, J. E. Rodgers, and C. G. Soares, "Radiochromic film dosimetry - recommendations of aapm radiation therapy committee task group no. 55," tech. rep., AAPM, 1998.

[60] R. Fleischer *et al.*, *Nuclear tracks in solids, principles and applications*. University of California Press, 1975.

[61] H. G. Rinderknecht, J. Rojas-Herrera, A. B. Zylstra, J. A. Frenje, M. G. Johnson, N. S. H. Sio1, M. J. Rosenberg, C. K. Li, F. H. Séguin, R. D. Petrasso, T. Filkins, J. A. Steidle, J. A. Steidle, N. Traynor, and C. Freeman, "Impact of x-ray dose on track formation and data analysis for cr-39-based proton diagnostics," *Review of Scientific Instruments*, vol. 86, p. 123511, 2015.

[62] J. Charvat and F. Spurny, "Etching characteristics of cellulose nitrate and cr-39 after high dose electron irradiation," *Nuclear Tracks and Radiation Measurements*, vol. 14, pp. 451–455, 1988.

[63] A. Yogo, T.Maeda, T.Hori, H.Sakaki, K.Ogura, M.Nishiuchi, A.Sagisaka, P.R.Bolton, M. Murakami, S.Kawanishi, and K.Kondo, "Development of laser-driven quasi-monoenergetic proton beamline for radiobiology," *Nuclear Instruments and Methods in Physics Research A*, vol. 653, pp. 189–192, 2011.

[64] I. J. Paterson, R. J. Clarke, N. C. Woolsey, and G. Gregori, "Image plate response for conditions relevant to laser–plasma interaction experiments," *Measurement Science and Technology*, vol. 19, pp. 1–5, 2008.

[65] M. Katto, R. Matsumoto, K. Kurosawa, W. Sasaki, Y. Takigawa, and M. Okuda, "Laser beam profiler in the vacuum ultraviolet spectral range using photostimulable phosphor," *Review of Scientific Instruments*, vol. 64, pp. 319–324, 1993.

[66] K. Takahashi, K. Koda, J. Miyahara, Y. Kanemitsu, K. Amitani, and S. Shionoya, "Mechanism of photostimulated luminescence in bafx:eu2+ (x=cl,br) phosphors," *Journal of Luminescence*, vol. 31-32, pp. 266–268, 2002.

[67] A. Mančić, J. Fuchs, P. Antici, S. A. Gaillard, and P. Audebert, "Absolute calibration of photostimulable image plate detectors used as ( 0.5 – 20 mev ) high-energy proton detectors," *Review of Scientific Instruments*, vol. 79, p. 073301, 2008.

[68] J. L. Wiza, "Microchannel plate detectors," *Nuclear Instruments and Methods*, vol. 162, pp. 587–601, 1979.

[69] R. Cambria, J. Herault, N. Brassart, M. Silari, and P. P Chauvelz, "Proton beam dosimetry: A comparison between the faraday cup and an ionization chamber," *Physics in Medicine and Biology*, vol. 42, pp. 1185–1196, 1997.

[70] J. T. Lyman, M. Awschalom, P. Berardo, H. Bicchsel, G. T. Y. Chen, J. Dicello, P. Fessenden, M. Goitein, G. Lam, J. C. McDonald, A. F. Smith, R. T. Haken, L. Verhey, and S. Zink, "Protocol for heavy charged-particle therapy beam dosimetry," tech. rep., AAPM, 1986.

[71] S. Vynckier, D. Bonnett, and D. Jones, "Code of practice for clinical proton dosimetry," *Radiotherapy and Oncology*, vol. 20, pp. 53–63, 1991.

[72] S. Nakamura, Y. Iwashita, A. Noda, T. Shirai, H. Tongu, A. Fukumi, M. Kado, A. Yogo, M. Mori, S. Orimo, K. Ogura, A. Sagisaka, M. Nishiuchi, Y. Hayashi, Z. Li, H. Daido, and Y. Wada, "Real-time optimization of proton production by intense short-pulse laser with time-of-flight measurement," *Japanese Journal of Applied Physics*, vol. 34, pp. L913–L916, 2006.

[73] H. Mörtel, J. Georgi, W. Eyrich, M. Fritsch, and L. Distel, "Automation of the particle dosimetry and the dose application for radiobiological experiments at a vertical proton beam," *Nuclear Instruments and Methods in Physics Research A*, vol. 489, pp. 503–508, 2002.

[74] W. H. Bragg and R. Kleeman, "Xxxix. on the alpha particles of radium, and their loss of range in passing through various atoms and molecules," *The London, Edinburgh, and Dublin Philosophical Magazine and Journal of Science*, vol. 10:57, pp. 318–340, 1905.

[75] J. F. Ziegler, M. Ziegler, and J. Biersack, "Srim – the stopping and range of ions in matter (2010)," *Nuclear Instruments and Methods in Physics Research B*, vol. 268, pp. 1818–1823, 2010.

[76] G. Both, R. Krotz, K. Lohmer, and W. Neuwirth, "Density dependence of stopping cross sections measured in liquid ethane," *Physical Review A*, vol. 28, p. 3212, 1983.

[77] R. Katz, "Track structure theory in radiobiology and in radiation detection," *Nuclear Track Detection*, vol. 2, pp. 1–28, 1978.

[78] E. J. Hall and A. J. Giaccia, *Radiobiology for the radiologist*. Wolters Kluwer, 2012.

[79] D. T. Goodhead, "Initial events in the cellular effects of ionizing radiations : clustered damage in dna," *International Journal of Radiation Biology*, vol. 65, pp. 7–17, 1994.

[80] E. Hairer, C. Lubich, and M. Roche, *The numerical solution of differential-algebraic systems by Runge-Kutta methods*. Springer-Verlag, 1989.

[81] L. Ingenbleek, "Dosimetrie von laserbeschleunigten protonen (bachelorarbeit)," Master's thesis, Heinrich-Heine-Universität Düsseldorf, 2017.

[82] J. F. Ziegler and J. M. Manoyan, "The stopping of ions in compounds," *Nuclear Instruments and Methods in Physics Research B*, vol. 35, pp. 215–228, 1988.

[83] A. Mick, "Absolute energiemessung laser beschleunigter protonen," Master's thesis, Heinrich-Heine University Düsseldorf, 2012.

[84] G. J. Williams, B. R. Maddox, H. Chen, S. Koijima, and M. Millecchia, "Calibration and equivalency analysis of image plate scanners," *Review of Scientific Instruments*, vol. 85, p. 11E604, 2014.

[85] Y. Amemiya, T. Matsushita, A. Nakagawa, Y. Satow, J. Miyahara, and J. ichi Chikawa, "Design and performance of an imaging plate system for x-ray diffraction study," *Nuclear Instruments and Methods in Physics Research A*, vol. 266, pp. 645–653, 1988.

[86] F. Ingenito, P. Andreoli, D. Batani, G. Boutoux, M. Cipriani, F. Consoli, G. Cristofari, A. Curcio, R. De Angelis, G. Di Giorgio, J. Ducret, P. Forsetier-Colleoni, S. Hulin, K. Jakubowska, and N. Rabhi, "Comparative calibration of ip scanning equipment," in *Plasma Physics by Laser and Applications (PPLA 2015) ENEA Research Centre, Frascati, Italy 5-7 October, 2015*, 2015.

[87] A. Chatterjee and W. Holley, "A general theory of dna strand break production by direct and indirect effects," *Radiation protection Dosimetry*, vol. 31, pp. 241–247, 1990.

[88] R. B. Mikkelsen and P. Wardman, "Biological chemistry of reactive oxygen and nitrogen and radiation-induced signal transduction mechanisms," *Oncogene*, vol. 22, pp. 5734–5754, 2003.

[89] S. Reichert, V. Reinbold, S. Hehlgans, T. Efferth, C. Rödel, and F. Rödel, "A radiosensitizing effect of artesunate in glioblastoma cells is associated with a diminished expression of the inhibitor of apoptosis protein survivin," *Radiotherapy and Oncology*, vol. 103, pp. 394–401, 2012.

[90] S. Toyokuni, K. Okamoto, J. Yodoi, and H. Hiai, "Persistent oxidative stress in cancer," *FEBS Letters*, vol. 358, pp. 1–3, 1995.

[91] Y. Yokota, T. Funayama, Y. Mutou-Yoshihara, and H. Ikeda, "The bystander cell-killing effect mediated by nitric oxide in normal human fibroblasts varies with irradiation dose but not with radiation quality," *International Journal of Radiation Biology*, vol. 91, pp. 383–388, 2015.

[92] A. Yogo, K. S. M. Nishikino, T. Maeda, H. Sakaki, T. Hori, K. Ogura, M. Nishiuchi, T. Teshima, H. Nishimura, K. Kondo, P. R. Bolton, and S. Kawanishi,

"Measurement of dna double-strand break yield in human cancer cells by high-current, short-duration bunches of laser-accelerated protons," *Japanese Journal of Applied Physics*, vol. 50, pp. 106401–1 – 106401–7, 2011.

[93] K. Markey, P. McKenna, C. Brenner, C. D.C., M. Günther, K. Harres, S. Kar, K. Lancaster, F. Nürnberg, M. Quinn, A. Robinson, R. M., M. Zepf, and D. Neely, "Spectral enhancement in the double pulse regime of laser proton acceleration," *Physical Review Letters*, vol. 105, p. 195008, 2010.

[94] J. Green, N. Booth, R. Dance, R.J.Gray, D.A.MacLellan, A. Marshall, P. McKenna, C. Murphy, C. Ridgers, A. Robinson, D. Rusby, R. Scott, and L. Wilson, "Time-resolved measurements of fast electron recirculation for relativistically intense femtosecond scale laser-plasma interactions," *Scientific Reports*, vol. 8, p. 4525, 2018.

[95] O. Jäckel, *Characterization of ion acceleration with relativistic laser-plasma*. PhD thesis, Universität Jena, 2009.

[96] M. Hegelich, S. Karsch, G. Pretzler, D. Habs, K. Witte, W. Guenther, M. Allen, A. Blazevich, J. Fuchs, J. Gauthier, M. Geissel, P. Audebert, T. Cowan, and M. Roth, "Mev ion jets from short-pulse-laser interaction with thin foils," *Physical Review Letters*, vol. 89, pp. 085002–1, 2002.

[97] F. Lindau, O. Lundh, A. Persson, P. McKenna, K. Osvay, D. Batani, and C.-G. Wahlström, "Laser-accelerated protons with energy-dependent beam direction," *Physical Review Letters*, vol. 95, p. 175002, 2005.

[98] K. Eidmann, J. M. ter Vehn, and T. Schlegel, "Hydrodynamic simulation of subpicosecond laser-interaction with solid-density matter," *Physcial Review E*, vol. 62, pp. 1202–1214, 2000.

[99] A. Henig, S. Steinke, M. Schnürer, T. Sokollik, R. Hörlein, D. Kiefer, D. Jung, J. Schreiber, B. Hegelich, X. Yuan, J. M. ter Vehn, P. Nickles, W. Sandner, and D. Habs, "Radiation-pressure acceleration of ion beams driven by circularly polarized laser pulses," *Physical Review Letters*, vol. 103, p. 245003, 2009.

[100] D. Haberberger, S. Tochitsky, F. Fiuza, C. Gong, R. A. Fonseca, L. O. Silve, W. B. Mori, and C. Joshi, "Collisionless shocks in laser-produced plasma generate monoenergetic high-energy proton beams," *nature physics*, vol. 8, pp. 95–99, 2012.

[101] V. T. Tikhonchuk, A. A. Andreev, S. G. Bochkarev, and V. Y. Bychenkov, "Ion acceleration in short-laser-pulse interaction with solid foils," *Plasma Physics and Controlled Fusion*, vol. 47, pp. B869–B877, 2005.

[102] B. Boughton and V. R. Wheatley, "The fatty acid composition of the skin surface fat ('sebum') of normal human subjects," *Journal of Investigative Dermatology*, vol. 33, pp. 49–55, 1959.

[103] R. Sims, "Determining the density of triglycerides and esters by the falling drop method," *Journal of the American Oil Chemists' Society*, vol. 31, pp. 144–147, 1954.

[104] S. Brauckmann, *X-ray generation by high intensity laser pulses.* PhD thesis, Universität Düsseldorf, 2017.

[105] P. Antici, J. Fuchs, M. Borghesi, L. Gremillet, T. Grismayer, Y. Sentoku, E. d'Humières, C. Cecchetti, A.Mančić, A. Pipahl, T. Toncian, O. Willi, P. Mora, and P. Audebert, "Hot and cold electron dynamics following high-intensity laser matter interaction," *Physical Review Letters*, vol. 101, p. 105004, 2008.

[106] S. Eliezer, *The Interaction of High-Power Lasers with Plasmas.* CRC Press, 2002.

[107] E. Aktan, "Laser plasma interactions using ultra-thin foils," Master's thesis, Heinrich-Heine University Düsseldorf, 2016.

# List of Figures

# Acknowledgements

I would like to thank Professor Willi for being my advisor during my PhD.

I would also like to thank Professor Pukhov for accepting the role as second assessor.

Special thanks go to Rajendra Prasad, Marco Swantusch and Mirela Cerchez for many fruitful discussions and invaluable support in the lab.

Thanks to Mustafa Gaja and Mara Wiltshire for help with the initial data analysis.

Thanks to Thomas Gangolf for discussions and insightful comments on interpretation of data.

Thanks should also go to the central workshop and the ILPP's staff.

Special thanks go to Ilhan Engin, Sascha Raschke and Thomas Hahn for their repeated support and important conversations. You are decent human beings.

In addition to that, Sascha Raschke also deserves a lot of credit for his decisive role in the cell experiments and his analysis of their biological endpoints.

Thanks also to Professor Iliakis and Professor Boege for facilitating the cell experiments.

Thanks to Ulrich Giesen and the staff at the Van de Graaff accelerator at Physikalisch Technische Bundesanstalt (PTB) in Braunschweig. Impressive work. Everybody should visit the PTB if they have the time.

Thanks to Anna Levy, Domenico Doria and Gianluca Sarri for allowing me to witness excellency at work and thanks to École Polytechnique, the Rutherford Appleton Laboratory and Professor Willi for making it possible.

Many thanks to Jens Ehlert, Jürgen Böker, Lukas Ingenbleek, Esin Aktan, Bastian Aurand, Stephanie Brauckmann, Marie Schroer, Tobias Thiele, Toma and Monika Toncian, Thomas Wowra, Farzan Hamzehei, Marius Blecher, Xiaoming Zhu and Alexander Mick for help and company in the lab. Additional thanks go to Jürgen Böker for grant-

ing permission to analyze ion data from his experiments and to Anna-Lena Giesecke for plasma mirror related discussions.

Thanks to my parents for their love and lasting support.

Special thanks to my dear friend Julia for distracting me with fun and absurd raccoon stories when I really was in need of some distraction.

I hope I didn't forget anyone. If I did, please be assured that it's not out of malice. My sincere gratitude goes to everybody who helped bring light into darkness and gave me the opportunity to learn valuable lessons during the journey.

# Erklärung zu inhaltlichem Anteil des Autors an Manuskript

Mein Anteil am Manuskript "Ultra-Short laser-accelerated proton pulses have similar DNA-damaging effectiveness but produce less immediate nitroxidative stress than conventional proton beams" [7] ist wie folgt:

- Teilnahme an Experimenten am Institut für Laser- und Plasmaphysik (ILPP) und der Physikalisch Technischen Bundesanstalt (PTB)
- Entwurf der Target- und Diagnostikgeometrie für Experimente am ILPP
- Bau des Targets für Experimente am ILPP [9]
- Dosimetrie für Experimenten mit laserbeschleunigten Protonen am ILPP (Datenauswertung)
- Mitarbeit an dosimetrischer Auswertung für Experimente am Van de Graaff Generator an der PTB (SRIM-Simulationen für Datenauswertung)
- Berechnung durchschnittlicher LET für LAP
- Mitarbeit an Berechnung von radiobiological effectiveness für LAP
- Mitarbeit an Formulierung des Manuskripts

Direkte Bezüge auf dieses Manuskript finden sich in den Kapiteln 1, 4 und 5. Abbildungen 5.15 und 5.16 wurden aus dem Paper übernommen. Abbildung 5.14 wurde für diese Arbeit in dort angegebener Weise modifiziert.

Das Paper wurde am 31. August 2016 im Magazin "Scientific Reports" des Nature-Verlages veröffentlicht. Die vollständige Autorenliste lautet: S. Raschke, S. Spickermann, T. Toncian, M. Swantusch, J. Boeker, U. Giesen, G. Iliakis, O. Willi und F. Boege.

# Eidesstattliche Versicherung

Ich versichere an Eides Statt, dass die Dissertation von mir selbständig und ohne unzulässige fremde Hilfe unter Beachtung der "Grundsätze zur Sicherung guter wissenschaftlicher Praxis an der Heinrich-Heine-Universität Düsseldorf" erstellt worden ist.

Die vorliegende Dissertation wurde in der vorgelegten oder in ähnlicher Form noch bei keiner anderen Institution eingereicht. Ich habe bisher keine erfolglosen oder erfolgreichen Promotionsversuche unternommen.

Düsseldorf, Juni 2019 Sven Spickermann